

AD-A245 014

Quarterly Technical Report

Solid State Research

JAN 21 1992

92-01613



199112

Lincoln Laboratory

MASSACHUSETTS INSTITUTE OF TECHNOLOGY

LINCOLN, MASSACHUSETTS



Contracted to the Department of the Air Force under Contract F19628-90-C-0001

Approved for public release; distribution is unlimited.

92 1 17 029

This report is based on studies performed at Lincoln Laboratory, a center for research in the Massachusetts Institute of Technology. The work was sponsored by the Department of the Air Force under Contract #F19628-65-C-5602.

This document is prepared to satisfy needs of U.S. Government agencies.

The ESD Public Affairs Office has reviewed this report, and its release to the National Technical Information Service, where it will be available to the general public, including foreign nationals.

The technical report has been reviewed and is approved for publication.

FOR THE COMMANDER

Hugh L. Southall

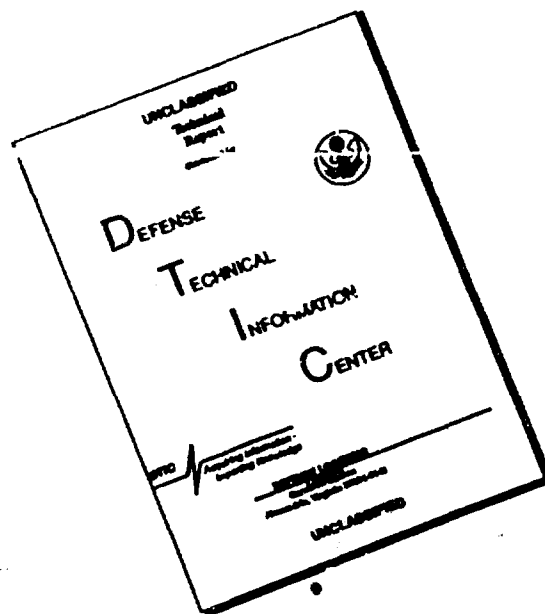
Hugh L. Southall, Lt. Col., USAF
Chief, ESD Lincoln Laboratory Project Office

Non-Lincoln Replants

PLEASE DO NOT RETURN

Permission is given to destroy this document
when it is no longer needed.

DISCLAIMER NOTICE



THIS DOCUMENT IS BEST
QUALITY AVAILABLE. THE COPY
FURNISHED TO DTIC CONTAINED
A SIGNIFICANT NUMBER OF
PAGES WHICH DO NOT
REPRODUCE LEGIBLY.

**MASSACHUSETTS INSTITUTE OF TECHNOLOGY
LINCOLN LABORATORY**

SOLID STATE RESEARCH

QUARTERLY TECHNICAL REPORT

1 FEBRUARY — 30 APRIL 1991

ISSUED 10 OCTOBER 1991

Approved for public release; distribution is unlimited.

LEXINGTON

MASSACHUSETTS

ABSTRACT

This report covers in detail the research work of the Solid State Division at Lincoln Laboratory for the period 1 February through 30 April 1991. The topics covered are Electrooptical Devices, Quantum Electronics, Materials Research, Submicrometer Technology, High Speed Electronics, Microelectronics, and Analog Device Technology. Funding is provided primarily by the Air Force, with additional support provided by the Army, DARPA, Navy, SDIO, NASA, and DOE.



Accession For	
NTIS GRA&I	<input checked="" type="checkbox"/>
DTIC TAB	<input type="checkbox"/>
Unannounced	<input type="checkbox"/>
Justification	
By	
Distribution/	
Availability Codes	
Dist	Avail and/or Special
A-1	

TABLE OF CONTENTS

Abstract	iii
List of Illustrations	vii
List of Tables	xi
Introduction	xiii
Reports on Solid State Research	xvii
Organization	xxvii
 1. ELECTROOPTICAL DEVICES	 1
1.1 Integrated-Optical Modulators for an Adaptive Nulling System	1
1.2 Self-Aligned Fabrication Technique for Two-Dimensional Surface-Emitting Diode Laser Arrays	2
1.3 Fabrication of High-Efficiency Two-Dimensional Surface-Emitting InGaAs/AlGaAs and AlInGaAs/AlGaAs Diode Laser Arrays	7
1.4 Proton Bombardment of $n\text{-Ga}_{0.51}\text{In}_{0.49}\text{P}$	11
1.5 $\text{Ga}_{0.51}\text{In}_{0.49}\text{P}$ as a Reference Crystal for (002) Rocking Curves of AlGaAs Layered Structures	13
 2. QUANTUM ELECTRONICS	 19
2.1 Thermal Loading in Nd:YAG and Yb:YAG	19
 3. MATERIALS RESEARCH	 23
3.1 High-Power AlInGaAs/AlGaAs Strained Single-Quantum-Well Diode Lasers	23
3.2 Room-Temperature CW Operation of GaInAsSb/AlGaAsSb Diode Lasers Emitting at $2.2\ \mu\text{m}$	26
 4. SUBMICROMETER TECHNOLOGY	 31
4.1 Excimer-Laser-Induced Sub- $0.5\text{-}\mu\text{m}$ Patterning of WO_3 Thin Films	31
4.2 Fast Room-Temperature Growth of SiO_2 Films by Molecular-Layer Dosing	35
 5. HIGH SPEED ELECTRONICS	 41
5.1 Vacuum Field-Emitter Triode	41
5.2 Electrical and Structural Characterization of GaAs Vertical-Sidewall Layers Grown by Atomic Layer Epitaxy	43

6.	MICROELECTRONICS	47
6.1	Suppression of Charged-Particle Events in Deep-Depletion CCD Imagers	47
6.2	Modeling of Proton-Induced Vacancy Generation in Si	49
7.	ANALOG DEVICE TECHNOLOGY	53
7.1	Quad CMOS Buffer to Enhance CCD Clocks	53
7.2	Modes on Two- and Three-Conductor Coplanar Transmission Lines	55
7.3	Solid State Electrocaloric Refrigeration	58

LIST OF ILLUSTRATIONS

Figure No.		Page
1-1	Block diagram of optical nulling system. Two channels are shown, with the solid lines and dashed lines indicating optical and electrical paths, respectively.	1
1-2	Measured (a) amplitude and (b) phase response of two lithium niobate traveling-wave modulators.	3
1-3	Schematic diagram of the geometry of the monolithic laser array.	4
1-4	Self-aligned process for fabricating the laser facets and parabolic deflecting mirrors.	5
1-5	Power output vs current for an etched-facet edge-emitting laser.	6
1-6	Near-field pattern of two rows of 24 surface-emitting lasers.	6
1-7	Power output vs current for a monolithic surface-emitting laser array.	7
1-8	Schematic diagram of a monolithic two-dimensional surface-emitting array of strained-layer diode lasers. Each individual laser utilizes a folded cavity consisting of two 45° internal reflectors and two top-surface facets.	8
1-9	Scanning electron micrograph showing a 45° cavity-folding mirror from one of the AlInGaAs/AlGaAs arrays.	9
1-10	Near-field pattern of a 48-element AlInGaAs/AlGaAs array with differential quantum efficiency of 51%.	9
1-11	Pulsed output power vs current for a one-row, 16-element InGaAs/AlGaAs array. The current pulses were 100 ns wide at a 1-kHz repetition rate, and the differential quantum efficiency was ~ 56%.	10
1-12	Electron carrier concentration vs depth obtained from C-V data of 100-keV, proton-bombarded n -GaInP for incremental doses of $1 \times 10^{11} \text{ cm}^{-2}$.	12
1-13	Electron carrier concentration vs depth obtained from C-V data of 100-keV proton-bombarded n^+ -GaInP for incremental doses of $2 \times 10^{12} \text{ cm}^{-2}$.	12
1-14	(a) Simulated (004) rocking curve of a MQW structure with 10-nm GaAs wells and 50-nm $\text{Al}_{0.5}\text{Ga}_{0.5}\text{As}$ barriers repeated five times. (b) Simulated (002) rocking curve of the same MQW structure. A comparison of (a) and (b) illustrates the value of the (002) reflection for enhancing the satellite structure. For both curves the origin of the angle scale is taken at the Bragg angle of GaAs, ϕ_B (004) = 33° and ϕ_B (002) = 16°.	14

Figure No.		Page
1-15	(a) Experimental (002) rocking curve of a 20-period AlGaAs interference-stack sample. (b) Simulated rocking curve with best-fit parameters, in which the peaks due to the substrate and the various satellite orders are labeled. Some sample curvature has been introduced to broaden the simulated peaks.	16
2-1	Fractional thermal loading for five samples of Nd:YAG pumped at 808 nm with low pump intensity. The curve shows the expected thermal loading due to the quantum defect and concentration quenching.	20
2-2	Fractional thermal loading of Nd:YAG during CW laser operation. The higher fractional thermal loading at threshold compared with that in Figure 2-1 is due to effects that occur with high pump intensity. The solid line is a model fitted to the data that projects $\eta_r = 0.36$ for laser operation very far above threshold. The vertical bars represent errors that occur from measurement to measurement and do not include systematic errors such as imperfect power meter calibration and uncertainty in the heat capacity.	21
3-1	Pulsed threshold current vs temperature for a $500 \times 1000\text{-}\mu\text{m}$ AlInGaAs/AlGaAs diode laser.	24
3-2	Pulsed differential quantum efficiency vs temperature for the diode laser of Figure 3-1.	24
3-3	CW output power and power efficiency vs current for a $500 \times 1000\text{-}\mu\text{m}$ AlInGaAs/AlGaAs diode laser at a heatsink temperature of 10°C .	25
3-4	CW output power vs current for a $500 \times 1000\text{-}\mu\text{m}$ AlInGaAs/AlGaAs diode laser at heatsink temperatures between 25 and 125°C .	25
3-5	Lifetest of a $500 \times 1000\text{-}\mu\text{m}$ AlInGaAs/AlGaAs diode laser at a heatsink temperature of 10°C , for output power levels of 1 W/facet for 1100 h and then 2 W/facet for 800 h .	26
3-6	Dependence of threshold current density on cavity length for broad-stripe GaInAsSb/AlGaAsSb lasers with a $\text{Ga}_{0.84}\text{In}_{0.16}\text{As}_{0.14}\text{Sb}_{0.86}$ active layer and two different cladding layer compositions.	28
3-7	CW output power vs current for a GaInAsSb/AlGaAsSb laser $30\text{ }\mu\text{m}$ wide by $300\text{ }\mu\text{m}$ long at several heatsink temperatures.	28
3-8	Dependence of threshold current on temperature for pulsed and CW operation of the diode laser of Figure 3-7.	29
4-1	Semilog plot of the etch rate of a WO_3 film in a CF_4 parallel-plate plasma as a function of the RF power density. The film had been deposited on a Si(100) substrate to a thickness of 180 nm . The CF_4 etch pressure was 300 mTorr . At low power levels, one 25-mJ/cm^2 laser pulse causes a fivefold reduction in etch rate.	32

Figure No.		Page
4-2	XPS spectra taken at 45° takeoff angle of the F 1s photoelectron of an as-deposited WO ₃ film on Si(100) and of samples of the same film following three postdeposition treatments. The as-deposited film has only one peak, at 684.2 eV, and the films that have been partially etched in a CF ₄ plasma have additional peaks whose intensity is modified by laser exposure prior to etching.	32
4-3	Scanning electron micrographs of nominally (a) 0.5-μm and (b) 0.35-μm lines and spaces patterned in an all-dry bilayer. First, a 1-μm-thick <i>a</i> -C:H layer was deposited by PECVD, and then a 75-nm-thick WO ₃ imaging layer was deposited, also by PECVD. Next, exposure was performed in projection with a 193-nm excimer laser in one 20-mJ/cm ² pulse, followed by dry development in a low-power CF ₄ plasma and pattern transfer through the <i>a</i> -C:H layer in an O ₂ reactive ion etching plasma.	34
4-4	Scanning electron micrographs of silicon trenches filled by deposited oxides (cleaved profile). Note the excellent filling and planarization of the substrate topography. Typical growth conditions are 2-Torr H ₂ O, 5-Torr SiCl ₄ , and ~ 15-min total growth time.	36
4-5	Low H ₂ O pressure measurements of SiO ₂ deposition rates. The H ₂ O adsorption isotherm (13°C) on the growth surface, measured in the same apparatus, is shown as a dashed line.	38
4-6	Dependence of SiO ₂ deposition on substrate temperature at fixed 0.28-Torr H ₂ O and 5-Torr SiCl ₄ pressures. The solid curve is drawn as an aid to the eye.	38
5-1	Schematic view of a VACFET. The high field between the grid and each knife-edge causes electrons to emit from the knife-edges into the vacuum spaces. The electrons then move ballistically to the positively biased metal anode. A small variation in voltage on the grid causes a large variation in anode current.	41
5-2	VACFET shown in (a) a cross-sectional drawing and (b) an SEM. Grooves 100 nm wide are cut through an insulator-metal-insulator sandwich, and then hafnium is evaporated to form the knife-edges as well as to close off the vacuum spaces.	42
5-3	SEM of a completed VACFET. The internal vacuum cavities of the device are sealed during the fabrication process, enabling these devices to be subsequently tested and used in circuits in the same manner as typical semiconductor devices.	43
5-4	Schematic diagram of a test structure consisting of a GaAs rod with vertical-sidewall epilayers and wrap-around ohmic contacts.	44
5-5	SEM showing a vertical-sidewall test structure.	44

Figure No.		Page
5-6	SEM of a cleaved and stained cross section from an overgrown rod. GaAlAs was used as an interface marker layer.	45
5-7	Cross-sectional TEM showing the interface between a GaAs ALE layer and an annealed ohmic contact. The interface roughness is about 80 nm.	45
6-1	Cross section of a CCD imager with a reverse-biased n^+ back junction. Spurious charge generated in the lower depletion region by energetic charged particles is swept to the back junction in order to prevent collection of this charge by the CCD wells.	48
6-2	Depletion regions formed on the front surface of the device by the CCD and the back surface by the n^+ back junction. The back-surface depletion region was measured as a function of bias using capacitance-voltage measurements.	48
6-3	Histograms showing the frequency of charge events resulting from Co^{60} irradiation for various values of back-junction bias.	50
6-4	Total number of instances where a pixel contained more than $15 e^-$ as a function of back-junction bias under Co^{60} irradiation.	50
6-5	Differential vacancy production in Si by energetic protons.	51
7-1	Schematic of a single unit of the quad CMOS buffer. Ratios depicted for MOSFETs M1 through M4 are the ratios of gate length to gate width for each device.	54
7-2	Optimized layout for a single unit of the quad CMOS buffer shown (a) graphically and (b) in a photomicrograph of an actual circuit.	54
7-3	Cross sections of complementary coplanar lines showing (a) three conductors and (b) three slots.	55
7-4	Electrocaloric equivalent circuit. The ideal transformer turns ratio N is determined by electric and thermal units.	60

LIST OF TABLES

Table No.		Page
1-1	Reflectivities for Epitaxial Materials	15
7-1	Dual Compact Modes	57
7-2	Intermodal Cross Talk Between Distant Coplines (or Between Their Duals)	58

INTRODUCTION

1. ELECTROOPTICAL DEVICES

A pair of lithium niobate traveling-wave electrooptic intensity modulators has been built and tested for use in an optical adaptive nulling system. The device frequency responses track each other to within 0.03 dB and 0.22° in amplitude and phase, respectively, over the 5- to 7-GHz frequency band, as is required to provide attractive nulling system performance.

Monolithic two-dimensional AlGaAs surface-emitting laser arrays with etched facets and external parabolic deflecting mirrors have been fabricated using a new self-aligned fabrication process. Initial performance results for the arrays are very encouraging.

Monolithic two-dimensional surface-emitting arrays of folded-cavity strained-layer InGaAs/AlGaAs and AlInGaAs/AlGaAs diode lasers have been fabricated and operated pulsed with low threshold current densities and over 50% differential quantum efficiencies. Optical projection printing and chlorine ion-beam-assisted etching (IBAE) were used in key fabrication steps.

Proton bombardment of n^- and n^+ -Ga_{0.51}In_{0.49}P/GaAs heterostructures has produced regions of high resistivity that are comparable to those normally obtained in GaAs. In the n^+ material ($n^+ = 1 \times 10^{18} \text{ cm}^{-3}$), capacitance-voltage measurements indicate that a 0.5- μm -thick layer of highly compensated GaInP is formed after a proton bombardment of $2 \times 10^{13} \text{ cm}^{-2}$ at 100 keV through a 1300-Å-thick Ti/Au Schottky-barrier contact.

A 3- μm -thick epitaxial layer of Ga_{0.51}In_{0.49}P has been shown to fulfill the need for a reference crystal for (002) reflections with GaAs-based structures. This greatly enhances the usefulness of the double-crystal diffractometer for structural determinations of AlGaAs superlattices, multiple quantum wells, and interference stacks.

2. QUANTUM ELECTRONICS

The thermal loading of Nd:YAG and Yb:YAG has been measured for diode laser excitation of the dopant ion. In Nd:YAG the fraction of the absorbed optical power converted to heat is in the range of 0.34 to 0.43 and generally increases with doping; in one sample of Yb:YAG this fraction is 0.11.

3. MATERIALS RESEARCH

Strained-layer AlInGaAs/AlGaAs graded-index separate-confinement heterostructure single-quantum-well diode lasers with cavity width and length of 500 and 1000 μm , respectively, have been operated CW at a heatsink temperature of 10°C with output power up to 4.9 W/facet and power efficiency as high as 49%. Promising results have been obtained in initial reliability tests on uncoated devices at heatsink temperatures of 10 and 50°C.

Gain-guided $\text{Ga}_{0.84}\text{In}_{0.16}\text{As}_{0.14}\text{Sb}_{0.86}/\text{Al}_{0.75}\text{Ga}_{0.25}\text{As}_{0.06}\text{Sb}_{0.94}$ double-heterostructure diode lasers emitting at $\sim 2.2 \mu\text{m}$ have been operated CW at heatsink temperatures up to 30°C . The maximum output powers obtained at 5 and 20°C were 10.5 and 4.6 mW/facet, respectively.

4. SUBMICROMETER TECHNOLOGY

Thin films of WO_3 have been used as dry-deposited, dry-developed inorganic resists for 193-nm projection lithography. Negative-tone patterning with sub- $0.5\text{-}\mu\text{m}$ resolution was obtained with laser pulses that modify the atomic arrangement in this amorphous material.

A new method for controlled, room-temperature deposition of SiO_2 thin films has been demonstrated. Under optimized conditions, the surface chemical reactions between adsorbed water and gaseous SiCl_4 result in the growth of stoichiometric, conformal, and hermetic films.

5. HIGH SPEED ELECTRONICS

A vacuum field-emitter triode has been fabricated consisting of an array of microtriode cells, each sealed under vacuum and containing a single knife-edge field-emission cathode. The grating periodicity in the device is $0.2 \mu\text{m}$, making it by far the smallest-geometry vacuum triode ever reported.

Electrical and structural measurements have been performed on novel test structures fabricated from GaAs layers grown by atomic layer epitaxy on the vertical sidewalls of rods formed by IBAE. The results indicate that the properties of the layers are suitable for fabricating electronic, electrooptic, and photonic devices.

6. MICROELECTRONICS

A method of suppressing charged-particle events resulting from high-energy radiation has been demonstrated on a charge-coupled device (CCD) imager made on high-resistivity material. A reverse-biased junction on the back of the device is used to create a depletion region extending through a major fraction of the device thickness and to remove charge generated in this region.

An analytical model of the generation of vacancy defects in Si due to both incident protons and the resulting Si cascades has been derived. This computer simulation runs much more rapidly than the public domain program TRIM, agrees well with TRIM over 6 orders of magnitude of proton energies, and predicts that protons with energies of $\sim 100 \text{ keV}$ are the most damaging to the Si in the region of the buried channel of a CCD.

7. ANALOG DEVICE TECHNOLOGY

A quad CMOS buffer has been produced using a $2\text{-}\mu\text{m}$ CMOS/CCD process developed for the realization of high-performance analog signal processing devices. Test results show that this buffer can drive a 25-pF capacitive load in 1.2 ns, which is a significant improvement in current drive capability over commercially available parts.

The laterally confined modes that propagate on coplanar parallel strip transmission lines and their duals, obtained by interchanging conductor and gaps along the plane, have natural characteristic impedance levels, which can be modified only slightly by reasonable choices for transverse dimensions. Calculations based on the quasi-TEM model and very thin conductors indicate that, for a given average separation, the greatest isolation between adjoining structures occurs for properly designed systems of three conductors with the center conductor driven in one polarity and the outer conductors driven in the opposite polarity.

The coupling of thermal and electrical properties of materials by magnetostriction or electrostriction to provide electrocaloric refrigeration has been investigated. The study found that the modest thermal expansion of solids limits electrocaloric heat pumps to no-load differentials of only a degree or two per stage and to discouragingly low coefficients of performance.

REPORTS ON SOLID STATE RESEARCH

1 FEBRUARY THROUGH 30 APRIL 1991

PUBLICATIONS

High-Dynamic-Range, Low-Noise Analog Optical Links Using External Modulators: Analysis and Demonstration	G. E. Betts L. M. Johnson C. H. Cox III	<i>Proc. SPIE</i> 1371 , 252 (1990)
Nb/AlO _x /Nb Trilayer Process for the Fabrication of Submicron Josephson Junctions and Low-Noise dc SQUIDS	M. Bhushan E. M. Macedo	<i>Appl. Phys. Lett.</i> 58 , 1323 (1991)
Laser-Chemical Three-Dimensional Writing of Multimaterial Structures for Microelectromechanics	T. M. Bloomstein D. J. Ehrlich	<i>Proceedings IEEE Micro Electro Mechanical Systems</i> (IEEE, New York, 1991), p. 202
Efficient Coupling of Multiple Diode Laser Arrays to an Optical Fiber by Geometric Multiplexing	T. Y. Fan	<i>Appl. Opt.</i> 30 , 630 (1991)
Thermal Analysis and Control for Sputtering Deposition of High-T _c Superconducting Films	M. I. Flik* B. I. Choi* A. C. Anderson A. C. Westerheim	<i>In Transport Phenomena in Materials Processing-1990</i> , HTD-Vol. 146 (American Society of Mechanical Engineers, New York, 1990), p. 73
Capacitance-Voltage Measurements on Metal-SiO ₂ -Diamond Structures Fabricated with (100)- and (111)-Oriented Substrates	M. W. Geis J. A. Gregory B. B. Pate*	<i>IEEE Trans. Electron Devices</i> 38 , 619 (1991)
Analog Signal Correlator Design and Operation	J. B. Green M. Bhushan	<i>IEEE Trans. Magn.</i> 27 , 3380 (1991)

* Author not at Lincoln Laboratory.

Resistivity of Bulk InP	G. W. Iseler	In <i>Properties of Indium Phosphide</i> , Emiss Data Review Series, No. 6 (The Institution of Electrical Engineers, Hertfordshire, England, 1991), p. 25
Suppression of Laser Spiking by Intracavity Second-Harmonic Generation	T. H. Jeys	<i>Appl. Opt.</i> 30 , 1011 (1991)
Optical Modulators for Fiber-Optic Sensors	L. M. Johnson	In <i>Fiber-Optic Sensors: An Introduction for Engineers and Scientists</i> , edited by E. Udd (Wiley, New York, 1991), p. 99
Integrated-Optical Modulators for Bandpass Analog Links	L. M. Johnson G. E. Betts H. V. Roussel	<i>Proc. SPIE</i> 1371 , 2 (1990)
Low Noise dc SQUIDs Fabricated in Nb-Al ₂ O ₃ -Nb Trilayer Technology	M. B. Ketchen* M. Bhushan S. B. Kaplan* W. J. Gallagher*	<i>IEEE Trans. Magn.</i> 27 , 3005 (1991)
Ultrafast Shallow-Buried-Channel CCD's with Built-in Drift Fields	A. L. Lattes S. C. Munroe M. M. Seaver	<i>IEEE Electron Device Lett.</i> 12 , 104 (1991)
Heat Driven Cryocooler for Satellite Bus Use	R. M. Lerner	<i>Proceedings of the Sixth International Cryocoolers Conference</i> , Vol. II (David Taylor Research Center, Bethesda, Maryland, 1991), p. 273
Prevention of In Evaporation and Preservation of Smooth Surface in Thermal Annealing and Mass Transport of InP	Z. L. Liao	<i>Appl. Phys. Lett.</i> 58 , 1869 (1991)

* Author not at Lincoln Laboratory.

High- T_c Superconductive Microwave Filters	W. G. Lyons R. R. Bonetti* A. E. Williams* P. M. Mankiewicz* M. L. O'Malley* J. M. Hamm A. C. Anderson R. S. Withers A. Meulenberg* R. E. Howard*	<i>IEEE Trans. Magn.</i> 27 , 2537 (1991)
High- T_c Superconductive Delay Line Structures and Signal Conditioning Networks	W. G. Lyons R. S. Withers J. M. Hamm A. C. Anderson P. M. Mankiewicz* M. L. O'Malley* R. E. Howard*	<i>IEEE Trans. Magn.</i> 27 , 2932 (1991)
Surface Impedance Measurements of $YBa_2Cu_3O_{7-x}$ Thin Films in Stripline Resonators	D. E. Oates A. C. Anderson	<i>IEEE Trans. Magn.</i> 27 , 867 (1991)
Surface Impedance Measurements of Superconducting NbN Films	D. E. Oates A. C. Anderson C. C. Chin J. S. Derov* G. Dresselhaus* M. S. Dresselhaus*	<i>Phys. Rev. B</i> 43 , 7655 (1991)
Frequency-Modulated Nd:YAG Laser	P. A. Schulz S. R. Henion	<i>Opt. Lett.</i> 16 , 578 (1991)
Ferroelectric Thin Film Ultrasonic Micromotors	K. R. Udayakumar* S. F. Bart* A. M. Flynn* J. Chen* L. S. Tavrow* L. E. Cross* R. A. Brooks* D. J. Ehrlich	<i>Proceedings IEEE Micro Electro Mechanical Systems</i> (IEEE, New York, 1991), p. 109

* Author not at Lincoln Laboratory.

AlInGaAs/AlGaAs Strained Single-Quantum-Well Diode Lasers	C. A. Wang J. N. Walpole H. K. Choi L. J. Missaggia	<i>IEEE Photon. Technol. Lett.</i> 3 , 4 (1991)
Off-Axis Magnetron Sputtering of YBCO Films: The Influence of Atomic Oxygen	A. C. Westerheim L. S. Yu-Jahnes A. C. Anderson	<i>IEEE Trans. Magn.</i> 27 , 1001 (1991)
The Effects of Spatial Hole Burning and Energy Diffusion on the Single-Mode Operation of Standing-Wave Lasers	J. J. Zayhowski	<i>IEEE J. Quantum Electron.</i> 26 , 2052 (1990)
Q-Switched Operation of Microchip Lasers	J. J. Zayhowski	<i>Opt. Lett.</i> 16 , 575 (1991)

ACCEPTED FOR PUBLICATION

Measurement of a Critical Dependence on Background Electron Concentration of the Intersubband Transition of Cross-Gap Generated Carriers in Quantum Wells	E. R. Brown K. A. McIntosh K. B. Nichols J. W. Bales	<i>Phys. Rev. Lett.</i>
Room-Temperature CW Operation of GaAs-AlGaAs Diode Lasers on Silicon-on-Insulator Wafers	H. K. Choi C. A. Wang N. H. Karam*	<i>IEEE Photon. Technol. Lett.</i>
Production of Large-Area Mosaic Diamond Films Approaching Single-Crystal Quality	M. W. Geis H. I. Smith	<i>Appl. Phys. Lett.</i>
Silylation of Focused Ion Beam Exposed Resists	M. A. Hartney D. C. Shaver M. I. Shepard* J. S. Huh* J. Melngailis	<i>Appl. Phys. Lett.</i>
Room Temperature Diode-Pumped Yb:YAG Laser	P. Lacovara H. K. Choi C. A. Wang R. L. Aggarwal T. Y. Fan	<i>Opt. Lett.</i>

* Author not at Lincoln Laboratory.

Ultrafast, Room-Temperature, Resonance-Enhanced Third-Order Optical Susceptibility $\chi^{(3)}$ Tensor of AlGaAs/GaAs Quantum Well	H. Q. Le S. DiCecca	<i>Opt. Lett.</i>
Scalable High-Power Optically Pumped GaAs Laser	H. Q. Le S. DiCecca A. Mooradian	<i>Appl. Phys. Lett.</i>
Microstructure of Annealed Low- Temperature-Grown GaAs Layers	Z. Liliental-Weber* A. Calverie* J. Washburn* F. W. Smith A. R. Calawa	<i>Appl. Phys. Lett.</i>
Stripline Resonator Measurements of Z_s vs H_{rf} in $\text{YBa}_2\text{Cu}_3\text{O}_{7-x}$ Thin Films	D. E. Oates A. C. Anderson D. M. Sheen* S. M. Ali*	<i>IEEE Trans. Microwave Theory Tech.</i>
Current Distribution, Resistance, and Inductance for Superconducting Strip Transmission Lines	D. M. Sheen* S. M. Ali* D. E. Oates R. S. Withers J. A. Kong*	<i>IEEE Trans. Appl. Superconduct.</i>
Long-Wavelength $\text{Ge}_x\text{Si}_{1-x}\text{Si}$ Heterojunction Infrared Detectors and 400×400 -Element Imager Arrays	B.-Y. Tsaur C. K. Chen S. A. Marino	<i>IEEE Electron Device Lett.</i>
AlInGaAs/AlGaAs Separate- Confinement Heterostructure Strained Single-Quantum-Well Diode Lasers Grown by Organometallic Vapor Phase Epitaxy	C. A. Wang J. N. Walpole L. J. Missaggia J. P. Donnelly H. K. Choi	<i>Appl. Phys. Lett.</i>
Polarization-Switchable Microchip Lasers	J. J. Zayhowski	<i>Appl. Phys. Lett.</i>

*Author not at Lincoln Laboratory.

PRESENTATIONS[†]

Formation of Submicrometer Carbonaceous Islands During SEM Examination of Thin GaAs Layers on Si Substrates	G. W. Turner P. M. Nitishin	The Microphysics of Surfaces: Beam-Induced Processes Topical Meeting, Santa Fe, New Mexico, 11-14 February 1991
A CCD Programmable Image Processor	A. M. Chiang J. R. LaFranchise	1991 IEEE International Solid-State Circuits Conference, San Francisco, California, 13-15 February 1991
Microwave Semiconductor Devices	R. A. Murphy M. A. Hollis	Lincoln Laboratory Technical Seminar Series: University of Illinois, Champaign-Urbana, Illinois, 20 February 1991; University of Rochester, Rochester, New York, 20 March 1991
OMVPE of GaAs/AlGaAs and InGaAs/AlGaAs for Quantum-Well Diode Lasers	C. A. Wang	Lincoln Laboratory Technical Seminar Series, University of Southern California, Los Angeles, California, 22 February 1991
Quantum Efficiency Model for p^+ Doped Back-Illuminated CCD Imager	C. M. Huang J. R. Theriault E. T. Hurley B. W. Johnson B. E. Burke J. A. Gregory B. B. Kosicki	Symposium on Electronic Imaging Science and Technology, San Jose, California, 24 February – 1 March 1991

[†] Titles of presentations are listed for information only. No copies are available for distribution.

Insulating Layer for Device Isolation in GaAs Semiconductor Integrated Circuits	A. R. Calawa F. W. Smith	Lincoln Laboratory Technical Seminar Series, University of Michigan, Ann Arbor, Michigan, 25 March 1991
Wafer-Scale Solid-State Mass-Memory System	T. M. Lyszczarz	VLSI Seminar, Massachusetts Institute of Technology, Cambridge, Massachusetts, 26 February 1991
Recent Advances in Resonant- Tunneling Diode Oscillators	E. R. Brown C. D. Parker	NASA Space Terahertz Symposium, California Institute of Technology, Pasadena, California, 26-28 February 1991
The Future of Superconducting Electronics	R. W. Ralston	1991 Solid State Sciences Forum, Washington, D.C., 28 February 1991
Consortium for Superconducting Electronics: Overview of Technical Programs	R. W. Ralston	Washington Materials Forum, Washington, D.C., 28 February-1 March 1991
Evaluation of Phenolic Resists for 193-nm Surface Imaging	M. A. Hartney A. Spencer* D. W. Johnson*	} SPIE Symposium on Microlithography '91, San Jose, California, 3-8 March 1991
Polysilyne Resists for 193-nm Excimer Laser Lithography	R. R. Kunz M. W. Horn R. B. Goodman R. R. Paladugu P. A. Bianconi* D. A. Smith* C. A. Freed*	
Techniques for Implementation of High-Speed Free-Space Optical Interconnections	D. Z. Tsang	

*Author not at Lincoln Laboratory.

High-Frequency Analog Signal
Processing with High-Temperature
Superconductors

W. G. Lyons
R. S. Withers
J. M. Hamm
R. H. Mathews
B. J. Clifton
P. M. Mankiewicz*
M. L. O'Malley*
N. Newman*

OSA Topical Meeting on
Picosecond Electronics and
Optoelectronics,
Salt Lake City, Utah,
13-15 March 1991

Terahertz Time-Domain Transmission
of Superconductors

M. Nuss*
P. M. Mankiewicz*
M. L. O'Malley*
K. W. Goossen*
H. Roskos*
B. Tell*
M. Bhushan

CW Operation of a Diode-
Pumped Rotating Nd:Glass
Disk Laser

J. Korn
T. H. Jeys
T. Y. Fan

Room Temperature InGaAs
Diode-Pumped Yb:YAG Laser

P. Lacovara
C. A. Wang
H. K. Choi
R. L. Aggarwal
T. Y. Fan

Advanced Solid State
Lasers Meeting,
Hilton Head, South Carolina,
18-20 March 1991

Q-Switched Microchip Lasers

J. J. Zayhowski

High Resolution Far Infrared Laser
Magnetospectroscopy of Donor States
in GaAs/(GaAl)As Quantum Wells

E. R. Mueller*
D. M. Larsen*
J. Waldman*
W. D. Goodhue
J. W. Bales

March Meeting of the
American Physical Society,
Cincinnati, Ohio,
18-22 March 1991

High Frequency Applications of
Superconducting Electronics

R. W. Ralston

OMVPE of GaAs/AlGaAs and
InGaAs/AlGaAs for Quantum-Well
Diode Lasers

C. A. Wang

Seminar, Spire Corporation,
Bedford, Massachusetts,
19 March 1991

*Author not at Lincoln Laboratory.

Optimization of Modulators for Analog Applications	G. E. Betts L. M. Johnson	High-Speed/High-Frequency Optoelectronics, Palm Coast, Florida, 21 March 1991
Microwave Transistors—A Review	M. A. Hollis	Meeting, IEEE Electron Devices and Microwave Theory and Techniques Societies, Waltham, Massachusetts, 21 March 1991
Surface Imaging Lithography	M. A. Hartney	Soft X-Ray Projection Lithography, Monterey, California, 3-8 April 1991
Diode-Pumped Solid State Lasers: The Microchip Laser—A Case Study	J. J. Zayhowski	Norwegian Electro-Optics 1991, Nord-Torpa, Norway, 4-7 April 1991
High-Frequency InP/InGaAs <i>pin</i> Photodiodes with Efficient Response at Short Wavelengths	V. Diadiuk S. B. Alexander S. H. Groves D. L. Spears	Third International Conference on InP and Related Materials, Cardiff, Wales, 8-10 April 1991
Optical Wavefront Phase Tilt Measurement and Correction Using AlGaAs Integrated Guided-Wave Components	S. D. Lau J. P. Donnelly C. A. Wang R. B. Goodman R. H. Rediker	Integrated Photonics Research Topical Meeting, Monterey, California, 9-11 April 1991
Microwave and Millimeter-Wave Resonant Tunneling Devices	T. C. L. G. Sollner E. R. Brown W. D. Goodhue	Lincoln Laboratory Technical Seminar Series, University of Illinois, Champaign-Urbana, Illinois, 10 April 1991

Buried Heterostructure
InGaAs/GaAs/GaInP Strained-Layer
Quantum Well Lasers Fabricated
by Mass Transport

S. C. Palmateer
S. H. Groves
Z. L. Liao
J. N. Walpole

OMVPE Regrowth of CH₃I-Vapor-
Etched GaAs

C. A. Wang
C. W. Krueger
M. Flytzani-
Stephanopoulos*
R. A. Brown*

2-5 μ m Diode Laser Development

S. J. Eglash
H. K. Choi
G. W. Turner

Production of Large-Area Mosaic
Diamond Films Approaching
Single-Crystal Quality

M. W. Geis
H. I. Smith

Characterization of LPCVD
Silicon Nitride Using Experimental
Design

J. A. Gregory
D. J. Young
R. W. Mountain
C. L. Doherty

Modeling of the Reactive Sputtering
Process and Comparison with
Experimental Results

D. J. Lichtenwalner
A. C. Anderson
D. A. Rudman*

Fifth Biennial Workshop on
Organometallic Vapor Phase
Epitaxy,
Panama City Beach, Florida,
14-17 April 1991

Fourth Annual Diode Laser
Technology Program
Conference,
Clinton, Maryland,
16-18 April 1991

International Conference on
Metallurgical Coatings and
Thin Films,
San Diego, California,
22-26 April 1991

* Author not at Lincoln Laboratory.

ORGANIZATION

SOLID STATE DIVISION

A. L. McWhorter, *Head*
I. Melngailis, *Associate Head*
E. Stern, *Associate Head*
J. F. Goodwin, *Assistant*

D. J. Ehrlich, *Senior Staff*
N. L. DeMeo, Jr., *Associate Staff*
J. W. Caunt, *Assistant Staff*
K. J. Challberg, *Administrative Staff*

SUBMICROMETER TECHNOLOGY

D. C. Shaver, *Leader*
M. Rothschild, *Assistant Leader*

Astolfi, D. K.
Craig, D. M.
Dennis, C. L.
DiNatale, W. F.
Doran, S. P.
Efremow, N. N., Jr.
Forte, A. R.
Gajar, S. A.*
Geis, M. W.

Goodman, R. B.
Hartney, M. A.
Horn, M. W.
Kunz, R. R.
Lyszczarz, T. M.
Maki, P. A.
Melngailis, J.[†]
Sedlacek, J. H. C.
Uttaro, R. S.

QUANTUM ELECTRONICS

A. Mooradian, *Leader*
P. L. Kelley, *Associate Leader*
A. Sanchez-Rubio, *Assistant Leader*

Aggarwal, R. L.
Barch, W. E.
Cook, C. C.
Daneu, V.
DeFeo, W. E.
DiCecca, S.
Dill, C. D., III
Fan, T. Y.
Hancock, R. C.
Henion, S. R.
Hotaling, T. C.
Hsu, L.*

Jeys, T. H.
Korn, J. A.
Lacovara, P.
Le, H. Q.
Menyuk, N.[‡]
Nabors, C. D.
Ochoa, J. R.
Schulz, P. A.
Sullivan, D. J.
Wall, K. F.
Zayhowski, J. J.

ELECTRONIC MATERIALS

A. J. Strauss, *Leader*
B-Y. Tsaur, *Associate Leader*

Anderson, C. H., Jr.
Button, M. J.
Chen, C. K.
Choi, H. K.
Clark, H. R., Jr.
Connors, M. K.
Eg lash, S. J.
Fahey, R. E.
Finn, M. C.
Iseler, G. W.

Kolesar, D. F.
Krohn, L., Jr.
Marino, S. A.
Mastromattei, F. L.
McGilvary, W. L.
Nitishin, P. M.
Pantano, J. V.
Turner, G. W.
Wang, C. A.

HIGH SPEED ELECTRONICS

R. A. Murphy, *Leader*
M. A. Hollis, *Assistant Leader*
R. W. Chick, *Senior Staff*

Actis, R.
Bales, J. W.*
Barlas, A. D.
Bergeron, N. J.
Bozler, C. O.
Brown, E. R.
Calawa, A. R.
Chen, C. L.
Clifton, B. J.
Crenshaw, D. L.*
Gladden, D. B.[‡]
Goodhue, W. D.
Gray, R. V.
Lincoln, G. A., Jr.

Mahoney, L. J.
Manfra, M. J.
Mathews, R. H.
Mattia, J. P.*
McIntosh, K. A.
McMorran, R. A.
McNamara, M. J.
Nichols, K. B.
Parker, C. D.
Rabe, S.
Rathman, D. D.
Smith, F. W., III
Vera, A.

* Research Assistant

[†] Part Time

[‡] Staff Associate

ELECTROOPTICAL DEVICES

R. C. Williamson, *Leader*
D. L. Spears, *Assistant Leader*
R. H. Rediker, *Senior Staff*

Aull, B. F. [†]	Missaggia, L. J.
Bailey, R. J.	Mull, D. E.
Barwick, D. S.*	O'Donnell, F. J.
Betts, G. E.	Palmacci, S. T.
Corcoran, C. J.*	Palmateer, S. C.
Cox, C. H., III	Pheiffer, B. K.*
Diadiuk, V.	Rauschenbach, K.
Donnelly, J. P.	Reeder, R. E.
Ferrante, G. A.	Roussell, H. V.
Groves, S. H.	Shiple, S. D.*
Harman, T. C.	Tsang, D. Z.
Hovey, D. L.	Walpole, J. N.
Johnson, L. M.	Woodhouse, J. D.
Liau, Z. L.	Yee, A. C.
Lind, T. A.	

ANALOG DEVICE TECHNOLOGY

R. W. Ralston, *Leader*
R. S. Withers, *Associate Leader*
T. C. L. G. Sollner, *Assistant Leader*
A. C. Anderson, *Senior Staff*
R. M. Lerner, *Senior Staff*[†]

Arsenault, D. R.	Lyons, W. G.
Bhushan, M.	Macedo, E. M., Jr.
Boisvert, R. R.	Minnick, R. G.
Brogan, W. T.	Oates, D. E.
Denneno, A. P.	Sage, J. P.
Fitch, G. L.	Seaver, M. M.
Green, J. B.	Slattery, R. L.
Hamm, J. M.	Westerheim, A. C.*
Holtham, J. H.	Whitley, D. B.
Lattes, A. L.	Yu-Jahnes, L. S.*

MICROELECTRONICS

E. D. Savoye, *Leader*
B. B. Kosicki, *Assistant Leader*
B. E. Burke, *Senior Staff*
A. M. Chiang, *Senior Staff*

Chuang, M. L.*	Felton, B. J.	Loomis, A. H.
Collins, I. K.	Gregory, J. A.	McGonagle, W. H.
Cooper, M. J.	Huang, C. M.	Mountain, R. W.
Daniels, P. J.	Hurley, E. T.	Percival, K. A.
Doherty, C. L., Jr.	Johnson, B. W.	Pichler, H. H.
Dolat, V. S.	Johnson, K. F.	Reich, R. K.
Donahue, T. C.	LaFranchise, J. R.	Reinold, J. H., Jr.
Durant, G. L.		Young, D. J.

* Research Assistant

[†] Part Time

[‡] Leave of Absence

1. ELECTROOPTICAL DEVICES

1.1 INTEGRATED-OPTICAL MODULATORS FOR AN ADAPTIVE NULLING SYSTEM

An optical adaptive nulling system is being developed for microwave/millimeter-wave multielement antenna systems [1]. A critical device requirement for this system is a set of high-speed electrooptic modulators with closely matched frequency responses. We have built and tested a pair of LiNbO_3 traveling-wave interferometric modulators meeting the nulling system requirements, with frequency responses that track each other to within 0.03 dB and 0.22° in amplitude and phase, respectively, over the 5- to 7-GHz frequency band.

A block diagram of a portion of the optical adaptive nulling system is shown in Figure 1-1. At the front end of the system, an optical carrier wave is intensity modulated by the electrical signal from each antenna element. Next, amplitude and phase weighting is implemented in the optical domain using optical modulators. The weighted optical signals are then combined and detected to provide the antenna output. The weights are set by control signals to achieve the desired antenna pattern and null placement.

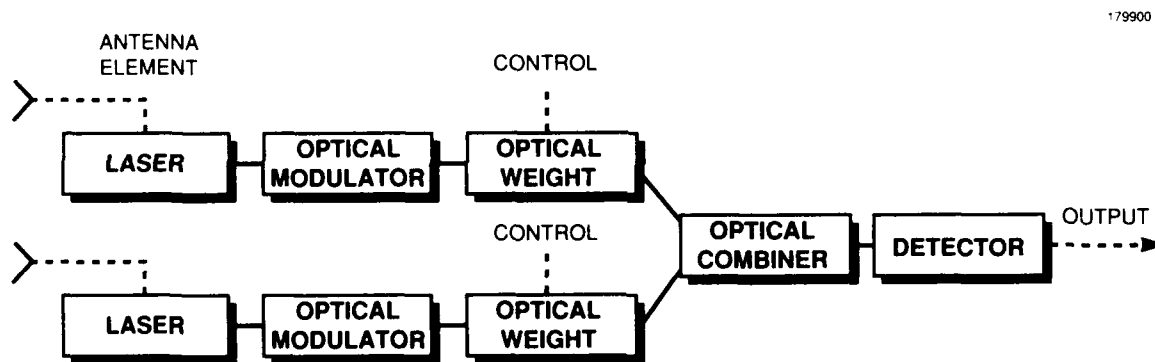


Figure 1-1. Block diagram of optical nulling system. Two channels are shown, with the solid lines and dashed lines indicating optical and electrical paths, respectively.

A key advantage of the optical adaptive nulling implementation is the reduction in the number of electrical components required to meet difficult channel-tracking specifications. To achieve 40-dB nulls, variations in the amplitude and phase response of each channel must track the variations of all other channels to within 0.1 dB and 0.8° , respectively, over the system bandwidth. To meet this condition, the weights must provide nearly uniform amplitude and phase offsets across the system frequency range. While this requirement is difficult to achieve working entirely in the electrical domain, channel tracking is relatively simple to obtain using optical components because the system electrical bandwidth is very

small compared with the optical carrier frequency. For example, amplitude weighting is easily achieved with an adjustable optical attenuator, ensuring uniform weighting over a multigigahertz optical modulation bandwidth.

The potential advantages of an optical nulling system can only be realized if the front-end electrooptic modulators meet the required channel-tracking performance. Channel tracking was confirmed over the 5- to 7-GHz frequency band using LiNbO_3 traveling-wave modulators designed for operation at $1.3\ \mu\text{m}$. The traveling-wave electrode interaction length was 9 mm, which provided good response over the frequency band. Following the active modulator portion of the electrode structure was a long transmission line section with moderate attenuation which, along with matched termination resistors, minimized the effect of reflected electrical signals. This design feature contributed to providing a well-defined and reproducible frequency response.

The modulators were tested in a simple optical link arrangement consisting of a CW laser, optical modulator, and detector. Network analyzer S_{21} measurements were taken between the electrical input to the modulator and the electrical output of the detector. Two modulators, built separately but with identical fabrication parameters, were tested and the results are shown in Figure 1-2. Amplitude and phase tracking is achieved to within 0.03 dB and 0.22° , respectively. This performance offers the possibility of achieving null depths of between 45 and 50 dB in an optical nulling system.

L. M. Johnson
H. V. Roussel
G. E. Betts

W. K. Hutchinson
A. Sonnenschein

1.2 SELF-ALIGNED FABRICATION TECHNIQUE FOR TWO-DIMENSIONAL SURFACE-EMITTING DIODE LASER ARRAYS

Monolithic two-dimensional AlGaAs surface-emitting laser arrays with external deflecting mirrors have been made using a new fabrication process that self-aligns the deflecting mirrors to the facets in order to reduce alignment tolerances. This process, which is also applicable to other diode laser materials systems, allows the fabrication of large ($1\ \text{cm}^2$) arrays with high efficiency. Performance data on dry-etched edge-emitting and surface-emitting monolithic laser arrays are presented.

The basic design of the two-dimensional monolithic laser arrays has been described previously [2],[3]. A combination of straight and angled dry etching is used to produce arrays of edge-emitting horizontal-cavity lasers that deflect the radiation normal to the surface, as shown schematically in Figure 1-3. The laser material structure, laser geometry, and external deflecting mirror design have been improved to achieve higher external differential quantum efficiencies and lower threshold current densities.

The arrays are fabricated from graded-index separate-confinement heterostructure single-quantum-well (GRINSCH-SQW) AlGaAs material grown by organometallic vapor phase epitaxy (OMVPE). The 10-nm-thick quantum well contains 7% AlAs. The GRIN regions on both sides of the quantum well are graded from 30 to 60% AlAs over $\sim 200\ \text{nm}$, making the total confinement region $\sim 410\ \text{nm}$ thick. Typically, the threshold current density is $200\ \text{A}/\text{cm}^2$, the external differential quantum efficiency is 40% per facet, and the full width at half-maximum (FWHM) of the beam is $< 35^\circ$ [4].

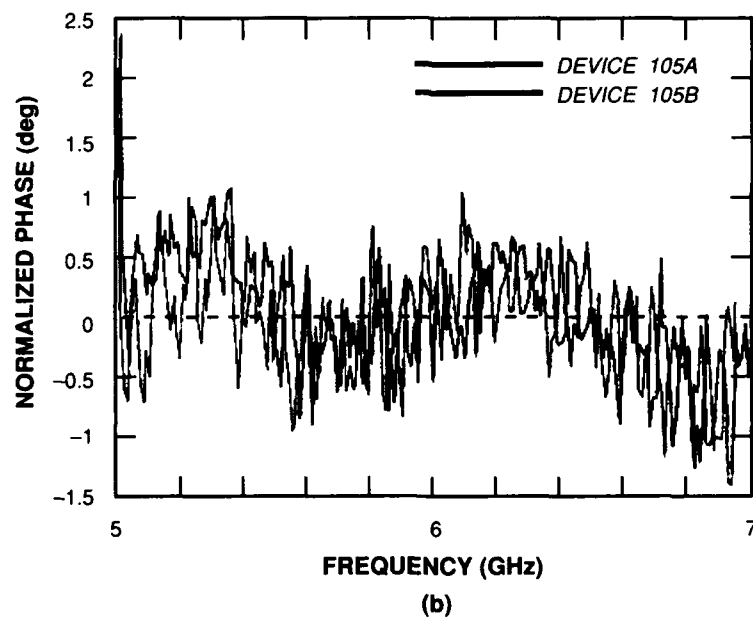
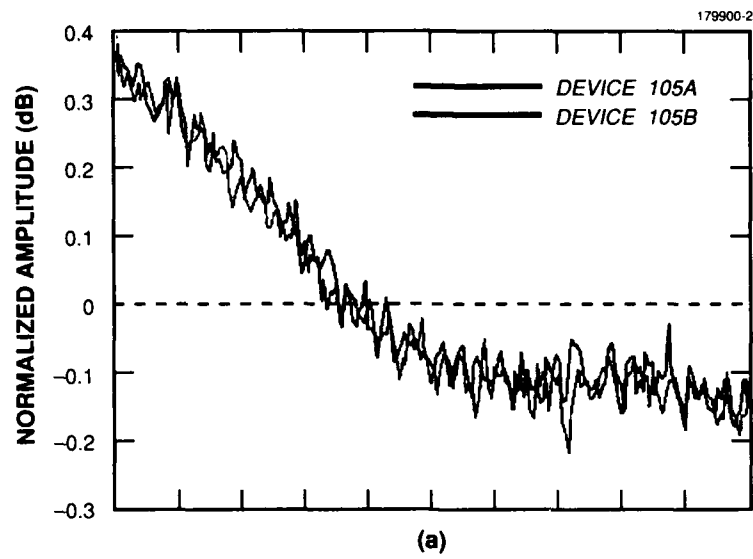


Figure 1-2. Measured (a) amplitude and (b) phase response of two lithium niobate traveling-wave modulators.

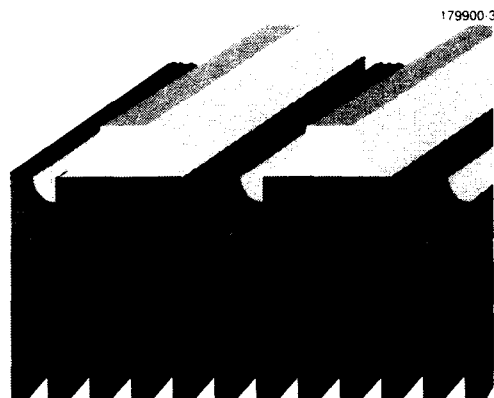


Figure 1-3. Schematic diagram of the geometry of the monolithic laser array.

The laser geometry has been optimized for high-power operation [5]. The laser cavity length is 1 mm, and the laser stripes are $45\text{ }\mu\text{m}$ wide on $85\text{-}\mu\text{m}$ centers. The collection efficiency of our latest devices has been increased by modifying the deflector geometry. The junction depth is increased to $2.5\text{ }\mu\text{m}$, the facet-deflector spacing is reduced to $1.5\text{ }\mu\text{m}$, and the distance between the facet and the top of the deflecting mirror is reduced to $4.5\text{ }\mu\text{m}$ after coating. The f-number of the parabolic deflecting mirror is ~ 0.85 .

To obtain high collection efficiency, the deflectors must be aligned to the facets with a tolerance $< 0.5\text{ }\mu\text{m}$ [3]. Maintaining this alignment precision over a 1-cm^2 array is difficult. A self-aligned fabrication process has been developed to reduce the alignment error, as illustrated in Figure 1-4. A 70-nm nickel mask, fabricated with a conventional lift-off technique, is used to define the edges of both laser facets and both deflecting mirrors. The boundary of the laser facets is defined with an additional photoresist mask, and the facets are etched to a depth of $4\text{ }\mu\text{m}$ by ion-beam-assisted etching (IABE). The two parabolic deflecting mirrors are fabricated separately. A photoresist mask is placed over the nickel mask to protect both facets so only the region to be etched is exposed. The deflecting mirror is etched using a high-precision computer-controlled tiltable sample holder.

Once the laser facets and deflecting mirrors are etched, the facets and parabolas are masked with photoresist and the nickel etch mask is removed with HCl. Next, Ti/Au *p*-type contact and deflecting mirror metallizations are deposited with two successive angle evaporation and metal lift-off steps. A shallow proton bombardment patterned with a photoresist mask confines the current to $45\text{-}\mu\text{m}$ -wide stripes on $85\text{-}\mu\text{m}$ centers, while a deep proton bombardment midway between the laser stripes introduces enough optical loss to prevent transverse lasing. Finally, the substrate of the laser is thinned to $\sim 75\text{ }\mu\text{m}$ and a AuGe *n*-type contact is deposited and then alloyed using a rapid thermal alloying system.

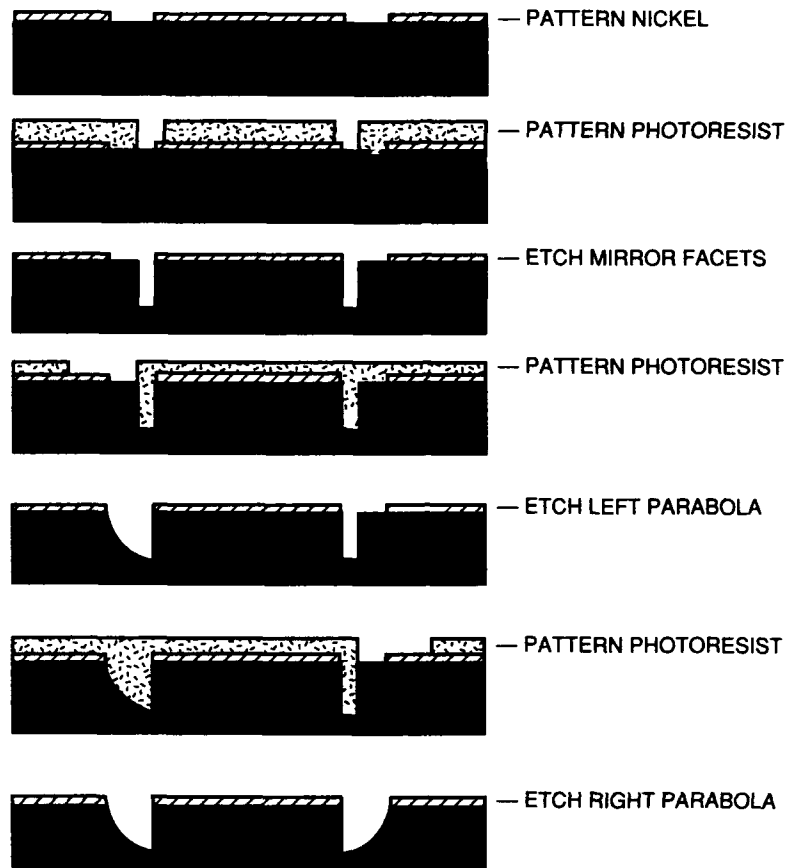


Figure 1-4. Self-aligned process for fabricating the laser facets and parabolic deflecting mirrors.

The masking and facet-etching techniques have been evaluated by fabricating broad-area etched-facet lasers and cleaving them in close proximity to the etched facets. Lasers with two etched facets are found to have efficiencies and threshold current densities comparable with cleaved lasers. The light output power vs current characteristics of a typical etched-facet edge-emitting laser is shown in Figure 1-5. This laser has a threshold current density of 250 A/cm^2 and a differential quantum efficiency of 39% per facet.

Initial results for surface-emitting lasers made using the self-aligned deflector fabrication process are very encouraging. A near-field pattern of two rows of 24 surface-emitting lasers is pictured in Figure 1-6. The light output power of one row is shown in Figure 1-7. The threshold current density is $\sim 250 \text{ A/cm}^2$ and the differential quantum efficiency is $\sim 31\%$. The low quantum efficiency of the etched-facet

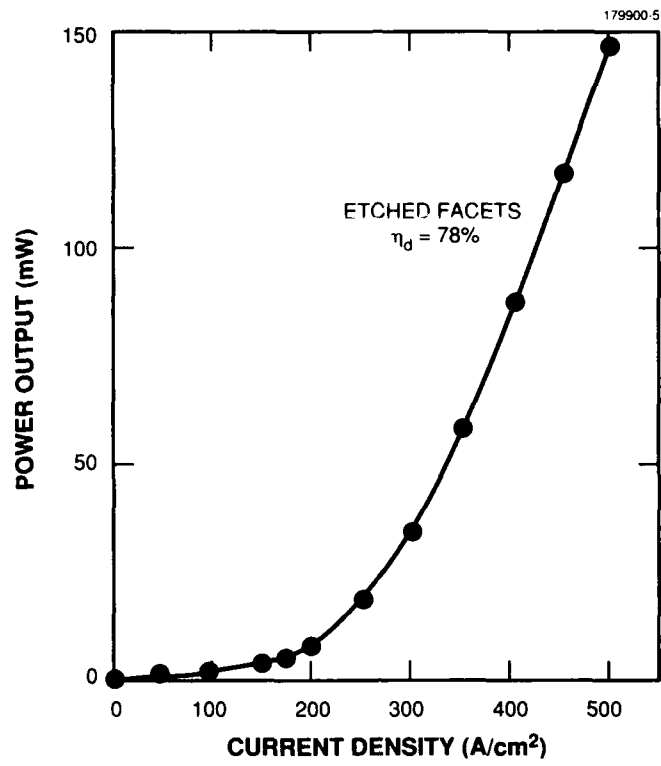


Figure 1-5. Power output vs current for an etched-facet edge-emitting laser.

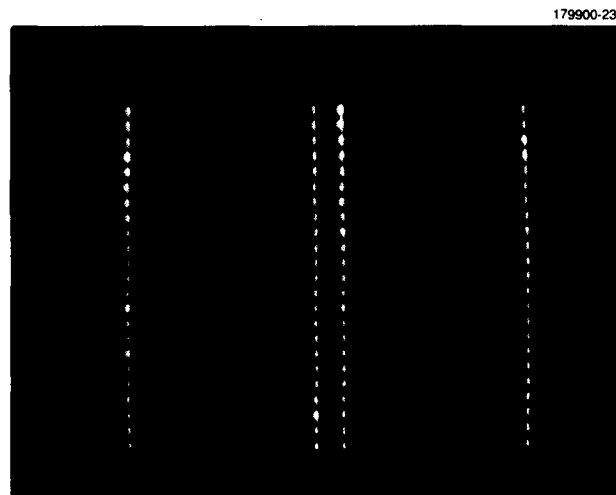


Figure 1-6. Near-field pattern of two rows of 24 surface-emitting lasers.

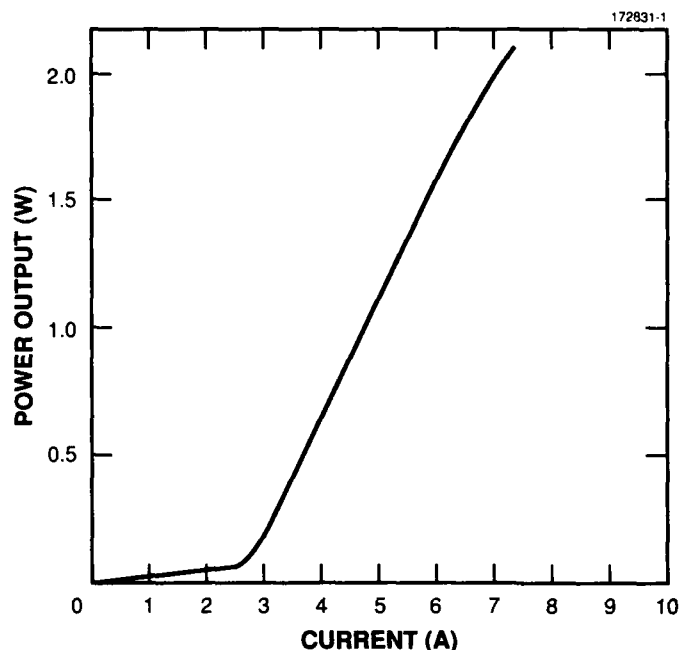


Figure 1-7. Power output vs current for a monolithic surface-emitting laser array.

surface-emitting lasers compared with the etched-facet edge-emitting lasers is attributed to facet roughness produced during the additional processing steps. After these devices were made, we discovered that the unprotected AlGaAs at the mirror facet was severely etched by the photoresist developer during the *p*-type metallization step. Efforts to protect the facet during this processing step are under way.

K. Rauschenbach

C. A. Wang

G. A. Ferrante

1.3 FABRICATION OF HIGH-EFFICIENCY TWO-DIMENSIONAL SURFACE-EMITTING InGaAs/AlGaAs AND AlInGaAs/AlGaAs DIODE LASER ARRAYS

The first demonstration of monolithic two-dimensional arrays of folded-cavity surface-emitting strained-layer InGaAs/AlGaAs and AlInGaAs/AlGaAs diode lasers is reported. These arrays, which use two 45° internal mirrors [6]-[8] and two top-surface facets, are fabricated with a self-aligned process and IBAE [9]. The InGaAs and AlInGaAs arrays emit at 1.03 and 0.815 μm , respectively, have low threshold current densities (between 160 and 240 A/cm²), and display differential quantum efficiencies as high as 56%.

The InGaAs/AlGaAs and AlInGaAs/AlGaAs wafers used for the arrays were grown by OMVPE and contain a single InGaAs or AlInGaAs quantum well symmetrically positioned in an optical cavity. The layer structures are similar to strained-layer InGaAs and AlInGaAs structures previously reported [10],[11]. We chose AlInGaAs over AlGaAs as the quantum-well material for 0.815- μm operation because preliminary investigations indicate that strained-layer AlInGaAs diode lasers have lower threshold current densities, may be less susceptible to processing-induced defects, and therefore may be more reliable than their counterparts with AlGaAs quantum wells.

The design of the laser arrays is shown schematically in Figure 1-8. Since total internal reflection occurs at the surface of the folding mirrors, high-reflectivity coating of the mirror surfaces is not required. Emission occurs through window regions in the top-surface facets at the ends of each laser element. Figure 1-9 is a scanning electron micrograph of an etched 45° cavity-folding mirror from one of the arrays. Optical pattern-generator masks, optical projection printing, and chlorine IBAE were used in this key fabrication step.

The arrays were evaluated during pulsed operation (100-ns pulses, 1-kHz repetition rate). Figure 1-10 shows the near-field pattern taken at about twice threshold for a AlInGaAs/AlGaAs array consisting of two rows of 24 elements each, all bonded in parallel. The SiO₂ encapsulation and the absorbing GaAs cap layers were removed from the top-surface facets in the AlInGaAs/AlGaAs arrays. The threshold

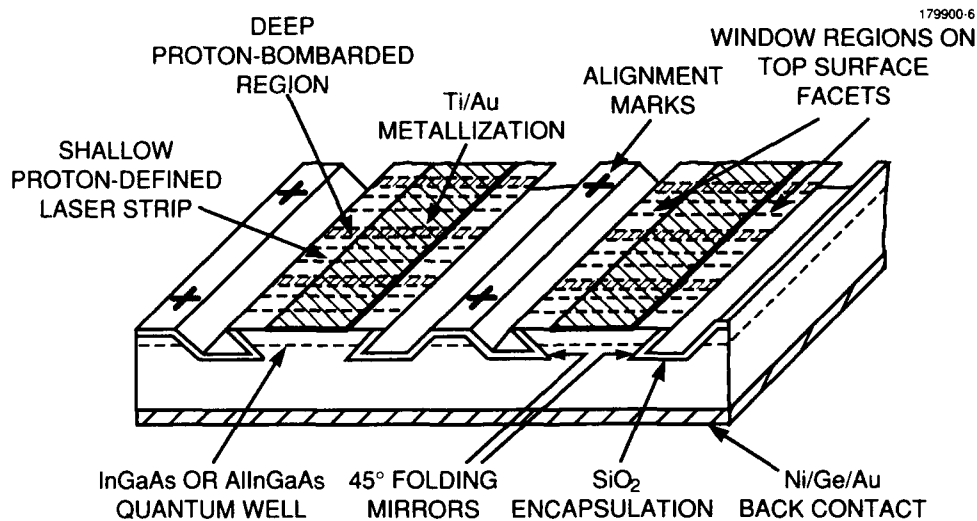


Figure 1-8. Schematic diagram of a monolithic two-dimensional surface-emitting array of strained-layer diode lasers. Each individual laser utilizes a folded cavity consisting of two 45° internal reflectors and two top-surface facets.

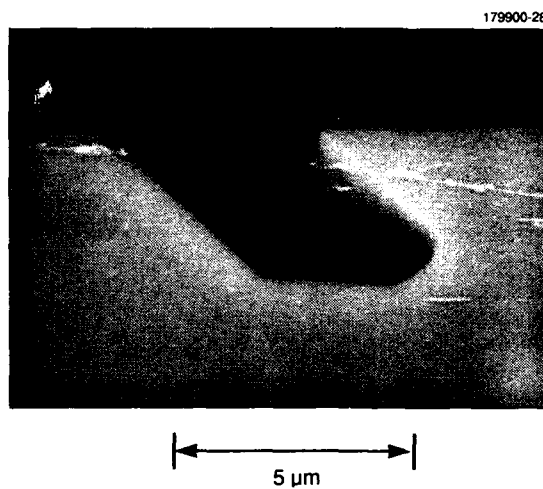


Figure 1-9. Scanning electron micrograph showing a 45° cavity-folding mirror from one of the AlInGaAs/AlGaAs arrays.

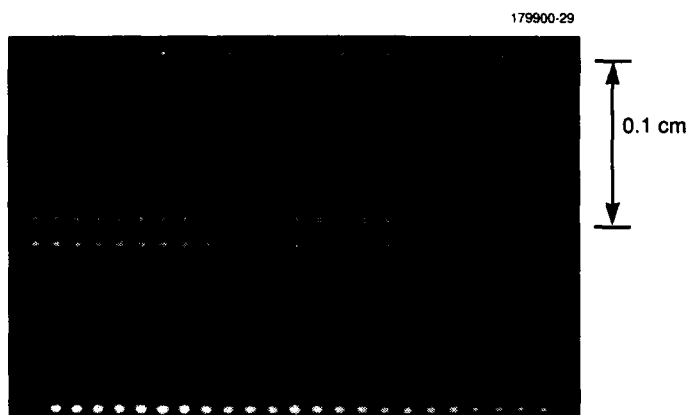


Figure 1-10. Near-field pattern of a 48-element AlInGaAs/AlGaAs array with differential quantum efficiency of 51%.

current for the best of these arrays, a 17-element device, is about 92 mA per laser, which corresponds to a threshold current density of 230 A/cm^2 . The peak output power was $\sim 15 \text{ W}$ at 20 A, and the differential quantum efficiency was $\sim 53\%$. We also measured a number of InGaAs/AlGaAs arrays. The best of these, a 16-element device, exhibited an average threshold current of $\sim 74 \text{ mA}$ per laser, which corresponds to a threshold current density of 185 A/cm^2 , and a differential quantum efficiency of $\sim 56\%$. A plot of output power vs current for this array is shown in Figure 1-11. These results indicate that it should be possible to make high-performance monolithic arrays over the entire wavelength range from 0.7 to $1.1 \mu\text{m}$.

W. D. Goodhue
J. P. Donnelly
C. A. Wang
G. A. Lincoln

K. Rauschenbach
R. J. Bailey
G. D. Johnson

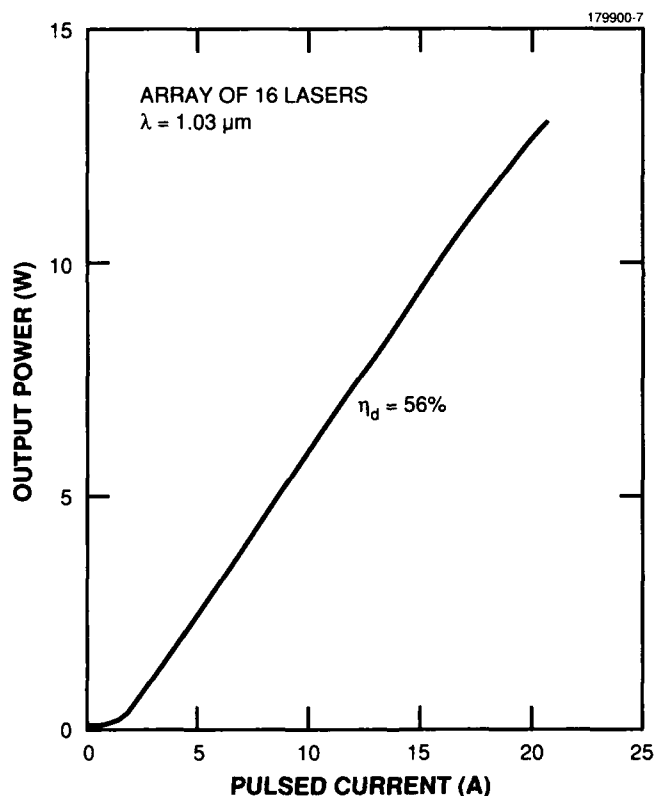


Figure 1-11. Pulsed output power vs current for a one-row, 16-element InGaAs/AlGaAs array. The current pulses were 100 ns wide at a 1-kHz repetition rate, and the differential quantum efficiency was $\sim 56\%$.

1.4 PROTON BOMBARDMENT OF $n\text{-Ga}_{0.51}\text{In}_{0.49}\text{P}$

Heterostructures epitaxially grown on GaAs play a major role in optoelectronic device technology. At present, most GaAs heterostructure devices are based on the AlGaAs/GaAs materials system. This system is relatively easy to grow because of the close match in lattice constant of GaAs and AlAs. Recently, interest has developed in using lattice-matched GaInAsP (which includes the ternary $\text{Ga}_{0.51}\text{In}_{0.49}\text{P}$) to replace AlGaAs. Elimination of Al-containing alloys would provide the device designer with fabrication techniques, such as etch and regrowth or mass transport, which are impossible or extremely limited in the AlGaAs/GaAs system. In addition, preliminary results indicate that this materials system may be more resistant to device degradation. Realizing the possibility that a whole range of new integrated-optical device structures could be based on these Al-free alloys, we have begun to investigate the potential use of proton bombardment and ion implantation in this system. In this section, some preliminary results on the use of proton bombardment to produce high-resistivity regions in $\text{Ga}_{0.51}\text{In}_{0.49}\text{P}$ are reported.

For these experiments, two different lattice-matched $\text{Ga}_{0.51}\text{In}_{0.49}\text{P}$ layers were grown on $n^+\text{-GaAs}$ ($n^+ = 2 \times 10^{18} \text{ cm}^{-3}$) substrates. The first was a nominally undoped layer ($n = 8 \times 10^{15} \text{ cm}^{-3}$) about $0.7 \mu\text{m}$ thick, while the second was a Si-doped layer ($n^+ = 1 \times 10^{18} \text{ cm}^{-3}$) about $1.0 \mu\text{m}$ thick. The epitaxial growth of GaInP/GaAs was performed by OMVPE using an atmospheric-pressure chimney reactor [12]. Uniform growth over a 50-mm-diam substrate was obtained by susceptor rotation. Growth was made at 650°C using GaAs substrates oriented 2° off (100) toward (110). Trimethylgallium, trimethylindium, arsine, and phosphine were used as precursors, and silane in H_2 was employed as the n -type dopant.

Prior to the proton bombardment a Ge/Au/Ni/Au alloyed ohmic contact was made to the back of the $n\text{-GaAs}$ substrate, and 20-mil-diam Ti/Au Schottky-barrier contacts (an array) were made to the surface of the GaInP layer. The Ti and Au were ~ 300 and 1000 \AA thick, respectively. The Schottky-barrier contacts facilitated capacitance-voltage (C-V) measurements for carrier-concentration depth profiling. After a repetitive series of C-V measurements and incremental-dose proton bombardments, the carrier compensation effects were evaluated by plotting the various concentration depth profiles on the same scale. These initial experiments used 100-keV protons, and the energy lost in the Ti/Au contacts was considered in determining the penetration depth of the protons.

Figure 1-12 shows the electron carrier concentration vs depth of a nominally undoped $n\text{-GaInP}$ epitaxial layer for incremental proton doses of $1 \times 10^{11} \text{ cm}^{-2}$. The uppermost curve is for an unimplanted sample, and the C-V data indicate that the zero-bias depletion region extends about $0.3 \mu\text{m}$ below the surface. The steep rise at about $0.7 \mu\text{m}$ is due to the $n^+\text{-GaAs}$ substrate. As the proton dose is increased, the carrier concentration decreases and the zero-bias depletion region extends deeper into the GaInP. Finally, at a dose of $4 \times 10^{11} \text{ cm}^{-2}$, the GaInP layer appears to be fully compensated. A second undoped sample, which was bombarded with a dose of $2 \times 10^{13} \text{ cm}^{-2}$, 100-keV H^+ , exhibited compensation that was thermally stable for an annealing cycle of 400°C for 30 min.

For the $n^+\text{-GaInP}$, changes in the carrier concentration were not observed until a total proton dose of $1 \times 10^{12} \text{ cm}^{-2}$ was attained. Each profile in Figure 1-13 represents a decrease in the electron carrier concentration that results from an incremental increase in dose of $2 \times 10^{12} \text{ cm}^{-2}$. Once a proton dose $\geq 1 \times 10^{13} \text{ cm}^{-2}$ is reached, the carrier concentration decreases dramatically, and the first $0.5 \mu\text{m}$ of the $n^+\text{-GaInP}$ becomes completely compensated after receiving an accumulated dose of $2 \times 10^{13} \text{ cm}^{-2}$. At higher doses ($1 \times 10^{14} \text{ cm}^{-2}$), the compensated thickness reaches about $0.6 \mu\text{m}$ and changes very little

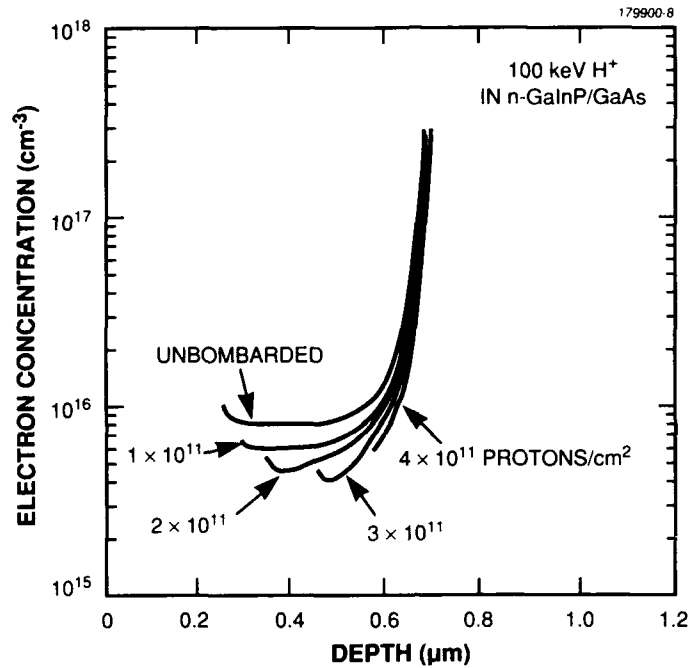


Figure 1-12. Electron carrier concentration vs depth obtained from C-V data of 100-keV, proton-bombarded n-GaInP for incremental doses of $1 \times 10^{11} \text{ cm}^{-2}$.

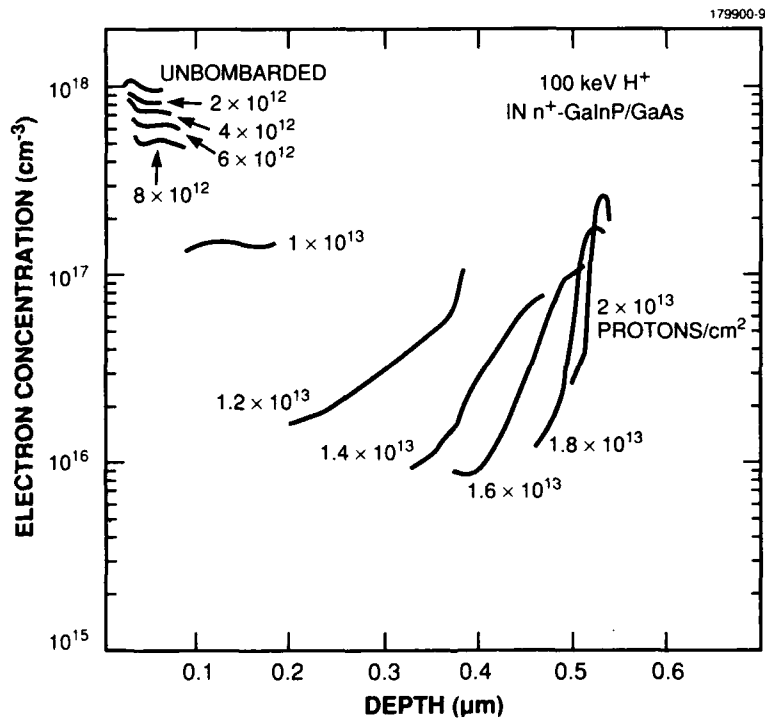


Figure 1-13. Electron carrier concentration vs depth obtained from C-V data of 100-keV proton-bombarded n⁺-GaInP for incremental doses of $2 \times 10^{12} \text{ cm}^{-2}$.

with further increases in dose. Up to a dose of $8 \times 10^{12} \text{ cm}^{-2}$, the change in carrier concentration appears to be fairly linear as a function of dose. A plot of Δn (change in carrier concentration) vs accumulated dose yields a carrier removal rate of about 5 electrons per proton-micrometer at a depth of $0.05 \mu\text{m}$ from the surface. Because of differences in experimental parameters, specific comparisons with other materials systems are hard to make, but this measure of the electron compensation rate in GaInP agrees very well with that observed in GaAs [13].

In conclusion, a preliminary investigation of the proton bombardment in n - and n^+ -GaInP indicates that highly compensated layers similar to those obtained in GaAs can be realized. This finding is encouraging from the viewpoint of being able to fabricate planar integrated-optical devices and circuits in this materials system. A more detailed study in both n - and p -type GaInP is being carried out to determine the energy-dependent resistivity as a function of depth as well as the thermal stability of these proton-bombarded layers.

J. D. Woodhouse

S. H. Groves

S. C. Palmateer

J. P. Donnelly

1.5 $\text{Ga}_{0.51}\text{In}_{0.49}\text{P}$ AS A REFERENCE CRYSTAL FOR (002) ROCKING CURVES OF AlGaAs LAYERED STRUCTURES

Superlattice (SL) and multiple-quantum-well (MQW) structures are valuable for studies of low-dimensional physics and for extracting information about crystal growth processes. Along with interference-stack structures, they are also finding application in electronic and optical devices. The structural evaluation of these layered materials is usually made with high-resolution x-ray diffraction. To be effective, however, the x-ray scattering from barrier and well materials must differ. If there is a lattice constant change (strained-layer structures), the layered nature of the structure produces the characteristic pattern with satellite peaks in the rocking curve. For lattice-matched structures, such as those made up of AlGaAs alloys, the situation is more difficult, and the necessary interference of diffracted beams to produce the satellite structure must come from different structure factors. In this case it is important to be able to select Bragg reflections such as the (002), in which reflections from the group III and group V sublattices are out of phase, to enhance the structure-factor difference. The double-crystal diffractometer is a commonly available instrument that is well suited for high-resolution studies. Unfortunately, a first crystal for (002)-reflection studies of GaAs-based materials has not been available. Here, we demonstrate that epitaxial $\text{Ga}_{0.51}\text{In}_{0.49}\text{P}$ (referred to as GaInP), which is lattice matched to GaAs, fills this need.

Figure 1-14 shows a simulated rocking curve, generated with RADS commercial software, of (004) and (002) Bragg reflections for a MQW with $\text{Al}_{0.5}\text{Ga}_{0.5}\text{As}$ barriers and GaAs quantum wells. Similar curves are obtained if the barrier material is GaInP. In the case of the (004) rocking curve, there is barely enough information to extract just the period and the average composition of the MQW. However, for the case of the (002) rocking curve, the compositions and thicknesses of the individual wells and barriers can be accurately determined from the abundant satellite structure. For the zinc blende lattice, the structure factors are $|F_{004}| = 4|f_{\text{III}} + f_{\text{V}}|$ and $|F_{002}| = 4|f_{\text{III}} - f_{\text{V}}|$, where f_{III} and f_{V} are the atomic scattering factors for the group III and group V elements, respectively. Because of the similarity in size of f_{Ga} and f_{As} , F_{002} for GaAs is small in comparison to that for $\text{Al}_{0.5}\text{Ga}_{0.5}\text{As}$. This enhances the contrast between layers for the (002) reflection, which in turn causes the many satellites in the (002) rocking curve.

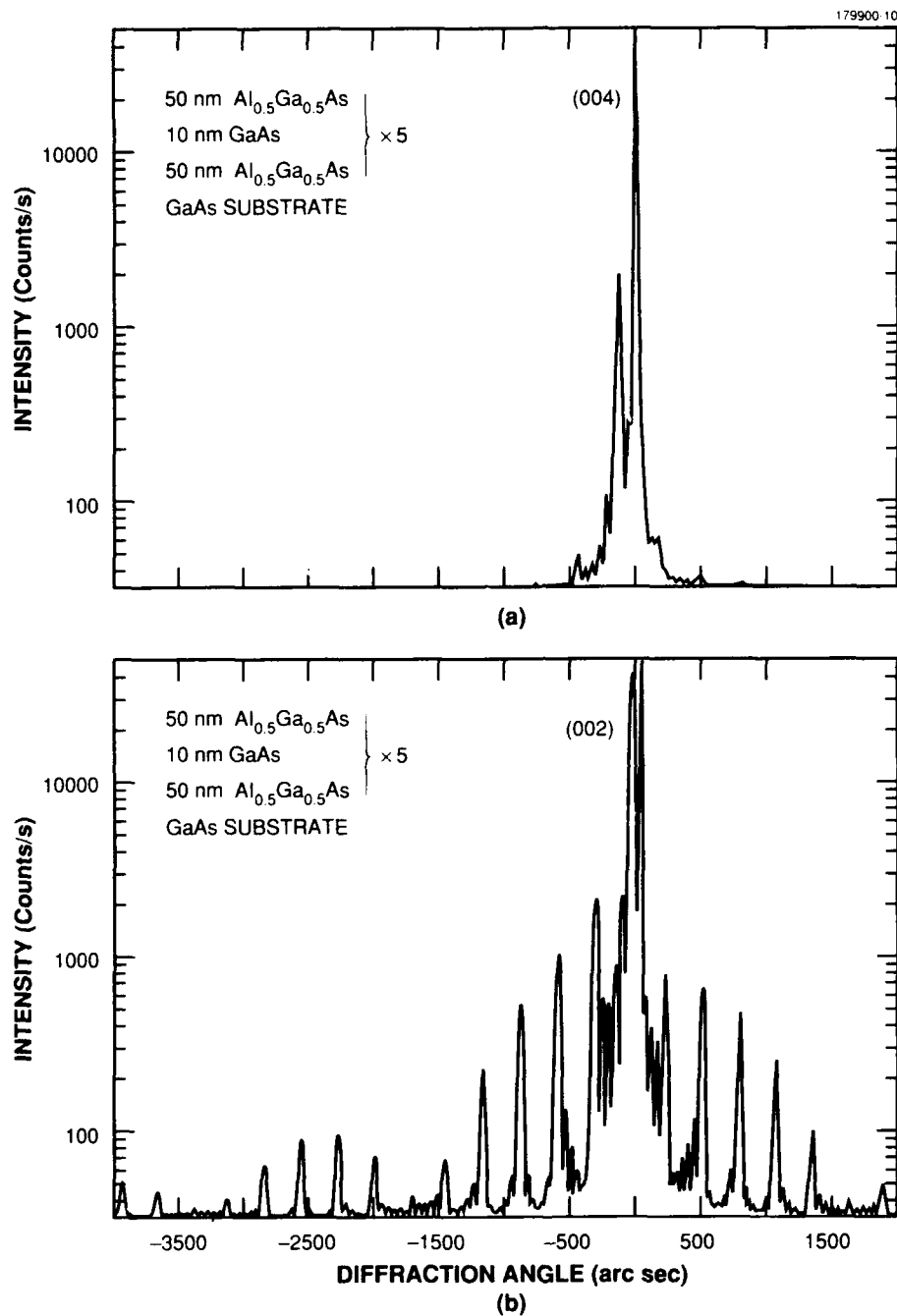


Figure 1-14. (a) Simulated (004) rocking curve of a MQW structure with 10-nm GaAs wells and 50-nm $\text{Al}_{0.5}\text{Ga}_{0.5}\text{As}$ barriers repeated five times. (b) Simulated (002) rocking curve of the same MQW structure. A comparison of (a) and (b) illustrates the value of the (002) reflection for enhancing the satellite structure. For both curves the origin of the angle scale is taken at the Bragg angle of GaAs, $\phi_B(004) = 33^\circ$ and $\phi_B(002) = 16^\circ$.

Unfortunately, the small size of F_{002} for GaAs also means that the reflected (002) intensity from this material is weak, as shown in Table 1-1, which makes it unsuitable as the reference crystal for the (002) reflection with a double-crystal diffractometer. Because of this problem, AlGaAs/GaAs SL and MQW structures were first analyzed using the (002) reflection with single-crystal diffractometers. More recently, the four-crystal diffractometer, providing a source of x-rays that is well defined in both wavelength and direction, has provided much more suitable instrumentation for high-resolution studies [14]. However, such instruments are relatively expensive and not readily available. Double-crystal diffractometers, on the other hand, have become standard characterization tools serving many epitaxial-growth facilities. Consequently, finding a suitable first crystal, lattice matched to GaAs, for (002) rocking curves would be of considerable value.

In this search we have investigated the use of epitaxial AlAs and GaInP. With the assumption of good crystal quality, the reflected intensity depends on the ratio of the elastic to inelastic scattering. The strength of the elastic scattering, proportional to the structure factor, is represented by the inverse of a thickness called the extinction depth. The inelastic scattering is proportional to the mass absorption coefficient, or inverse absorption depth [14]. Several calculated reflectivities for bulk material and layers 3 μm thick are given in Table 1-1. The reasonably high reflectivity for the thin layers provides the motivation for evaluating epitaxial materials.

TABLE 1-1
Reflectivities for Epitaxial Materials

Material	Reflection	Reflectivity	
		Bulk Material	3- μm Layer
GaAs	(004)	0.87	—
GaAs	(002)	0.08	—
AlAs	(002)	0.88	0.77
GaInP	(002)	0.81	0.76

In an initial attempt to find a first crystal, 4 μm of AlAs was grown on a GaAs substrate by OMVPE. A layer of GaAs, 50 nm thick, was grown on top in an attempt to prevent oxidation of the AlAs. The necessary long-term stability was not achieved, and efforts were then turned to evaluating epitaxial GaInP. The morphology of GaInP grown by atmospheric pressure OMVPE depends on factors such as substrate orientation and layer thickness. Mirror-smooth morphology, assessed by Nomarski-contrast optical microscopy, is obtained for growth on substrates oriented 5° off (001) toward [110] for layers up to ~ 1.5 μm thick. These typically give x-ray linewidths of 20 to 25 arc sec (FWHM). For this study, a layer 3 μm thick was grown on this orientation. Some surface roughening occurred due to the thickness, and the linewidth for the (004) reflection increased to 30 arc sec. Two pieces of this material were used to obtain a (002) rocking curve with the satisfactory first results of 43-arc sec linewidth and 2.2×10^4 -counts/s peak intensity.

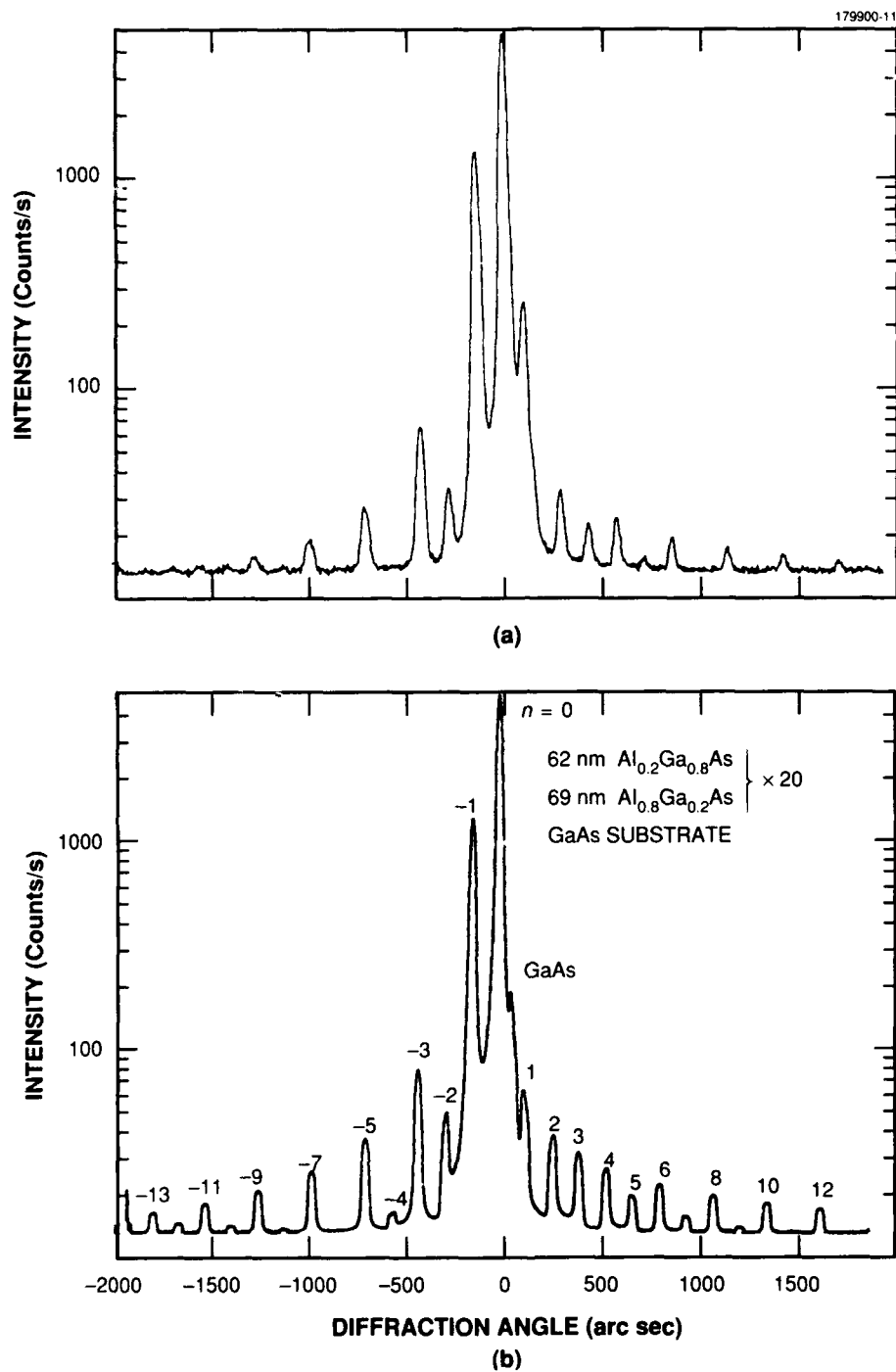


Figure 1-15. (a) Experimental (002) rocking curve of a 20-period AlGaAs interference-stack sample. (b) Simulated rocking curve with best-fit parameters, in which the peaks due to the substrate and the various satellite orders are labeled. Some sample curvature has been introduced to broaden the simulated peaks.

Figure 1-15(a) shows a (002) rocking curve run with this material as a first crystal and a sample with a repetitive stack of two AlGaAs alloys as the second crystal. The curve was recorded with steps of 4 arc sec and a count time of 180 s. Satellite peaks of orders -14 to 12 are seen. The (004)-reflection rocking curve of this sample, with GaAs as the first crystal, shows only peaks of orders -4 to 8. A best-fit simulated curve for the (002) reflection is shown in Figure 1-15(b). (A (002) rocking curve on this sample was run on a four-crystal diffractometer by Dr. T. Ryan of Philips Analytical. For a comparable scan time, satellite peaks of orders -22 to 25 were detected.)

In conclusion, we have demonstrated that epitaxial GaInP can fill the need for a first crystal for (002) rocking curves on materials lattice matched to GaAs. A layered AlGaAs sample has been run with (004) and (002) Bragg reflections, and the latter gives about double the number of satellite peaks. Further improvements in crystal quality and instrumentation are expected in this effort to obtain (002) double-crystal rocking curves on GaAs-based structures. On the other hand, the double-crystal diffractometer, which has high angular resolution but is nondispersive, is unlikely to produce results that are fully comparable to those of the four-crystal diffractometer, where the x-ray wavelength is also well defined. The virtue of the approach demonstrated here is that it makes use of a commonly available instrument, and it produces results that are sufficiently detailed for many structural determinations.

S. H. Groves

D. R. Calawa

S. C. Palmateer

C. A. Wang

REFERENCES

1. A. Sonnenschein and W. K. Hutchinson, MIT Lincoln Laboratory Technical Report 887, August 1990.
2. J. P. Donnelly, K. Rauschenbach, C. A. Wang, W. D. Goodhue, and R. J. Bailey, *Proc. SPIE* **1043**, 92 (1989).
3. W. D. Goodhue, K. Rauschenbach, C. A. Wang, J. P. Donnelly, and G. D. Johnson, *J. Electron. Mater.* **19**, 463 (1990).
4. C. A. Wang, H. K. Choi, and M. K. Connors, *IEEE Photon. Technol. Lett.* **1**, 351 (1989).
5. J. P. Donnelly, K. Rauschenbach, C. A. Wang, R. J. Bailey, J. N. Walpole, L. J. Missaggia, J. D. Woodhouse, H. K. Choi, F. J. O'Donnell, and V. Diadiuk, *Proc. SPIE* **1219**, 255 (1990).
6. A. J. SpringThorpe, *Appl. Phys. Lett.* **31**, 524 (1977).
7. N. Hamao, M. Sugimoto, N. Takado, Y. Tashiro, H. Iwata, T. Yuasa, and K. Asakawa, *Appl. Phys. Lett.* **54**, 2389 (1989).
8. T. Takamori, L. A. Coldren, and J. L. Merz, *Appl. Phys. Lett.* **55**, 1053 (1989).
9. W. D. Goodhue, G. D. Johnson, and T. H. Windhorn, in *Gallium Arsenide and Related Compounds 1986*, W. T. Lindley, ed. (IOP Publishing, Bristol, England, 1987), p. 349.

10. H. K. Choi and C. A. Wang, *Appl. Phys. Lett.* **57**, 321 (1990).
11. C. A. Wang, J. N. Walpole, L. J. Missaggia, J. P. Donnelly, and H. K. Choi, to be published in *Appl. Phys. Lett.*
12. S. C. Palmateer, S. H. Groves, J. W. Caunt, and D. L. Hovey, *J. Electron. Mater.* **18**, 645 (1989).
13. B. R. Pruniaux, J. C. North, and G. L. Miller, in *Ion Implantation in Semiconductors*, I. Ruge and J. Graul, eds. (Springer-Verlag, Berlin, 1971), p. 212.
14. W. J. Bartels, *J. Vac. Sci. Technol. B* **1**, 338 (1983).

2. QUANTUM ELECTRONICS

2.1 THERMAL LOADING IN Nd:YAG AND Yb:YAG

Thermal loading in solid state laser materials limits the performance of the lasers. Thermal gradients cause effects such as thermooptic distortion, stress-induced birefringence, and, at the highest power levels, stress fracture and melting. Gain media with low thermal loading offer the potential for higher average power scaling because of the reduced thermal effects. We have measured the fraction of absorbed optical power from diode lasers that is converted to heat, η_h , in Nd:YAG and Yb:YAG and show that Yb:YAG has lower fractional thermal loading, as expected.

Heating in Nd:YAG and Yb:YAG is expected to be primarily due to the quantum defect, i.e., the difference between the pump photon energy and the fluorescence or laser output photon energy. In Nd:YAG the average fluorescence wavelength from the upper laser level is 1.038 μm ; in Yb:YAG the average fluorescence wavelength is 1.008 μm . Thus, for 808-nm diode-laser pumping of Nd:YAG, η_h should be 0.22 in the absence of stimulated emission, if the radiative quantum efficiency η_r of the Nd:YAG is 1. For 943-nm pumping of Yb:YAG, η_h should be 0.064 if $\eta_r = 1$. For CW laser operation far above threshold, η_h is given by the difference between the pump and laser photon energies divided by the pump photon energy if every excited ion contributes to laser oscillation.

We measure η_h using a calorimetric technique. The material under test is suspended in air by a thermocouple. A low-intensity pump beam is incident on the sample, and the absorbed power is measured. The temperature of the sample is allowed to come to steady state before the laser is turned off, and the temperature is measured as a function of time. The fractional thermal loading is calculated from the steady-state temperature rise ΔT , the time constant τ for the temperature to return to ambient, and the absorbed power P_{abs} as

$$\eta_h = \frac{c_p m \Delta T}{\tau P_{\text{abs}}} , \quad (2.1)$$

where c_p is the heat capacity and m is the mass of the sample. The measured fractional thermal loading of five samples of Nd:YAG with various doping levels is shown in Figure 2-1. The expected thermal loading shown is calculated from the quantum defect and the known concentration quenching in Nd:YAG [1]. As expected, higher-doped Nd:YAG in general has higher thermal loading because of concentration quenching effects that lower the radiative quantum efficiency. For a sample of YAG doped with 6.5 at.% Yb, the measured η_h is 0.11. This number represents an upper bound because no correction has been made for additional thermal loading by radiative trapping, i.e., fluorescent photons that are reabsorbed, which can be significant in Yb:YAG.

The fractional thermal loading can be used to calculate the radiative quantum efficiency η_r of these materials. If we assume that the excitation of nonradiating ions is converted entirely to heat, the radiative quantum efficiency is given by

$$\eta_r = \frac{1 - \eta_h}{1 - \eta_{\text{QD}}} , \quad (2.2)$$

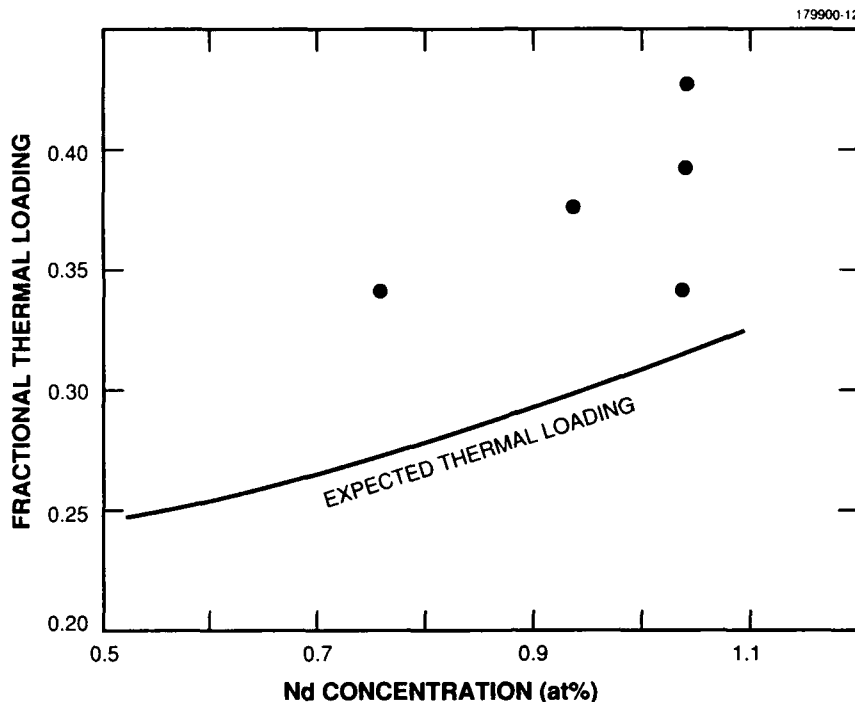


Figure 2-1. Fractional thermal loading for five samples of Nd:YAG pumped at 808 nm with low pump intensity. The curve shows the expected thermal loading due to the quantum defect and concentration quenching.

where η_{QD} is the thermal loading that would occur if the heating were due only to the quantum defect. The Yb:YAG has $\eta_r > 0.96$, while the 1.1%-doped Nd:YAG samples have η_r in the range from 0.73 to 0.84. In the absence of excited-state absorption and upconversion effects, high η_r means that the quantum slope efficiency of a laser will also be high. Thus, Yb:YAG lasers are expected to have good slope efficiency. Low η_r does not necessarily imply low quantum slope efficiency in laser operation; the slope efficiency is dependent on the mechanism responsible for low η_r .

To investigate the effect of nonunity η_r on Nd:YAG laser operation, we performed calorimetry measurements on one of the 1.1%-doped Nd:YAG samples (with $\eta_h = 0.43$) during CW laser operation. This sample was antireflection coated for 1.06- μm radiation and inserted into a cavity with round-trip intracavity loss of $\sim 2\%$. The measured thermal loading is shown in Figure 2-2 as a function of the ratio of pump power to threshold power. If all the dopant ions participate in laser oscillation, η_h should approach $\eta_{QD} = 0.24$ well above threshold. We have projected that the asymptotic limit well above threshold is 0.36, which indicates that some ions are acting as so-called dead sites, i.e., ions that are excited but do not contribute to laser oscillation. Dead sites in Nd:YAG have been previously postulated in order to explain experiments in which the pump wavelength was near 590 nm [2]. Based on our analysis, the fraction of dead sites is about 0.15. The effect of dead sites is to decrease laser efficiency and increase thermal loading.

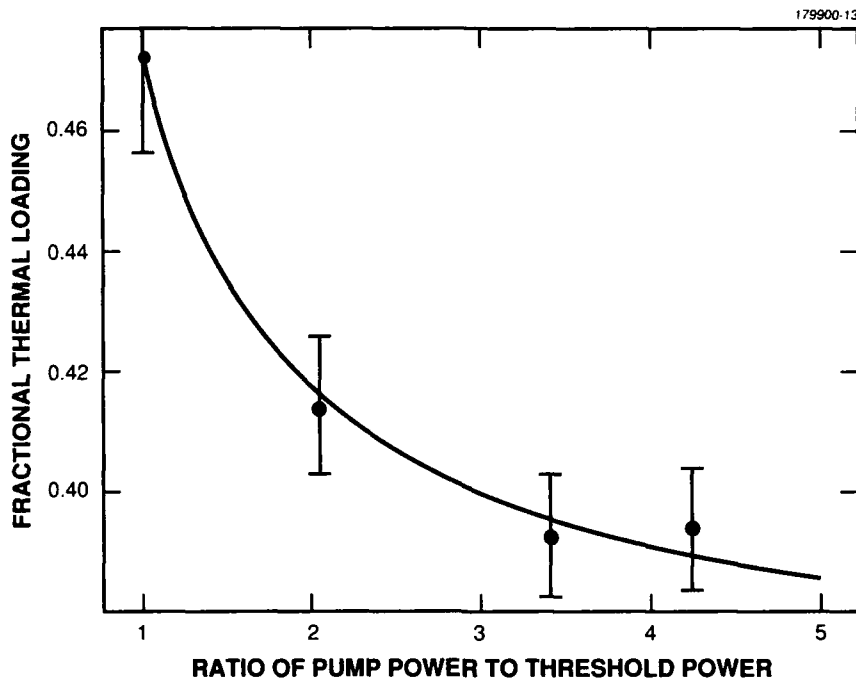


Figure 2-2. Fractional thermal loading of Nd:YAG during CW laser operation. The higher fractional thermal loading at threshold compared with that in Figure 2-1 is due to effects that occur with high pump intensity. The solid line is a model fitted to the data that projects $\eta_r = 0.36$ for laser operation very far above threshold. The vertical bars represent errors that occur from measurement to measurement and do not include systematic errors such as imperfect power meter calibration and uncertainty in the heat capacity.

In summary, we have measured the fractional thermal loading in Nd:YAG and Yb:YAG with optical pumping and found it to be at least a factor of 3 lower in Yb:YAG. Measurements of thermal loading during laser oscillation have produced evidence of dead sites in Nd:YAG, which decrease laser efficiency.

T. Y. Fan

REFERENCES

1. A. A. Kaminskii, *Laser Crystals: Physics and Properties* (Springer-Verlag, Berlin, 1981), p. 364.
2. D. P. Devor and L. G. DeShazer, *Opt. Commun.* **46**, 97 (1983).

3. MATERIALS RESEARCH

3.1 HIGH-POWER AlInGaAs/AlGaAs STRAINED SINGLE-QUANTUM-WELL DIODE LASERS

Recently we reported [1],[2] AlInGaAs/AlGaAs strained quantum-well lasers, with emission wavelengths ranging from 785 to 890 nm, that had threshold current densities as low as 103 A/cm² and differential quantum efficiencies as high as 90% for cavity lengths of 1500 and 300 μ m, respectively. Because the density of states is reduced by compressive strain, these lasers have lower threshold current densities than AlGaAs/AlGaAs lasers [2]. In addition, the incorporation of In in the active layer is expected to improve the reliability of the AlInGaAs/AlGaAs lasers, since the propagation of defects should be retarded because the In atom is larger than the Ga, Al, and As atoms, which are almost the same size [3]. This mechanism is believed to account for the improved reliability reported for InGaAs/AlGaAs strained quantum-well lasers [4],[5]. In this paper, we report CW operation of AlInGaAs/AlGaAs graded-index separate-confinement heterostructure single-quantum-well (GRINSCH-SQW) lasers with output power as high as 4.9 W/facet. Promising results have been obtained in preliminary lifetests of devices with uncoated facets at power levels of 1 and 2 W/facet.

The laser structure was grown on a GaAs substrate by organometallic vapor phase epitaxy in a rotating-disk reactor at low pressure. The structure consists of the following layers: 20-nm-thick *n*-GaAs buffer, 0.1- μ m-thick *n*-Al_yGa_{1-y}As (*y* linearly graded from 0.1 to 0.7 to reduce diode series resistance), 1.1- μ m-thick *n*-Al_{0.7}Ga_{0.3}As cladding, 0.15- μ m-thick undoped Al_yGa_{1-y}As confining (*y* linearly graded from 0.7 to 0.3), 10-nm-thick undoped Al_{0.09}In_{0.13}Ga_{0.78}As active, 0.15- μ m-thick undoped Al_yGa_{1-y}As confining (*y* linearly graded from 0.3 to 0.7), 1.1- μ m-thick *p*-Al_{0.7}Ga_{0.3}As cladding, 0.1- μ m-thick *p*-Al_yGa_{1-y}As (*y* linearly graded from 0.7 to 0.1), and 0.1- μ m-thick *p*⁺-GaAs contact. The *n*- and *p*-type doping levels in the cladding layers were varied from 10¹⁸ to 10¹⁷ cm⁻³ toward the GRIN layers to reduce the optical loss resulting from free-carrier absorption. Detailed growth conditions have been reported previously [1].

Broad-stripe lasers were fabricated by the following procedure. Mesas 500 μ m wide were formed by etching the *p*⁺-GaAs and *p*-AlGaAs layers to a depth of \sim 0.2 μ m. The entire front surface was metallized with Ti/Pt/Au to form ohmic contact to the *p*⁺-GaAs and Schottky contact to the *p*-AlGaAs. The wafer was thinned from the substrate side to \sim 100 μ m, and contact to the *n*-GaAs was made by alloying Ge/Au/Ni/Ti/Au at 390°C. The wafer was cleaved into bars 1000 μ m long, which were then separated into individual chips by scribing. The laser facets were not coated.

Several lasers were mounted junction side down on copper heatsinks with In solder. The emission wavelength measured under pulsed operation at room temperature is 855 nm. The pulsed threshold current and differential quantum efficiency η_d for one device are plotted against temperature in Figures 3-1 and 3-2, respectively. The threshold current increases from 0.67 A at 25°C to 1.87 A at 155°C. The values of the characteristic temperature T_0 are 180, 123, and 92 K for heatsink temperature ranges of 25 to 65°C, 85 to 105°C, and 125 to 155°C, respectively. The value of η_d is almost constant at \sim 73% between 25 and 105°C, then decreases gradually with increasing temperature, but is higher than 60% even at 155°C.

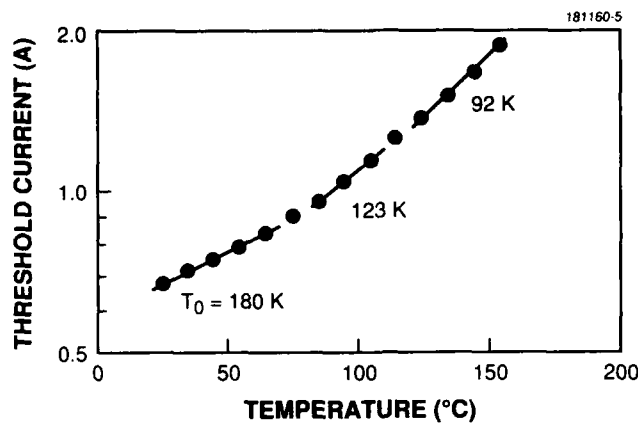


Figure 3-1. Pulsed threshold current vs temperature for a $500 \times 100\text{-}\mu\text{m}$ AlInGaAs/AlGaAs diode laser.

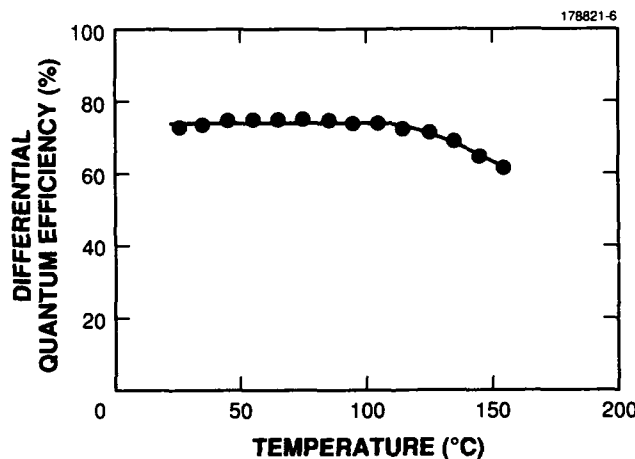


Figure 3-2. Pulsed differential quantum efficiency vs temperature for the diode laser of Figure 3-1.

Figure 3-3 shows the CW output power vs current for another device at a heatsink temperature of 10°C . The threshold current is 685 mA, and the initial η_d is 73%. The maximum power is 4.9 W/facet. At this level the device failed catastrophically. Because the beam size in the transverse direction is $\sim 0.23\text{ }\mu\text{m}$, the catastrophic damage threshold is $> 4\text{ MW/cm}^2$. The power conversion efficiency is as high as 49%. The series resistance is $0.05\text{ }\Omega$. From data on the power efficiency and the dependence of emission wavelength on heatsink temperature and output power, the thermal impedance is estimated to be $\sim 4^{\circ}\text{C/W}$.

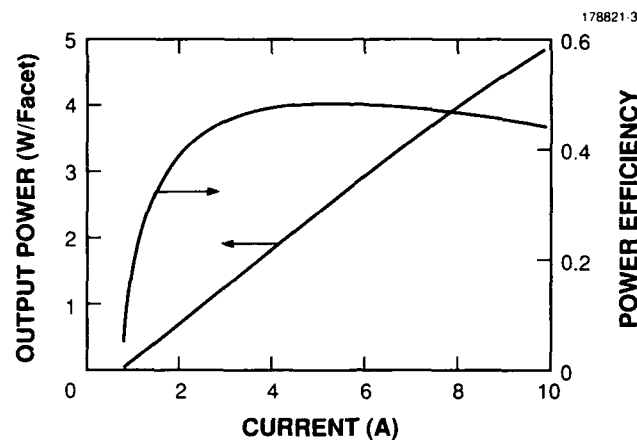


Figure 3-3. CW output power and power efficiency vs current for a $500 \times 1000\text{-}\mu\text{m}$ AlInGaAs/AlGaAs diode laser at a heatsink temperature of 10°C .

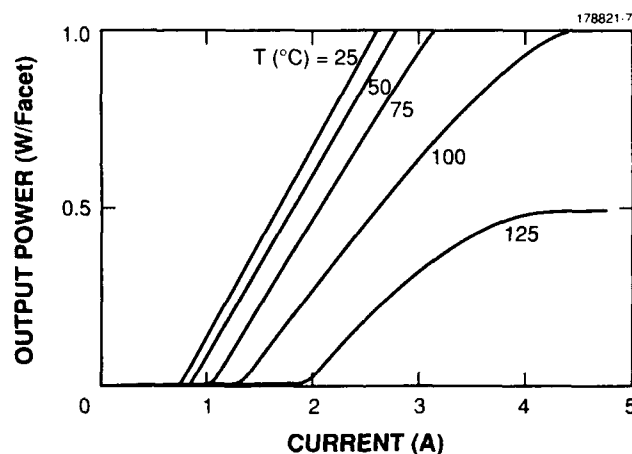


Figure 3-4. CW output power vs current for a $500 \times 1000\text{-}\mu\text{m}$ AlInGaAs/AlGaAs diode laser at heatsink temperatures between 25 and 125°C .

Figure 3-4 shows the curves of CW output power vs current for another device at heatsink temperatures between 25 and 125°C . With increasing heatsink temperature the value of η_d decreases more rapidly than in the case of pulsed operation because T_0 decreases with temperature. The maximum powers obtained at heatsink temperatures of 100 and 125°C are 1 and 0.5 W/facet, respectively.

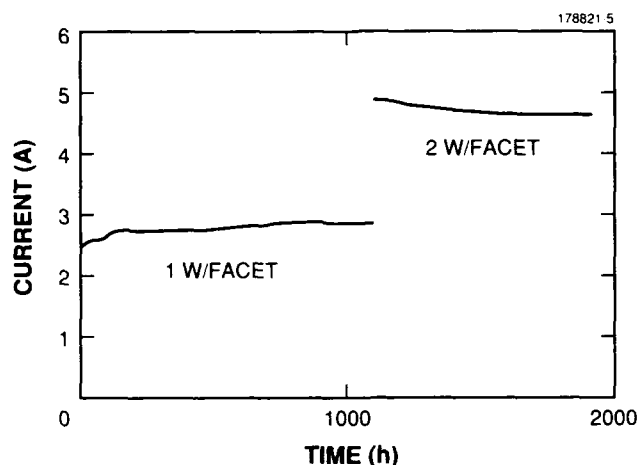


Figure 3-5. Lifetest of a $500 \times 1000\text{-}\mu\text{m}$ AlInGaAs/AlGaAs diode laser at a heatsink temperature of 10°C , for output power levels of 1 W/facet for 1100 h and then 2 W/facet for 800 h.

One device was lifetested at a heatsink temperature of 10°C , first at an output power of 1 W/facet for 1100 h and subsequently at 2 W/facet for 800 h. There was no initial burn-in before the test. Figure 3-5 shows the time dependence of the current required to maintain constant power. This current initially increased rapidly, from 2.46 to 2.76 A in ~ 150 h, increased much more slowly to 2.88 A in the next 600 h, and then remained essentially constant for 350 h. The power was then increased to 2 W/facet. The current to maintain this power level decreased from 4.92 to 4.62 A in 800 h. Subsequently, the power was intentionally increased by gradually increasing the current. At ~ 2.5 W/facet the output power suddenly decreased, probably because of facet degradation. Oxidation during the lifetest may have lowered the facet damage threshold.

In an initial experiment to investigate the effect of temperature on reliability, two other devices were lifetested for 300 h at 1 W/facet, but at a heatsink temperature of 50°C . In the first 100 h, the current values exhibited the same relative change as in 750 h at 10°C heatsink temperature. For the next 200 h, however, there was no further change in current. These results suggest that even without facet coating AlInGaAs/AlGaAs lasers will be very reliable.

H. K. Choi	R. L. Aggarwal
C. A. Wang	J. N. Walpole
D. F. Kolesar	

3.2 ROOM-TEMPERATURE CW OPERATION OF GaInAsSb/AlGaAsSb DIODE LASERS EMITTING AT $2.2\text{ }\mu\text{m}$

Double-heterostructure diode lasers incorporating a GaInAsSb active layer and AlGaAsSb confining layers lattice matched to a GaSb substrate are being developed to provide emission in the 2- to $5\text{-}\mu\text{m}$ spectral range. Room-temperature CW operation of index-guided GaInAsSb/AlGaAsSb lasers

grown by liquid phase epitaxy (LPE) has been achieved by two groups [6],[7]. We have recently reported [8] the room-temperature pulsed operation of broad-stripe double-heterostructure $\text{Ga}_{0.84}\text{In}_{0.16}\text{As}_{0.14}\text{Sb}_{0.86}/\text{Al}_{0.5}\text{Ga}_{0.5}\text{As}_{0.04}\text{Sb}_{0.96}$ lasers grown by molecular beam epitaxy (MBE), which had threshold current density J_{th} as low as 1.5 kA/cm^2 for a cavity length L of $700 \mu\text{m}$. These devices exhibited values of η_d as high as 50% and pulsed output power as high as 900 mW/facet , the highest room-temperature values for any semiconductor laser emitting beyond $2 \mu\text{m}$. In this paper, we report the CW operation at temperatures up to 30°C of gain-guided double-heterostructure $\text{Ga}_{0.84}\text{In}_{0.16}\text{As}_{0.14}\text{Sb}_{0.86}/\text{Al}_{0.75}\text{Ga}_{0.25}\text{As}_{0.06}\text{Sb}_{0.94}$ lasers with emission wavelength of $\sim 2.2 \mu\text{m}$. The pulsed value of J_{th} has been reduced to as low as 0.94 kA/cm^2 for $L = 1000 \mu\text{m}$, the lowest room-temperature value for any semiconductor laser emitting beyond $2 \mu\text{m}$.

The GaInAsSb and AlGaAsSb layers were grown by MBE in the manner described previously [9],[10]. The laser structure consists of the following layers: $0.8\text{-}\mu\text{m}$ -thick $n\text{-GaSb}$ buffer, $2\text{-}\mu\text{m}$ -thick $n\text{-Al}_{0.75}\text{Ga}_{0.25}\text{As}_{0.06}\text{Sb}_{0.94}$ cladding, $0.4\text{-}\mu\text{m}$ -thick nominally undoped $n\text{-Ga}_{0.84}\text{In}_{0.16}\text{As}_{0.14}\text{Sb}_{0.86}$ active, $2\text{-}\mu\text{m}$ -thick $p\text{-Al}_{0.75}\text{Ga}_{0.25}\text{As}_{0.06}\text{Sb}_{0.94}$ cladding, and $0.05\text{-}\mu\text{m}$ -thick $p^+\text{-GaSb}$ cap.

The surface of the laser structure is very smooth, with no visible cross-hatching, because all the layers are closely lattice matched. Cladding layers of $\text{Al}_{0.75}\text{Ga}_{0.25}\text{As}_{0.06}\text{Sb}_{0.94}$ have not been used before in diode lasers because LPE growth of lattice-matched AlGaAsSb alloys with Al content higher than 40% is very difficult [11].

Broad-stripe lasers $300 \mu\text{m}$ wide were fabricated by a lift-off process similar to the one reported previously [9]. To obtain low threshold currents, narrow-stripe lasers $30 \mu\text{m}$ wide were fabricated by the following process. Mesas were formed by etching the $p^+\text{-GaSb}$ and $p\text{-AlGaAsSb}$ layers to a depth of $\sim 0.2 \mu\text{m}$ using a photoresist mask. The entire surface was metallized with Ti/Au to form ohmic contact to the $p^+\text{-GaSb}$ and Schottky contact to the $p\text{-AlGaAsSb}$. Ohmic contact to the $n\text{-GaSb}$ was formed by depositing Au/Si/Ni/Ti/Au and alloying at 300°C .

The lasers were probe tested in the pulsed mode at room temperature. For the broad-stripe lasers the emission spectrum exhibits multiple longitudinal modes centered at $2.19 \mu\text{m}$. The emission spectrum of narrow-stripe lasers peaks at $2.17 \mu\text{m}$ as a result of greater band filling, which occurs because J_{th} increases with decreasing stripe width. The far-field pattern in the direction perpendicular to the junction plane has a full width at half-maximum of 78° .

Figure 3-6 shows the dependence of J_{th} on L for broad-stripe lasers. As L increases from 300 to $1000 \mu\text{m}$, J_{th} decreases monotonically from 1.3 to 0.94 kA/cm^2 . For comparison, the data previously reported [9] for lasers with $\text{Al}_{0.5}\text{Ga}_{0.5}\text{As}_{0.04}\text{Sb}_{0.96}$ cladding layers are also shown. For the same L , J_{th} is about 30% lower for the devices with higher Al content. The reduction in J_{th} was achieved not only by tighter optical confinement but also by the improvement in the lattice matching of the cladding layers.

For CW operation, narrow-stripe lasers $300 \mu\text{m}$ long were mounted junction side down on copper heatsinks with In solder. The series resistance in the forward direction is 12Ω . Figure 3-7 shows the CW output power vs current (P-I) for a device measured at several heatsink temperatures. A pyroelectric detector with a mechanical chopper measured the power. Output powers as high as 10.5 and 4.6 mW/facet were obtained

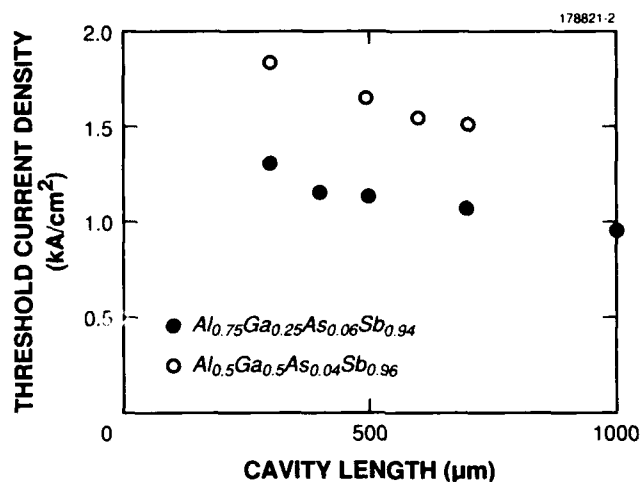


Figure 3-6. Dependence of threshold current density on cavity length for broad-stripe GaInAsSb/AlGaAsSb lasers with a $Ga_{0.84}In_{0.16}As_{0.14}Sb_{0.86}$ active layer and two different cladding layer compositions.

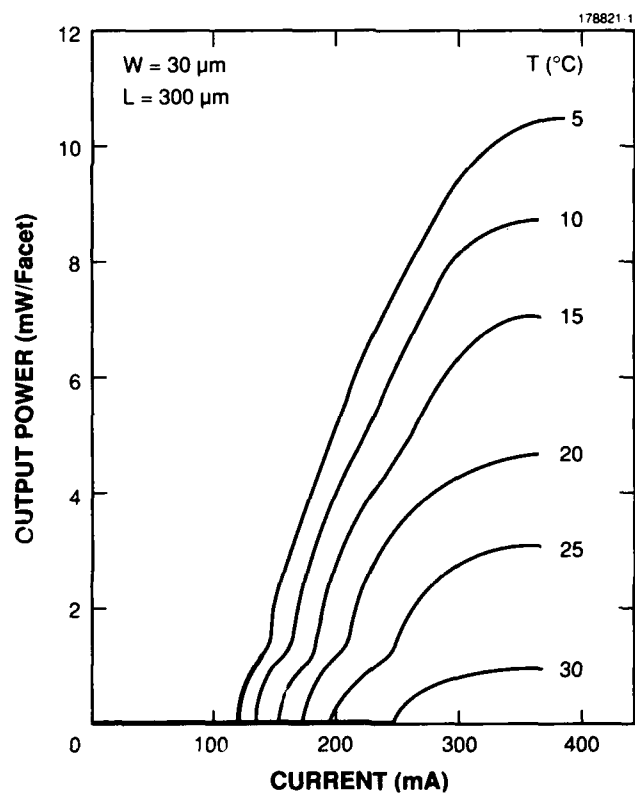


Figure 3-7. CW output power vs current for a GaInAsSb/AlGaAsSb laser 30 μm wide by 300 μm long at several heatsink temperatures.

at heatsink temperatures of 5 and 20°C, respectively. CW operation is observed up to 30°C, where the maximum power is 0.9 mW/facet. The only previously reported CW power level for GaInAsSb/AlGaAsSb lasers is ~ 1 mW, which was obtained at room temperature for devices grown by LPE [6]. The kinks in the P-I curves result from the instability of the near-field pattern, a characteristic commonly observed for gain-guided GaAs/AlGaAs lasers [12]. Observations with a PbS camera showed the near-field pattern to have three or four filaments whose relative intensities change with the current level.

Figure 3-8 shows the threshold current of the same device as a function of heatsink temperature for both pulsed and CW operation. The CW threshold current increases from 117 mA at 5°C to 257 mA at 30°C. These values are 12 and 77 mA higher than the respective pulsed values because the junction temperatures are higher under CW operation. The value of T_0 for pulsed operation is 49 K between 5 and 35°C, and 44 K between 35 and 55°C. These values are comparable to those reported previously [9],[13]. For CW operation, the T_0 values are much smaller than the respective pulsed values because the difference between the junction and heatsink temperatures increases with the heatsink temperature. At a heatsink temperature of 25°C, the CW value of T_0 is only 25 K.

H. K. Choi
S. J. Eglash

W. L. McGilvary
J. V. Pantano

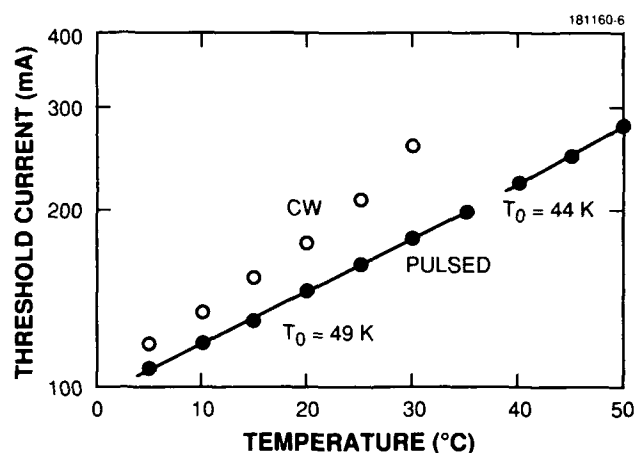


Figure 3-8. Dependence of threshold current on temperature for pulsed and CW operation of the diode laser of Figure 3-7.

REFERENCES

1. C. A. Wang, J. N. Walpole, H. K. Choi, and L. J. Missaggia, *IEEE Photon. Technol. Lett.* **3**, 4 (1991).
2. C. A. Wang, J. N. Walpole, L. J. Missaggia, J. P. Donnelly, and H. K. Choi, *Appl. Phys. Lett.* **58**, 2208 (1991).

3. J. Matsui, in *Defects in Semiconductors II* (Materials Research Society, Pittsburgh, 1990), p. 477.
4. S. E. Fischer, R. G. Waters, D. Fekete, J. M. Ballantyne, Y. C. Chen, and B. A. Soltz, *Appl. Phys. Lett.* **54**, 1861 (1989).
5. D. P. Bour, D. B. Gilbert, K. B. Fabian, J. P. Bednarz, and M. Ettenberg, *IEEE Photon. Technol. Lett.* **2**, 173 (1990).
6. A. E. Bochkarev, L. M. Dolginov, A. E. Drakin, P. G. Eliseev, and B. N. Sverdlov, presented at 11th Int. Semiconductor Laser Conf., Boston, Mass., 28 August–1 September 1988, Paper PD-8.
7. A. N. Baranov, T. N. Danilova, B. E. Dzhurtanov, A. N. Imenkov, S. G. Konnikov, A. M. Litvak, V. E. Usmanskii, and Yu. P. Yakovlev, *Sov. Tech. Phys. Lett.* **14**, 727 (1988).
8. H. K. Choi and S. J. Eglash, presented at 12th IEEE Int. Semiconductor Laser Conf., Davos, Switzerland, 9-13 September 1990, Paper PD-9.
9. S. J. Eglash and H. K. Choi, *Appl. Phys. Lett.* **57**, 1292 (1990).
10. S. J. Eglash, H. K. Choi, and G. W. Turner, to be published in *J. Cryst. Growth*.
11. G. Motosugi and T. Kagawa, *J. Cryst. Growth* **49**, 102 (1980).
12. T. L. Paoli, *IEEE J. Quantum Electron.* **QE-11**, 770 (1976).
13. J. L. Zyskind, J. C. DeWinter, C. A. Burrus, J. C. Centanni, and M. A. Pollack, *Electron. Lett.* **25**, 568 (1989).

4. SUBMICROMETER TECHNOLOGY

4.1 EXCIMER-LASER-INDUCED SUB-0.5- μm PATTERNING OF WO_3 THIN FILMS

A new type of excimer-induced solid state transformation is reported, namely, structural changes in amorphous WO_3 . Unlike ablation or melting, for instance, the changes in WO_3 do not involve a phase transformation but rather atomic rearrangements within the amorphous phase. As shown below, these subtle modifications nevertheless have a significant impact on the macroscopic optical and chemical properties of the material. We have exploited these effects to use WO_3 as an all-dry inorganic photoresist at 193 nm and have demonstrated negative-tone patterning with submicrometer resolution. WO_3 has been studied extensively as an electrochromic material [1]-[3] and also as an ion-beam resist [4] and electron-beam resist [5]. In these resist applications the particle beam reduces the solubility in alkaline solutions by a process that has not been fully identified. In fact, the electron-beam-induced transformation [5] may be related to the photoinduced process described in this report.

In our studies, the deposition of WO_3 thin films is performed in a plasma-enhanced chemical vapor deposition (PECVD) system. A 13.56-MHz RF plasma is generated in a 1:4:1 mixture of WF_6 , O_2 , and H_2 at a total pressure of 40 mTorr and a dc self-bias voltage of -200 V. The substrates are held near room temperature. Deposition rates of ~ 10 nm/min are obtained on a variety of substrates, including Si(100), SiO_2 thermally grown on Si, fused silica, and a range of carbon-based thin films, such as PECVD hydrogenated amorphous carbon ($\alpha\text{-C:H}$), AZ photoresist, and poly(methyl methacrylate) (PMMA). The PECVD WO_3 films are amorphous and electrically resistive. Their optical properties are similar to those found by Deb [1]: the index of refraction at 632.8 nm is in the range from 1.85 to 2.2, and the absorption coefficient increases rapidly at wavelengths below ~ 340 nm. At 193 nm, the absorption length is ~ 50 nm. Monochromatic x-ray photoelectron spectroscopy (XPS) indicates that the stoichiometry of these films is $\text{WO}_{2.9}\text{F}_{0.2}$. The fluorine 1s XPS peak has a binding energy of 684.2 eV, which can be attributed to nonvolatile WF_4 [6] incorporated in the WO_3 matrix. Fourier-transform infrared spectroscopy shows that, unlike WO_3 films grown by other methods [3],[7], the PECVD WO_3 does not adsorb water, even after weeks of exposure to ambient air.

Following deposition, the WO_3 films are exposed to 193-nm radiation from an ArF excimer laser and are then etched in a low-power RF plasma of CF_4 . The laser-irradiated WO_3 has an etch rate up to ~ 5 times lower than that of the as-deposited WO_3 . Figure 4-1 illustrates this effect. At an RF power density of 16 mW/cm², the unirradiated film is etched at a rate of 1 nm/min, while a film exposed to one pulse of 25 mJ/cm² is etched at ~ 0.2 nm/min. The etch selectivity all but disappears at power densities above ~ 150 mW/cm². Apparently, the laser-induced changes in the WO_3 film are correlated with differential etching in a fluorine chemistry only as long as the etchant concentration is relatively low.

In order to elucidate the underlying cause of the difference in etch rates, we have performed XPS studies on WO_3 films that were partially etched in CF_4 . The spectra are taken with a monochromatized Al x-ray source at several takeoff angles. Some of the more prominent results are summarized in Figure 4-2, which shows the spectra of the fluorine 1s photoelectron in WO_3 films exposed to four different laser and plasma conditions. The fluorine in as-deposited WO_3 has a single binding energy of 684.2 eV, which

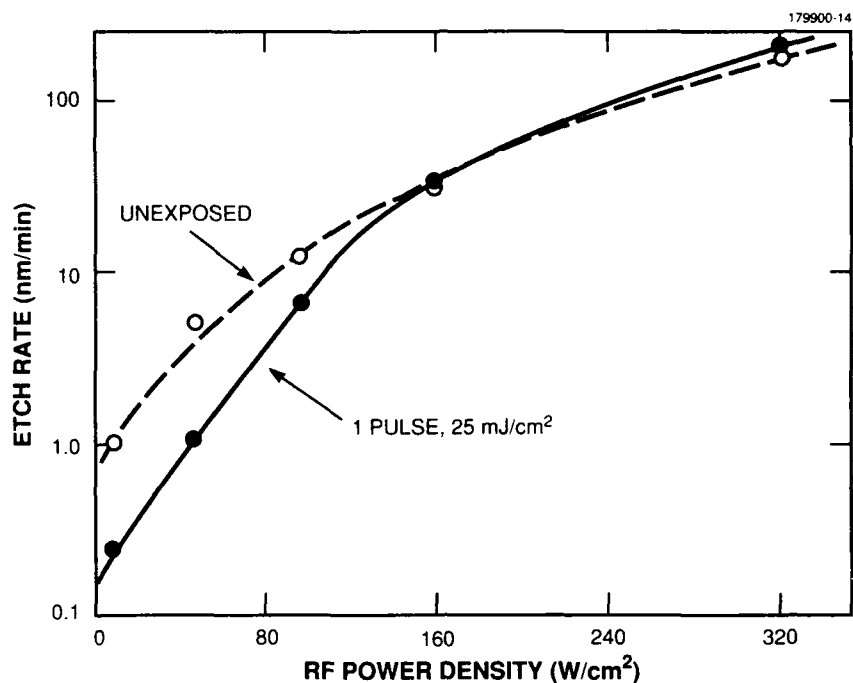


Figure 4-1. Semilog plot of the etch rate of a WO_3 film in a CF_4 parallel-plate plasma as a function of the RF power density. The film had been deposited on a Si(100) substrate to a thickness of 180 nm. The CF_4 etch pressure was 300 mTorr. At low power levels, one 25-mJ/cm² laser pulse causes a fivefold reduction in etch rate.

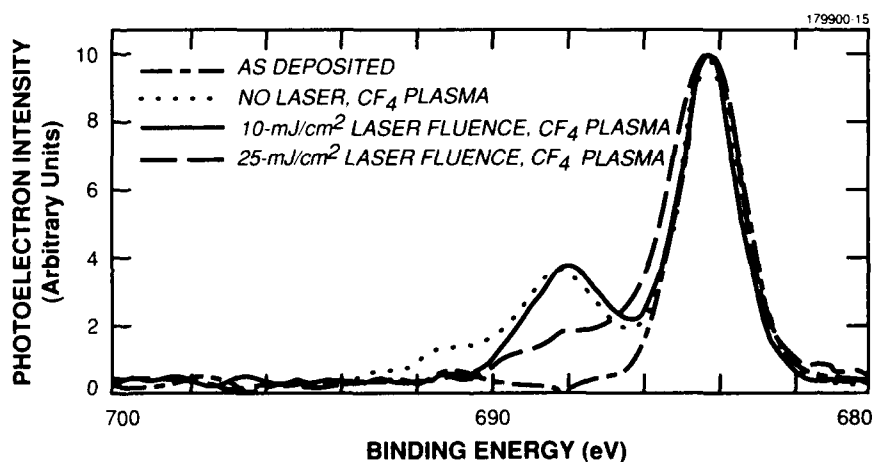


Figure 4-2. XPS spectra taken at 45° takeoff angle of the F 1s photoelectron of an as-deposited WO_3 film on Si(100) and of samples of the same film following three postdeposition treatments. The as-deposited film has only one peak, at 684.2 eV, and the films that have been partially etched in a CF_4 plasma have additional peaks whose intensity is modified by laser exposure prior to etching.

is attributed to WF_4 [6], as mentioned above. Its atomic concentration relative to that of tungsten is 0.2 which, assuming WF_4 bonding, implies that $\sim 5\%$ of the tungsten atoms are fluorinated and the rest are oxidized. Indeed, the oxygen-to-tungsten atomic ratio is 2.9, which translates into full oxidation (WO_3) of the 95% tungsten atoms that are not fluorinated. The $\text{F } 1s$ spectra of three WO_3 films following exposure to a 32-mW/cm^2 CF_4 plasma are also shown in Figure 4-2. The spectra of the film that had not been irradiated by the laser and the one that had been irradiated by one 10-mJ/cm^2 pulse are similar to each other and different from the spectra of the as-deposited film. The difference manifests itself in the appearance of a pronounced peak at a binding energy of 688.0 ± 0.2 eV. Analytical curve fitting clearly indicates the existence of a third, weaker peak at 686.2 ± 0.3 eV. These two binding energies are attributed to fluorine atoms in the form of WF_6 (686.2 eV) [6] and CF_x (688.0 eV) [8]. At the 45° takeoff angle used in Figure 4-2, the atomic ratio of fluorine to tungsten is ~ 0.34 (as compared to 0.20 for the as-deposited film). Of the F atoms in the film, $\sim 62\%$ are in the form of WF_4 , $\sim 5\%$ are as WF_6 , and $\sim 33\%$ are as CF_x . For the WO_3 irradiated with one 25-mJ/cm^2 pulse, the amount of CF_x is significantly reduced, as seen in Figure 4-2. Indeed, quantitative analysis shows that the F:W atomic ratio is ~ 0.26 , and $\sim 75\%$ of the F are as WF_4 , $\sim 12\%$ are as WF_6 , and $\sim 13\%$ are as CF_x . Furthermore, angle-dependent XPS indicates that in the 25-mJ/cm^2 WO_3 the CF_x and WF_6 components fall off rapidly with depth below the surface, while in the WO_3 that has not been irradiated or has been irradiated with one 10-mJ/cm^2 pulse, the non- WF_4 components decay much more gradually with increasing depth.

The conclusions that can be drawn from the XPS results are (1) that increased etch rates of WO_3 in CF_4 plasma are correlated with increased amounts of CF_x and WF_6 at and below the surface being etched, and (2) that excimer laser irradiation prior to etching reduces both the formation at the surface of CF_x and the range of penetration below the surface of CF_x and WF_6 . The CF_x species at the surface are probably nonvolatile products of the plasma, and their density is apparently related to that of the etchant radicals. The presence of WF_6 at and below the surface is somewhat surprising, since WF_6 is thought to be a volatile product of the etch process. The small amounts of WF_6 that were detected in our studies are probably molecules trapped in the reaction layer. Similar surface-bound WF_6 and SiF_4 have been reported in the plasma etching of W [9] and Si [10], respectively.

Our results can be understood with reference to the structure of amorphous WO_3 , which is thought to comprise WO_6 octahedra arranged in randomly packed clusters [11],[12]. The clusters enclose pores whose size and distribution are expected to be strongly dependent on the deposition conditions and on postdeposition treatments. As deposited, our films apparently have large enough voids to accommodate small, fluorine-containing radicals generated in the CF_4 plasma, even to a depth of several nanometers. Etching by these radicals can therefore proceed at a fast rate. Pulsed laser irradiation at 15 to 30 mJ/cm^2 per pulse disrupts the initial packing and enables rearrangement into denser clusters with smaller voids. The surface area open to chemical attack by the etchants is reduced, and so is their penetration depth, i.e., the thickness of the reaction layer. The XPS data and the etch rate values are consistent with this model.

The thresholdlike dependence on fluence of the laser-induced effects indicates that the material transformation has a large thermal component. Indeed, heating WO_3 films in an oven in the range from 200 to 300°C leads to similar changes in etch rate. Above 300°C , a transformation from amorphous to

polycrystalline takes place, as determined by x-ray diffraction. The main difference between the laser-exposed and the oven-heated WO_3 films lies in their morphology: the former are smooth and uniform, whereas the latter exhibit cracks and pits indicative of large thermal stresses. Preliminary results of modeling the thermal behavior during and after an excimer laser pulse do not seem to corroborate a purely thermal model. For 150 nm of WO_3 on Si, a 25-mJ/cm² pulse raises the surface temperature to $\sim 120^\circ\text{C}$ for only a few nanoseconds. At the WO_3/Si interface the maximum temperature rise is only $\sim 55^\circ\text{C}$. These temperature excursions are insufficient in oven-heating experiments to change the CF_4 etch rate. Further modeling and experiments are required to determine the extent of nonthermal effects operative in the excimer-induced process.

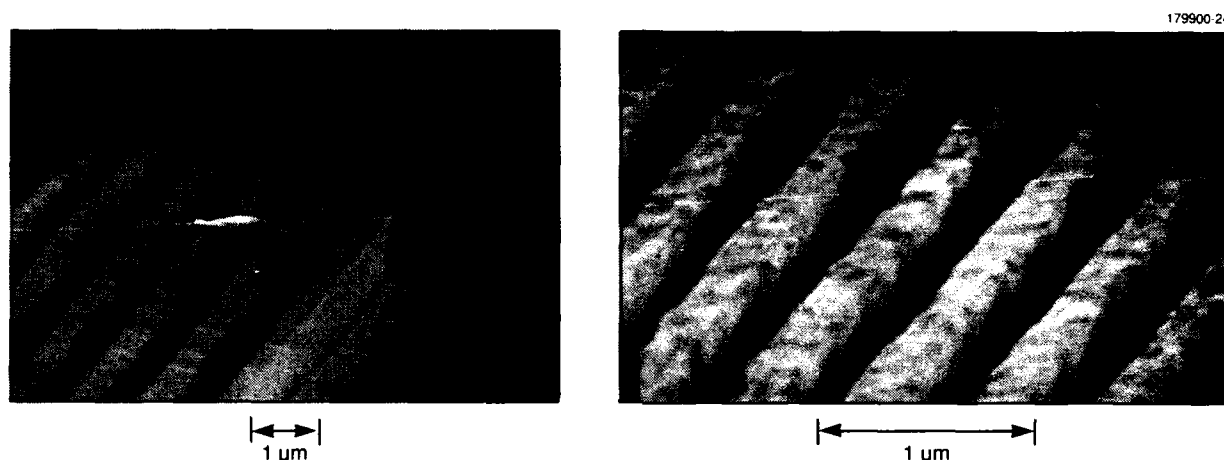


Figure 4-3. Scanning electron micrographs of nominally (a) 0.5- μm and (b) 0.35- μm lines and spaces patterned in an all-dry bilayer. First, a 1- μm -thick a-C:H layer was deposited by PECVD, and then a 75-nm-thick WO_3 imaging layer was deposited, also by PECVD. Next, exposure was performed in projection with a 193-nm excimer laser in one 20-mJ/cm² pulse, followed by dry development in a low-power CF_4 plasma and pattern transfer through the a-C:H layer in an O_2 reactive ion etching plasma.

The etch selectivity suggests the use of WO_3 as a dry-deposited, dry-developed, negative-tone inorganic photoresist at 193 nm. Figure 4-3 demonstrates the sub-0.5- μm resolution attained when 75 nm of WO_3 was deposited on a 1- μm -thick carbon-based film in a lithographic bilayer configuration. Patterned laser exposure was performed in projection with a 0.5-numerical-aperture (NA) Schwarzschild objective, with one 20-mJ/cm² pulse. The development was carried out in a CF_4 plasma for 15 min, followed by O_2 reactive ion etching for pattern transfer. We note that the high etch selectivity in CF_4 plasma between exposed and unexposed areas, combined with the excellent resistance of WO_3 to O_2 plasma, enables the use of this inorganic photoresist at thicknesses that are an order of magnitude smaller than those of more conventional, polymer-based photoresists. The reduced thickness makes possible the use of high-resolution, high-NA imaging systems, which have small depths of focus.

In conclusion, we have demonstrated the applicability of WO_3 as a dry-deposited, dry-developed photoresist at 193 nm. Submicrometer patterning is readily achieved with single pulses of 15- to 25-mJ/cm² fluence followed by development in fluorine-based RF plasma. The laser-induced reaction is thought to involve a structural transformation of WO_3 , which results in a more densely packed material and consequently in a reduced plasma etch rate. Laser-induced area-selective controlled changes in pore size may lend themselves also to a variety of nonlithographic applications where localized heterogeneous chemical reactions are desirable.

M. Rothschild
A. R. Forte

4.2 FAST ROOM-TEMPERATURE GROWTH OF SiO_2 FILMS BY MOLECULAR-LAYER DOSING

The scaling of microelectronic devices requires controlled, low-temperature methods for the growth of dielectric films. Process-induced thermal degradation must be avoided in smaller devices where interdiffusion is more critical, and deposition must often be into deeper and more recessed structures, e.g., trenches, in increasingly three-dimensional devices.

In this report, we describe a technique for film growth based on the room-temperature reaction of adsorbed molecular layers of water and silicon (or metal) halides. The technique has been developed primarily to obtain continuous, conformal, hermetic SiO_2 films at thicknesses below 30 nm. The adlayer dosing technique is based on conditioning substrates to critical, prescribed coverages of adsorbed water and then reacting this layer with SiCl_4 . In the sense that it takes advantage of high molecular surface mobility and the self-assembly characteristics of adsorbates, the approach is similar to that of atomic-layer epitaxy. However, to achieve low process temperature, hydrolytic rather than pyrolytic reactions are used. These reactions are run continuously by controlling the adsorbate species in steady-state equilibrium with a mixed vapor or by sequential cycling of ambients. Similar hydrolytic reactions have been studied for several polymer modification applications [13],[14]. Nakano et al. [15] have demonstrated a conceptually similar technique for SiO_2 growth by metered cycling of SiH_4 and discharged oxygen.

The steps in this new technique are as follows: (1) Normal hydrophilic substrates are loaded into a turbomolecular-pumped vacuum system (base pressure, mid- 10^{-7} Torr). In practice, nearly all silicon process wafers (bare, thin film, or resist-coated) will support the technique. However, for uniformity, we standardized to oxygen-plasma-ashed wafers for the experiments reported below. (2) The substrates are dosed with water vapor at a pressure between 0.2 and ~ 3 Torr. Near room temperature, this pressure is sufficient to consistently form a multilayer of adsorbed H_2O . (3) The excess water is rapidly evacuated to retard homogeneous vapor-phase reactions. (4) An ambient pressure (~ 5 Torr) of SiCl_4 vapor is introduced and allowed to react with the adsorbed water layer. (5) The SiCl_4 vapor is purged and the cycle is repeated for layer-by-layer growth. In our system this sequence is automated using computer control, with electronic valves and closed-loop feedback from the pressure sensors. In addition, the chamber walls and gas manifold are heated to ~ 50°C to prevent the stable formation of the H_2O multilayer and thereby greatly retard deposition on the apparatus. In practice, we have found that near room temperature the surface reactions are dominant and, at the expense of some precision in control of film thickness, step 3 can be eliminated. In this case, the reaction proceeds continuously on the substrate surface until the depletion of reactants or the buildup of reaction products terminates it.

Preliminary characterizations of the silicon oxide films have been made by various methods. The index of refraction under most growth conditions is 1.45. At least to the sensitivity of Auger electron spectroscopy and XPS (~ 1 at.%), films are stoichiometric SiO_2 without detectable metallic or halogen impurities. Deformation measurements on Si wafers at $1.0\text{-}\mu\text{m}$ growth thickness show the films to be under a small tensile stress. Capacitance-voltage measurements were conducted on films 100 to 200 nm thick grown on plasma-ashed silicon wafers. A breakdown voltage of 8 MV/cm is achieved consistently. The interface charge is negative at a density of 1 to $3 \times 10^{11} \text{ cm}^{-2}$.

In addition, qualitative measurements of hermeticity, using pinhole-decoration etching, were performed on films 30 to 50 nm thick. Process-related pinhole densities are extremely low and could not be quantified in our experiments as they were below the nominal ambient dust level in the laboratory. Resist-coated wafers, overgrown with SiO_2 layers, can be immersed for an hour in acetone with no visible solvent attack of the resist. In addition to resist technology, an important potential application, stemming from the unusual ability of the dosing reaction to conformally coat internal surfaces, is trench filling for VLSI. Figure 4-4 shows typical results of overgrowths made for this application.

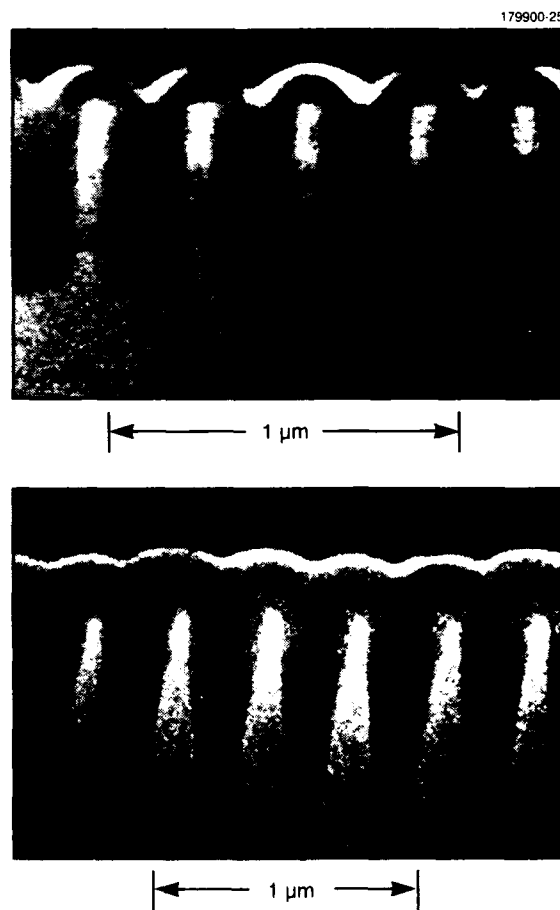


Figure 4-4. Scanning electron micrographs of silicon trenches filled by deposited oxides (cleaved profile). Note the excellent filling and planarization of the substrate topography. Typical growth conditions are 2-Torr H_2O , 5-Torr SiCl_4 , and $\sim 15\text{-min}$ total growth time.

The mechanism of the reaction has been studied in some detail using a quartz crystal microbalance mounted within the growth chamber. Measurements were made in real time by observing the rate of change of deposited mass and cross-calibrating the microbalance signal to final growth thicknesses using a surface profilometer. The strongest dependences are on variations of the H_2O pressure and substrate temperature, as shown in Figures 4-5 and 4-6, respectively. At low H_2O pressure, below 0.05 Torr in Figure 4-5, there is no appreciable reaction. This result is independent of the duration of exposure and is true over a wide temperature range near room temperature. Above ~ 0.1 Torr, the reaction rate begins to grow exponentially. It then saturates to a nearly linear increase with H_2O pressure at values exceeding ~ 0.5 Torr. The magnitudes of the exponential and linear rate increases depend on substrate temperature and increase with a decrease in the temperature, as long as it is above 0°C (see below). From the isotherm in Figure 4-5, note that the coverage of physisorbed H_2O is already large in the region of no appreciable reaction (< 0.05 Torr). The substrate-temperature dependence of the reaction rate at constant 0.28-Torr H_2O and 5-Torr SiCl_4 pressure conditions is shown in Figure 4-6. There is a rapid increase in rate as the substrate temperature is reduced. The rate peaks and falls rapidly at a temperature which, to the accuracy of our absolute thermal measurements ($\pm 1^\circ\text{C}$), appears to be the H_2O bulk-liquid freezing point (0°C). Below this temperature, rates under all pressure conditions appear to be extremely slow. The rates also diminish rapidly with temperature elevation above room temperature.

The nonlinear dependencies on pressure and substrate temperature are consistent with a mechanism of growth controlled dominantly by the distinct phases of adsorbed H_2O . On SiO_2 surfaces [16] these are commonly classified into (1) chemisorbed structural OH, which terminates normal oxide surfaces at approximately monolayer (2.4 to $2.7 \times 10^{14} \text{ cm}^{-2}$) coverage, on top of which form (2) "coordination-bound" H_2O and (3) hydrogen-bonded H_2O . Coordination-bound H_2O develops at low (< 0.1 Torr) pressure; we tentatively associate the knee observed near 0.15 Torr in the isotherm of Figure 4-5 with the saturation of this phase. Coordination-bound H_2O is probably composed of several spectroscopically distinguishable species. The third phase, hydrogen-bonded H_2O , is characterized by high mobility and rapid equilibration with the vapor phase. We tentatively associate the rapid reduction in rate at 0°C (Figure 4-6) with freezing of this last species into a less reactive solidlike phase.

Above ~ 0.5 -Torr H_2O pressure, where the coordination-bound H_2O coverage is saturated, the linear region of the hydrogen-bonded H_2O isotherm becomes dominant, and the SiCl_4 reaction can be thought of as titrating the instantaneous coverage of hydrogen-bonded H_2O . For example, the ratio of rates (13°C) between 1- and 2-Torr H_2O pressure is 1.9, corresponding well to the ratio of 1.8 in measured hydrogen-bonded H_2O coverage. The temperature dependence in Figure 4-6 derives from the variation of the H_2O saturation vapor pressure with temperature. In passing, we note that the efficiency of the reaction measured against surface collision frequency is relatively low, $\sim 10^{-5}$ to 10^{-6} reactions per SiCl_4 surface collision, even under fast growth conditions (12°C , 2-Torr H_2O , 5-Torr SiCl_4). This is consistent with the weak adsorption of SiCl_4 and a relatively slow reaction of the adsorbates.

Based on the foregoing, the sensitivity of the reaction to the state of hydration of the growth surface can be used to quantitatively control the rate of oxide deposition. We have found that this same sensitivity can also be used for selective-area growth. To demonstrate the latter, silicon wafers were first rendered hydrophobic (largely hydrogen terminated, see [17]) by dipping them in buffered HF and were then exposed in air to laser radiation with a 193-nm excimer projection imaging system. Laser radiation dislodges the hydrogen termination, permitting spontaneous oxidation and restoration of the hydrophilic

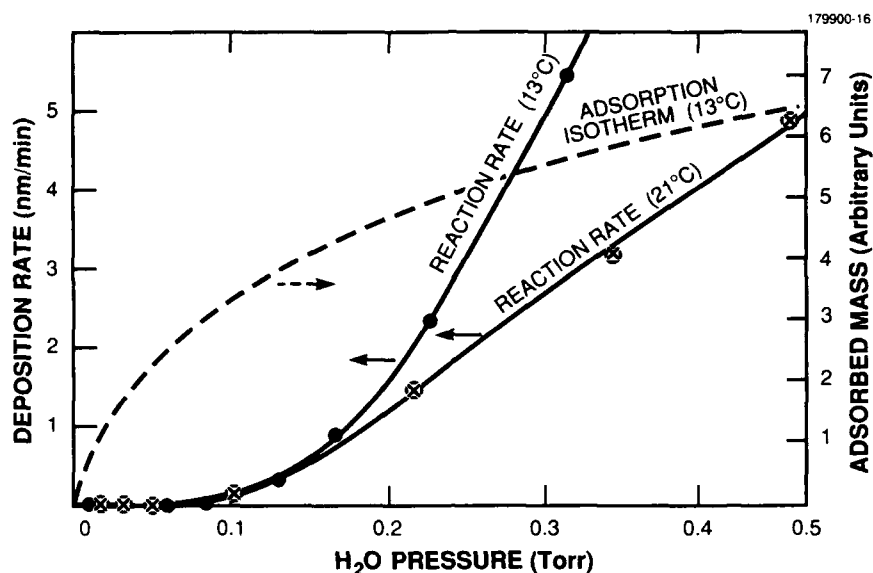


Figure 4-5. Low H₂O pressure measurements of SiO₂ deposition rates. The H₂O adsorption isotherm (13°C) on the growth surface, measured in the same apparatus, is shown as a dashed line.

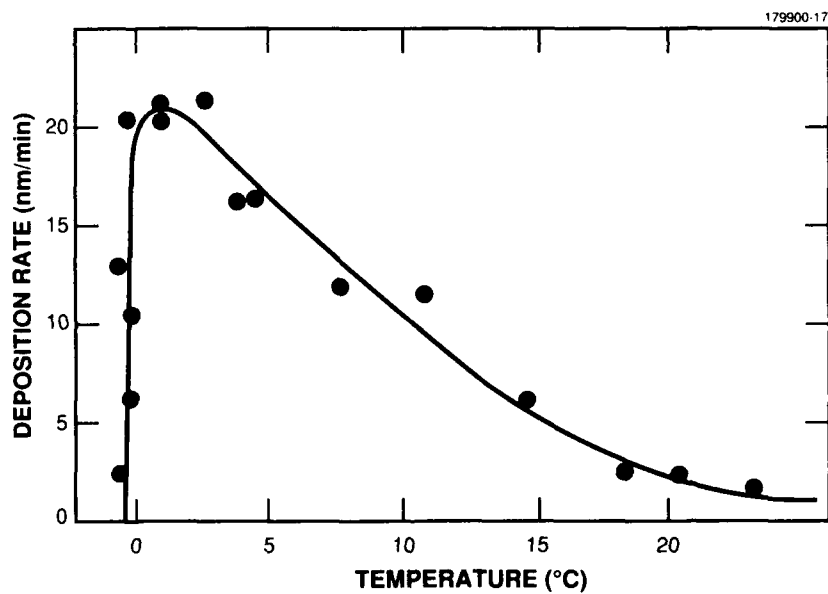


Figure 4-6. Dependence of SiO₂ deposition on substrate temperature at fixed 0.28-Torr H₂O and 5-Torr SiCl₄ pressures. The solid curve is drawn as an aid to the eye.

surface properties in exposed regions. The irradiated regions then support the H₂O adsorbates. Both single high-power (> 50 mJ/cm²) and multiple low-power (~ 100 pulses at 1 mJ/cm²) pulses are successful in this surface modification. Patterned surfaces are then placed in the SiO₂ growth chamber where they demonstrate selective-area growth. A 1- μ m spatial resolution has been achieved in the initial experiments. Separate experiments show that, even without optimization, the rate selectivity between irradiated and unirradiated regions exceeds 100:1 for growths to an oxide thickness range of 50 to 100 nm.

In conclusion, the molecular dosing technique produces SiO₂ films that are conformal, even on recessed surfaces, and are hermetic at thicknesses of several tens of nanometers. The deposition process operates optimally at 0 to 23°C and produces films with useful physical and dielectric properties. The process is accurately controlled over many orders of magnitude in rate by adjusting the coverage of adsorbed H₂O, and it should be extendable to other metal oxides. Applications to trench filling and photoresists are under development.

D. J. Ehrlich
J. Melngailis

REFERENCES

1. S. K. Deb, *Philos. Mag.* **27**, 801 (1973).
2. O. F. Schirmer, V. Wittwer, G. Baur, and G. Brandt, *J. Electrochem. Soc.* **124**, 749 (1977).
3. N. Yoshiike and S. Kondo, *J. Electrochem. Soc.* **130**, 2283 (1983).
4. N. Koshida and O. Tomita, *Jpn. J. Appl. Phys.* **24**, 92 (1985).
5. M. Baba and T. Ikeda, *Jpn. J. Appl. Phys.* **20**, L149 (1981).
6. A. Bensaoula, E. Grossman, and A. Ignatiev, *J. Appl. Phys.* **62**, 4587 (1987).
7. M. F. Daniel, B. Desbat, J. C. Lassegues, and R. Garie, *J. Solid State Chem.* **73**, 127 (1988).
8. C. D. Wagner, W. M. Riggs, L. E. Davis, J. F. Moulder, and G. E. Mullenberg (eds.), *Handbook of X-ray Photoelectron Spectroscopy* (Perkin-Elmer Corp., Eden Prairie, Minn., 1979).
9. G. S. Oehrlein and J. L. Lindström, *J. Vac. Sci. Technol. A* **7**, 1035 (1989).
10. F. R. McFeely, J. F. Morar, and F. J. Himpsel, *Surf. Sci.* **165**, 277 (1986).
11. J. J. Kleperis, P. D. Cizmach, and A. R. Lulis, *Phys. Status Solidi A* **83**, 291 (1984).
12. A. Agrawal and H. Habibi, *Thin Solid Films* **169**, 257 (1989).
13. L. E. Stillwagon, M. J. Vasile, F. R. Briocchi, P. J. Silverman, and G. N. Taylor, *Microelectron. Eng.* **6**, 381 (1987).
14. N. Awaya and Y. Arita, *Jpn. J. Appl. Phys.* **27**, 1172 (1988).
15. N. Nakano, H. Sakaue, H. Kawamoto, A. Nagata, M. Hirose, and Y. Horiike, *Appl. Phys. Lett.* **57**, 1096 (1990).

16. See, for example, V. F. Kiselev and O. V. Krylov, *Adsorption Processes on Semiconductor and Dielectric Surfaces I*, Springer Series in Chemical Physics, Vol. 32 (Springer-Verlag, Berlin, 1985), pp. 109-140.
17. V. Burrows, Y. J. Chabal, G. Higashi, K. Raghavachari, and S. B. Christman, *Appl. Phys. Lett.* **53**, 998 (1988); D. Fenner, D. K. Biegelsen, and R. D. Bringans, *J. Appl. Phys.* **66**, 419 (1989). An alternative plasma process to achieve hydrogen termination has been demonstrated by T. Hsu, B. Anthony, R. Qian, S. Banerjee, and A. Tasch, to be published in *J. Electron. Mater.*

5. HIGH SPEED ELECTRONICS

5.1 VACUUM FIELD-EMITTER TRIODE

As a transport medium for an electronic device, vacuum offers electron velocities and a maximum field at breakdown that are superior to those of any semiconductor. Microelectronics technology has now progressed to the point that it appears feasible to make high-performance microelectronic devices in which the electron current passes through a vacuum rather than through a semiconductor channel. Figure 5-1 depicts a microminiaturized analog of a traditional vacuum triode, called a vacuum field-emitter triode (VACFET), that we are now fabricating. It consists of an array of microtriode cells, each sealed under vacuum and containing a single knife-edge field-emission cathode. Electron flow is controlled by grid fingers sandwiched between two SiO_2 insulators, and the current is collected by an anode atop the structure. Theoretical calculations indicate that VACFETs may in the future demonstrate operating frequencies, breakdown voltages, and output power levels over 10 times higher than those of conventional Si and GaAs microelectronic devices. The fabrication technology for this device is a direct outgrowth of our permeable base transistor technology.

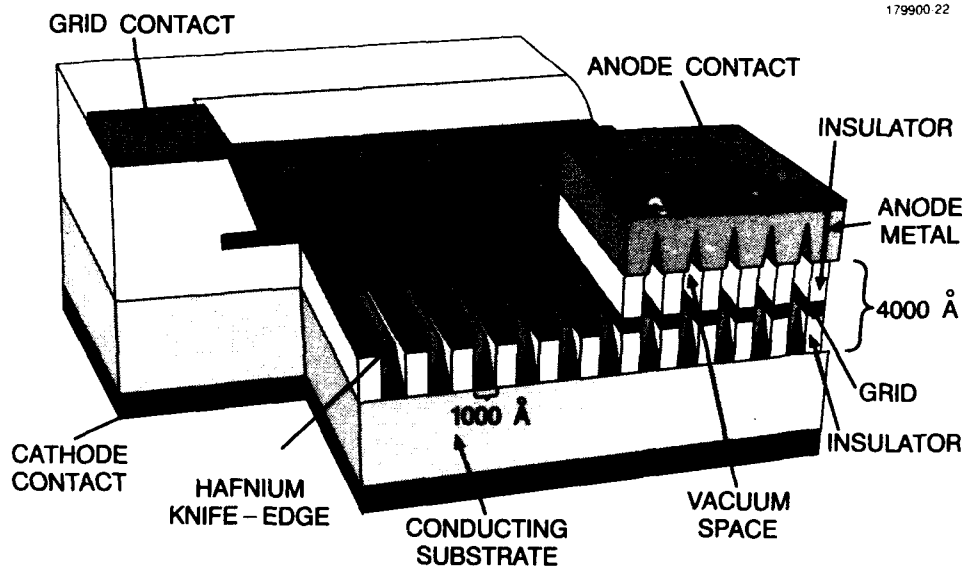


Figure 5-1. Schematic view of a VACFET. The high field between the grid and each knife-edge causes electrons to emit from the knife-edges into the vacuum spaces. The electrons then move ballistically to the positively biased metal anode. A small variation in voltage on the grid causes a large variation in anode current.

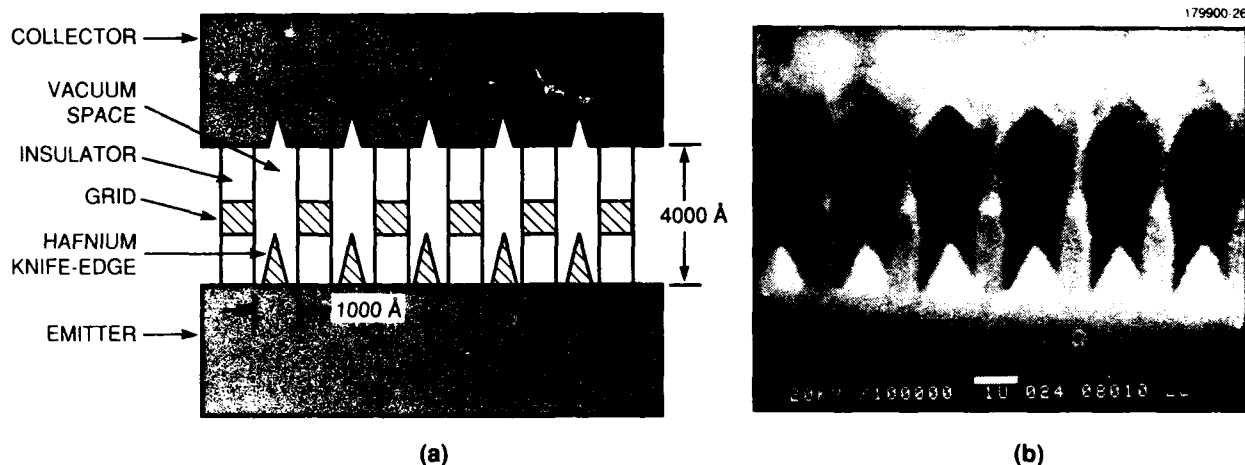


Figure 5-2. VACFET shown in (a) a cross-sectional drawing and (b) an SEM. Grooves 100 nm wide are cut through an insulator-metal-insulator sandwich, and then hafnium is evaporated to form the knife-edges as well as to close off the vacuum spaces.

Figure 5-2(a) shows a schematic cross section of a VACFET, and Figure 5-2(b) depicts a scanning electron micrograph (SEM) of the cross section of a fabricated device. The grating periodicity in these devices is $0.2\ \mu\text{m}$, making them by far the smallest-geometry vacuum triodes ever reported. The structures are made by first defining the grating in the insulator/metal/insulator sandwich by using laser holography and reactive ion etching. A low-work-function material, such as hafnium, is then evaporated through the grating to form an array of knife-edge emitters with edge radii $< 5\ \text{nm}$ and a total edge length of 2 mm. In this fabrication process, formation of the anode and closure of the vacuum cavity are achieved by the buildup of the evaporant used for the emitter. The anode is subsequently thickened with an additional evaporation of aluminum. Because the vacuum seal is made in situ, there is no need to test these devices in a vacuum system, and their electrical characteristics can be measured with a conventional probing station after only one day of additional processing beyond the formation of the emitters. The very small dimensions of these structures result in sharper knife-edges than have been achieved in the past using a similar technique and, in addition, make the in situ vacuum sealing practical. The thickness of the evaporation required to form the emitters is $< 300\ \text{nm}$, thereby avoiding the high stress of thicker films, which can cause peeling and roughening.

An SEM of a finished VACFET fabricated on a Si wafer is shown in Figure 5-3. The anode and grid contacts can be seen on the top surface of the wafer. These devices have achieved anode breakdown voltages $> 50\ \text{V}$, but the anode current density is still relatively modest at $100\ \text{A}/\text{cm}^2$. The fabrication scheme allows a variety of metals to be used for emitters, and we plan to employ the structure of Figure 5-3 to evaluate the emission properties of a range of metals so that the emitters can be optimized for higher current densities.

C. O. Bozler
S. Rabe



Figure 5-3. SEM of a completed VACFET. The internal vacuum cavities of the device are sealed during the fabrication process, enabling these devices to be subsequently tested and used in circuits in the same manner as typical semiconductor devices.

5.2 ELECTRICAL AND STRUCTURAL CHARACTERIZATION OF GaAs VERTICAL-SIDEWALL LAYERS GROWN BY ATOMIC LAYER EPITAXY

We report the use of chlorine ion-beam-assisted etching (IBAE) [1], atomic layer epitaxy (ALE) [2], and a wrap-around ohmic contacting technique to fabricate novel test structures incorporating GaAs vertical-sidewall epilayers. The ALE was performed in an organometallic vapor phase epitaxy reactor. Our study represents the first reported work to characterize horizontal conducting channels fabricated with vertical-sidewall ALE epilayers. Preliminary results indicate that these layers are of sufficient quality to support a sidewall epitaxy device technology. Some examples of candidate electronic, electrooptic, and photonic devices are vertical transistors, waveguides, tapered-waveguide antennas [3], lasers and modulators, and quantum wire and dot lasers.

The test structure, shown schematically in Figure 5-4, consists of a semi-insulating (SI) GaAs rod about $2\text{ }\mu\text{m}$ high and $75\text{ }\mu\text{m}$ long that has conducting epilayers grown by ALE on the two long vertical sidewalls and wrap-around ohmic contacts at the two ends. The rod is formed by chlorine IBAE on a SI GaAs (100) substrate. The long axis of the rod lies along the $[0\bar{1}1]$ direction. For this orientation, ALE yields conformal epilayers of the same thickness on both horizontal and vertical surfaces. After growth of the ALE layer, the wrap-around contact pads, spaced about $25\text{ }\mu\text{m}$ apart, are formed by a lift-off and anneal process using a two-level resist and an angled-evaporation Au/Zn/Au metallization [4] scheme. After contact formation, the horizontal epilayers deposited on the portions of the substrate and rod (top) that are not covered by contacts are removed by chlorine IBAE to isolate the test structures from one another and to form conducting paths solely on the sidewalls. Figure 5-5 is an SEM showing a completed test structure that has p -type (grown unintentionally doped) ALE layers 200 nm thick.

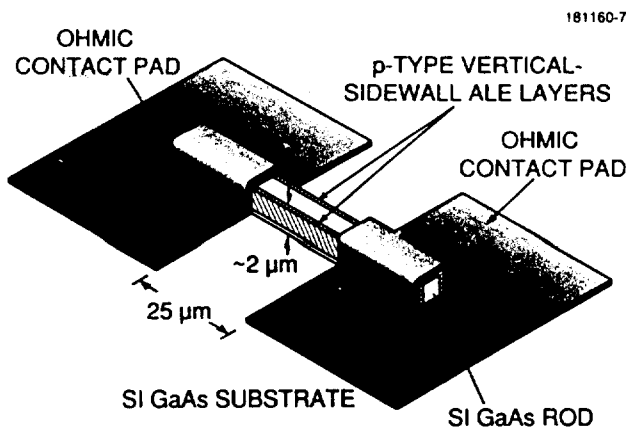


Figure 5-4. Schematic diagram of a test structure consisting of a GaAs rod with vertical-sidewall epilayers and wrap-around ohmic contacts.

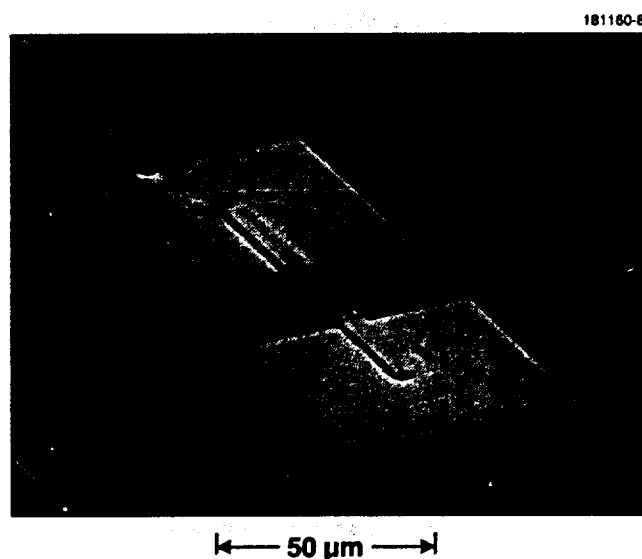


Figure 5-5. SEM showing a vertical-sidewall test structure.

An SEM of the cross section of an overgrown $[0\bar{1}1]$ rod is shown in Figure 5-6. A thin GaAlAs layer was used to mark the substrate-epilayer interface in this run, and a selective etch was used to delineate the marker. Other orientations gave various ratios of horizontal to vertical layer thickness, which may be of interest in specific devices. Cross-sectional transmission electron micrographs (TEMs) showed the epilayers to be of high crystalline quality. Figure 5-7 is a cross-sectional TEM showing the interface between an overgrown rod and one of the ohmic contacts. The contact alloyed uniformly into the GaAs epilayer with an interface roughness of ~ 80 nm.

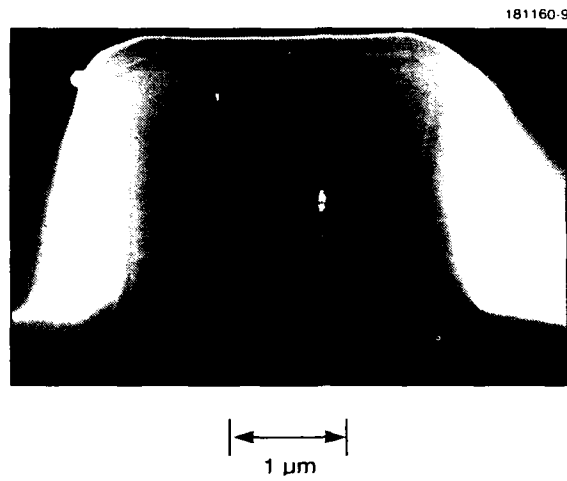


Figure 5-6. SEM of a cleaved and stained cross section from an overgrown rod. GaAlAs was used as an interface marker layer.

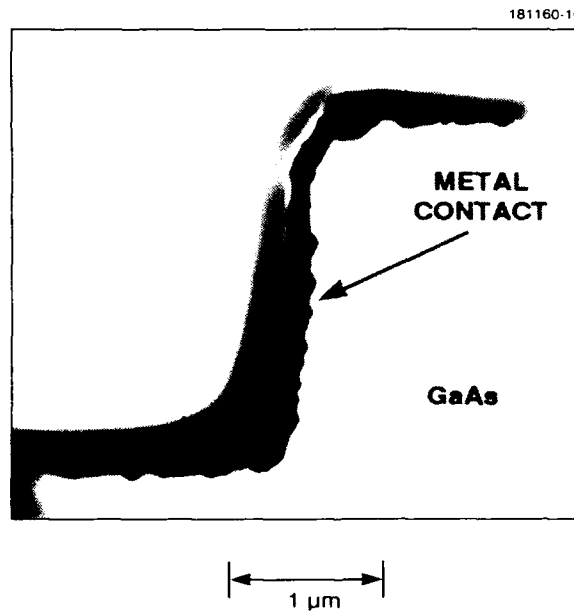


Figure 5-7. Cross-sectional TEM showing the interface between a GaAs ALE layer and an annealed ohmic contact. The interface roughness is about 80 nm.

The carrier concentration of the vertical-sidewall layers was determined using current saturation measurements [5]. Based on a saturation velocity of $2.4 \times 10^6 \text{ cm s}^{-1}$ for holes in GaAs, which we determined earlier [6], the concentration-thickness product of a sidewall layer was found to be $1.5 \times 10^{12} \text{ cm}^{-2}$. The carrier concentration measured for horizontal layers on the same wafer was $2.2 \times 10^{17} \text{ cm}^{-3}$, and the total depletion width from the interface into the layer and the surface into the layer was 145 nm. On the assumption of the same depletion width for the vertical layers, the active channel width for the layers is 55 nm, which corresponds to a carrier concentration of $\sim 2.8 \times 10^{17} \text{ cm}^{-3}$.

D. B. Gladden

W. D. Goodhue

C. A. Wang

G. A. Lincoln

REFERENCES

1. W. D. Goodhue, G. D. Johnson, and T. H. Windhorn, in *Gallium Arsenide and Related Compounds 1986*, W. T. Lindley, ed. (IOP Publishing, Bristol, England, 1987), p. 349.
2. Y. Ide, B. T. McDermott, M. Hashemi, S. M. Bedair, and W. D. Goodhue, *Appl. Phys. Lett.* **53**, 2314 (1988).
3. D. E. Bossi, W. D. Goodhue, M. C. Finn, K. Rauschenbach, J. W. Bales, and R. H. Rediker, *Appl. Phys. Lett.* **56**, 420 (1990).
4. H. J. Gopen and A. Y. C. Yu, *Solid-State Electron.* **18**, 331 (1975).
5. S. W. Pang, W. D. Goodhue, T. M. Lyszczarz, D. J. Ehrlich, R. B. Goodman, and G. D. Johnson, *J. Vac. Sci. Technol. B* **6**, 1916 (1988).
6. D. B. Gladden, S.M. thesis, Massachusetts Institute of Technology, Cambridge, Mass. (1991).

6. MICROELECTRONICS

6.1 SUPPRESSION OF CHARGED-PARTICLE EVENTS IN DEEP-DEPLETION CCD IMAGERS

Spaceborne charge-coupled device (CCD) imagers are subject to bombardment by highly energetic particles from the Van Allen belts, cosmic rays, and secondary radiation generated by the interaction of the external radiation with the spacecraft materials. Such radiation can generate substantial charge trails, amounting to several thousand electrons, and for sensors operating at low signal levels such extraneous charge can seriously obscure the desired signals. Visible-band CCD imagers are usually made on relatively thin ($\sim 10\ \mu\text{m}$) epitaxial material grown on heavily doped p -type substrates. In such devices, only electrons generated in the epilayer are detected, since the substrate has a very low minority-carrier lifetime. By contrast, CCD imagers intended for use as soft x-ray sensors are often made on high-resistivity p bulk material, and in these devices the minority-carrier lifetime is high through the entire wafer. The spurious charge created by energetic charged particles in such sensors will therefore be much greater than that for thin epilayer devices. One solution to this problem is to etch away as much of the substrate as possible, but this leaves the wafer more vulnerable to breakage. We have demonstrated an alternative method using a reverse-biased n^+/p junction, which reduces the charge-collection volume of the CCD by electrical means.

Figure 6-1 illustrates a cross-sectional view of the device and the method used to reduce bulk charge collection. The CCD used in these experiments is a 420×420 -pixel frame-transfer imager [1],[2] and is fabricated on p -type float-zone silicon with an acceptor concentration of $2 \times 10^{12}\ \text{cm}^{-3}$ (resistivity, $6500\ \Omega\ \text{cm}$). The depletion region created by the CCD gates at the upper surface of the device extends $\sim 80\ \mu\text{m}$ into the bulk. Our method of reducing bulk charge collection is to reverse bias an n^+ layer on the bottom surface with respect to the substrate. This creates a depletion region extending from the back surface into the bulk, and any electrons generated within this region are swept to the back contact. Fortunately, this n^+ layer is introduced into the back of the wafer for gettering purposes during fabrication, and therefore extra processing steps to add it to the device are not needed.

The extent of the back-surface depletion region as a function of the bias on the n^+ layer, or back-junction bias, is depicted in Figure 6-2. The depletion depth was determined by capacitance-voltage measurements. The calculated curve assumes an acceptor concentration of $2.17 \times 10^{12}\ \text{cm}^{-3}$, which is in good agreement with the value of $2.0 \times 10^{12}\ \text{cm}^{-3}$ obtained by spreading-resistance measurements on another wafer from the same lot. Of particular interest is that these spreading-resistance measurements were performed on a wafer before any high-temperature treatment, thus indicating that our device processing does not change the wafer resistivity. Ultrahigh-purity silicon has historically been difficult to use because of the resistivity changes after processing steps in a high-temperature furnace.

The results in Figure 6-2 show that a substantial fraction of the substrate can be depleted by this method. The back-junction voltages may seem high, but because of the very low p doping the peak electric field at the n^+/p junction is less than $8 \times 10^3\ \text{V/cm}$ at a bias of 100 V. This value is a factor of 40 below the intrinsic breakdown field in silicon. Leakage currents across this junction are typically $< 10\ \mu\text{A}$ at 100 V over the device area of $2.4\ \text{cm}^2$ at a temperature of -65°C .

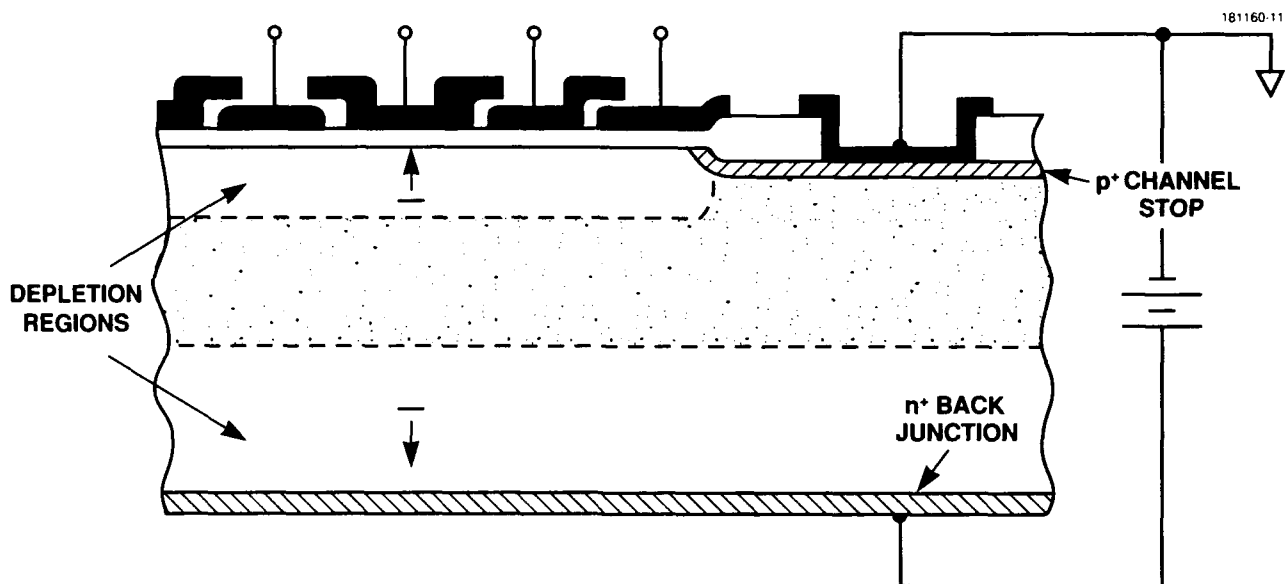


Figure 6-1. Cross section of a CCD imager with a reverse-biased n^+ back junction. Spurious charge generated in the lower depletion region by energetic charged particles is swept to the back junction in order to prevent collection of this charge by the CCD wells.

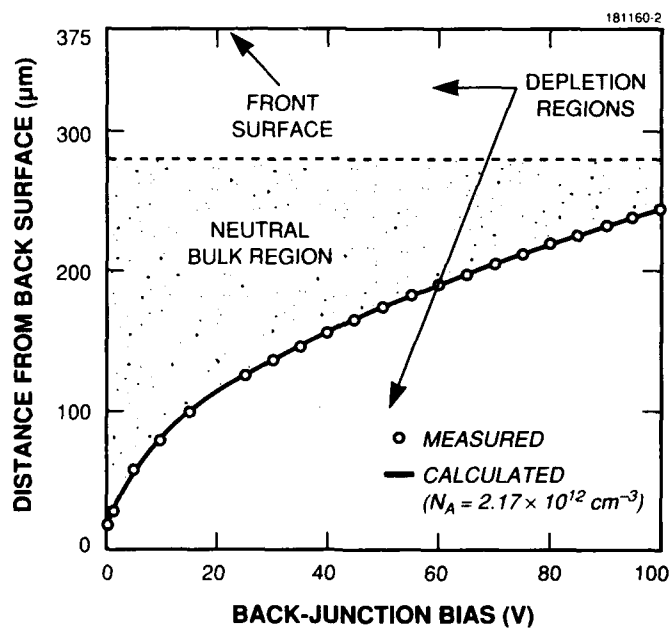


Figure 6-2. Depletion regions formed on the front surface of the device by the CCD and the back surface by the n^+ back junction. The back-surface depletion region was measured as a function of bias using capacitance-voltage measurements.

To test the effectiveness of this concept for reducing charged-particle events, a device was cooled to -75°C and irradiated by a weak Co^{60} source. The γ rays from this source generate energetic electrons in the device primarily from Compton scattering, and these electrons in turn lose energy by ionizing additional carriers. The ionization events detected by the CCD were measured as a function of the back-junction voltage. Figure 6-3 shows histograms of the quantity of charge per pixel from the device over a 30-s integration period for various back-junction voltages. In Figure 6-4, we show the number of instances in which a pixel registered more than $15 e^{-}$ (3σ above the device noise of $5 e^{-}$) as a function of bias. In both cases the suppression of the ionization events by the back depletion region is evident.

B. E. Burke

M. J. Cooper

B. B. Kosicki

6.2 MODELING OF PROTON-INDUCED VACANCY GENERATION IN Si

A CCD imager placed in orbit in the Van Allen radiation belts is subject to bombardment by energetic particles, with protons being the most prevalent species. These protons, with energies ranging from a few thousand to several hundred million electron volts, produce electron traps in the CCD that interfere with the charge-transfer efficiency of the device. These defects are believed to be created by the complexing of bombardment-induced vacancies with P dopant atoms in the buried channel [3]. Therefore, it is desirable to model vacancy generation in Si under proton bombardment, so that the level of degradation can be predicted and the effects of different proton spectra can be assessed. A program that can make these predictions is TRIM (TRAnsport of Ions in Matter), which exists in the public domain but runs at relatively slow rates. On a personal computer, up to 3 days may be needed to obtain meaningful data. Furthermore, limitations arise in modeling the behavior of protons as they decelerate to an energy $< 1 \text{ keV}$ (where many defects are formed in the lattice).

As a first step toward overcoming these difficulties, a computer program has been created that accurately predicts the differential generation rate of vacancies with run times of 20 min or less. The code is based on the modifications of Ziegler et al. [4] to the nuclear scattering theory of Lindhard et al. [5]. In this theory, the energy transferred to a target atom from a projectile atom depends on the mass, charge, atomic number, and relative velocity of the two particles, as well as the impact parameter (the distance of closest approach of the two particles if they were noninteracting). The effects of the first four of these parameters are simple to calculate, but the value of the impact parameter is probabilistic in nature. The TRIM program uses a Monte Carlo approach to generate the scattering parameters (including the kinetic energy transferred during an elastic collision) for many incident particles, where the impact parameter is controlled by a random number generator. On the other hand, the approach taken in the present program is to weight the impact parameter with the scattering cross section and numerically obtain the average kinetic energy transferred per collision, with all other operations in the model being performed analytically. Averaging the impact parameter in this fashion does limit the statistical spread of the results obtained, but for both techniques the calculations of the mean and standard deviation of the kinetic energy transferred agree quite well.

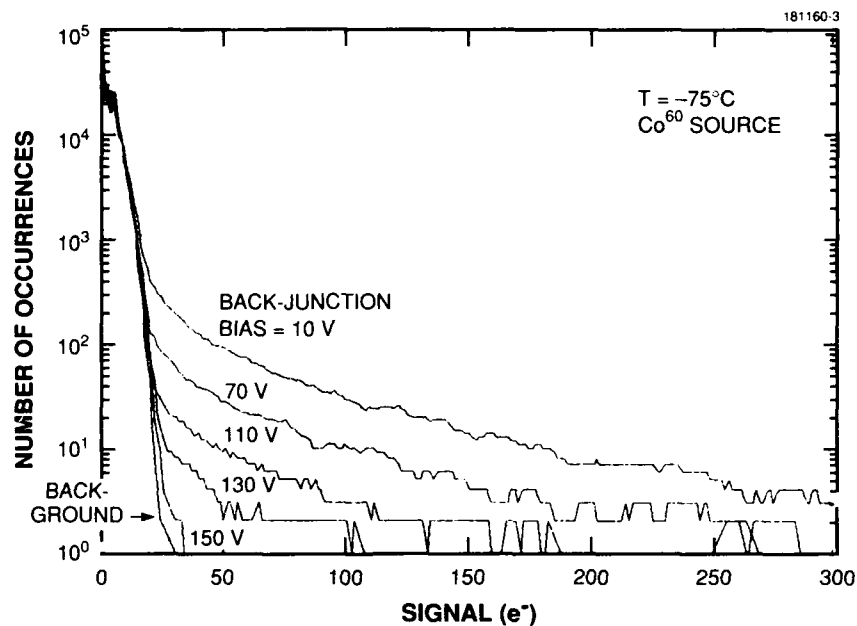


Figure 6-3. Histograms showing the frequency of charge events resulting from Co^{60} irradiation for various values of back-junction bias.

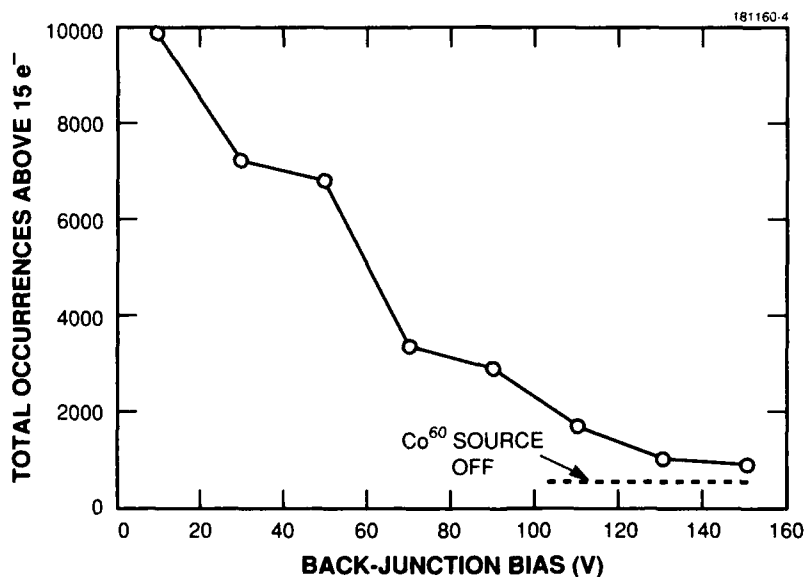


Figure 6-4. Total number of instances where a pixel contained more than $15 e^-$ as a function of back-junction bias under Co^{60} irradiation.

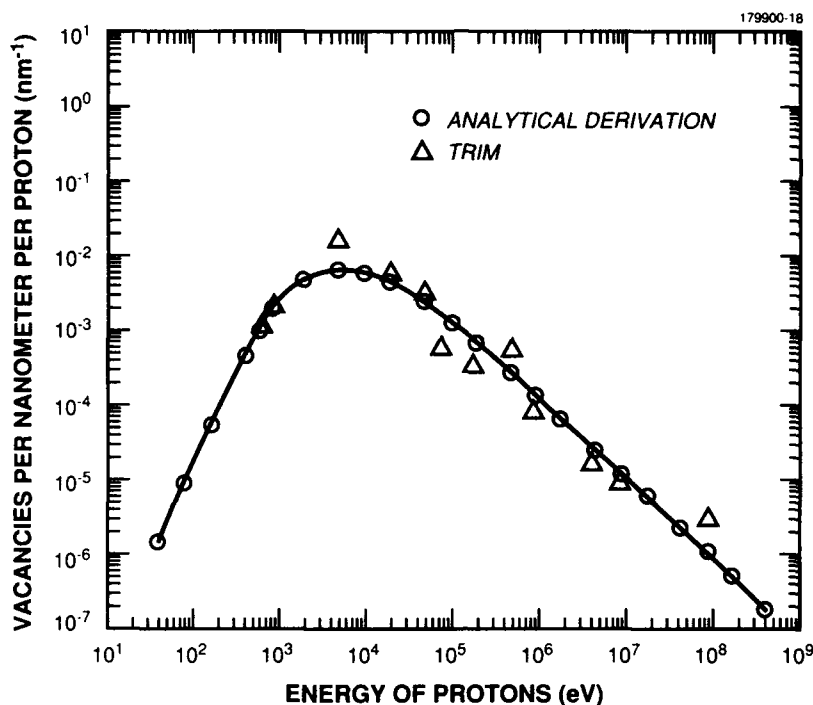


Figure 6-5. Differential vacancy production in Si by energetic protons.

The results of the calculation for generation of vacancies per nanometer per proton are shown in Figure 6-5 as a function of the proton energy. This differential generation rate applies to the ions as they first strike the Si surface or after they have decelerated to a specific energy within the Si. The total number of vacancies n generated by an ion as it passes from depth X_1 to X_2 in Si is given by

$$v = \int_{X_1}^{X_2} \frac{dv(E)}{dx} dx, \quad (6.1)$$

where $dv(E)/dx$ is the energy-dependent generation rate shown in Figure 6-5. The stopping cross section and range of protons in Si are well known [4], so for an incident energy E_0 it is possible to solve for the energy of the proton at distances between X_1 and X_2 and thereby to calculate v . It is apparent that the agreement is good between the analytical model and TRIM; the worst agreement is under those conditions where TRIM was run for periods of only several hours. The data include the vacancies that are generated by Si recoils moving through the lattice, that is, all the vacancies generated in a cascade. The Si recoils are emitted at an angle of 70 to 90° away from the incident proton velocity vector and travel less than 36 nm, so most of the vacancies are created at a depth near that of the primary recoil before it was displaced. Figure 6-5 also indicates that the most damage is created at an energy of several

thousand electron volts. It is important to note that protons striking Si with $E_0 = 100$ keV will have ~ 7 keV of energy remaining after penetrating 800 nm of Si, i.e., after partially traversing the buried channel and being in the vicinity of a charge packet. These considerations indicate that the interval for E_0 between 40 and 200 keV is the one most damaging to the CCD.

Work is under way to determine the effect of shielding on the spectrum of protons encountered at various altitudes of the Van Allen belts. The results of this work, when convoluted with the program described above, will predict the distribution of defects generated in the buried channel of the Si. This will allow us to alter the level of shielding and process conditions to minimize the damage occurring in the vicinity of the potential maximum of the buried channel, thereby improving the performance of proton-irradiated devices.

J. A. Gregory

REFERENCES

1. Solid State Research Report, Lincoln Laboratory, MIT, 1988:3, p. 61.
2. B. E. Burke, R. W. Mountain, D. C. Harrison, M. W. Bautz, J. P. Doty, G. R. Ricker, and P. J. Daniels, *IEEE Trans. Electron Devices* **38**, 1069 (1991).
3. Solid State Research Report, Lincoln Laboratory, MIT, 1990:2, p. 51.
4. J. F. Ziegler, J. P. Biersack, and U. Littmark, *The Stopping and Range of Ions in Solids* (Pergamon, New York, 1985).
5. J. Lindhard, M. Scharff, and H. E. Schiøtt, *K. Dan. Vidensk. Selsk. Mat. Fys. Medd.* **33** (14), 1 (1963).

7. ANALOG DEVICE TECHNOLOGY

7.1 QUAD CMOS BUFFER TO ENHANCE CCD CLOCKS

A quad CMOS buffer was produced using a 2- μ m CMOS/charge-coupled-device (CCD) process developed for Lincoln Laboratory at Orbit Semiconductor, Sunnyvale, California, for the realization of high-performance analog signal processing devices. This process technology was recently applied to the development of a CCD correlator and a serial-parallel-serial memory. The quad CMOS buffer evolved from the need for high-speed, full rail-to-rail (ground-to-supply) clock drive into a CCD's typically large capacitive load. When this project began, off-the-shelf devices were either adequately fast but not capable of providing the full required voltage swing, or they covered the appropriate range in voltage but had unsatisfactory rise and fall times. It was subsequently determined that the CMOS/CCD process should be adequate for the development of an appropriate device and that this test device could be included on the test wafer then under development for the full characterization of the intended process.

To provide the necessary performance, the CMOS buffer had to be capable of significant current drive for high-speed operation while possessing compact layout geometry for low levels of parasitics. Low parasitics are necessary to realize maximum speed and to minimize degradation of rail-to-rail output voltage swing due to inductive bounce on power and ground lines. (This latter concern was a problem in one of the tested off-the-shelf components.) It was further decided to configure the device as four isolated units in close proximity on a single die (to facilitate their incorporation into a single package) so that more drive could be provided by utilizing outputs from multiple buffers in parallel. Added drive could then be used to speed up rise and fall times into a fixed capacitive load or to maintain fixed values for rise and fall times into larger capacitive loads. Keeping the four buffers fully isolated from one another would prevent a surge in current in one buffer from coupling electrically to the others through a common power connection and thereby degrading their performance. Each buffer could be separately provided with decoupling capacitors for each of their dedicated power inputs.

The adopted circuit configuration for a single buffer is depicted schematically in Figure 7-1. The buffer consists essentially of two cascaded CMOS inverters. Two inverters are required to realize a noninverting condition. A stage of smaller MOSFETs precedes a stage of larger ones, which minimizes the capacitive drive requirement at the input of the buffer without compromising overall speed. The large transistors at the output were chosen to provide sufficient peak current capability to drive a 25-pF capacitive load from rail to rail (0 to 5 V) in about 1 ns. Although the design is simple, the real difficulty with this circuit resided in the realization of the optimum geometric layout of the MOSFET devices, both singly and in conjunction with one another, so as to minimize parasitics and thereby maximize performance. The final optimized layout for a single buffer is shown graphically in Figure 7-2(a) and in the photomicrograph in Figure 7-2(b). Common practice is to configure large transistors either as folded devices or as multiple parallel devices. Because of other layout constraints, the latter of the two approaches was adopted here. With a large transistor broken up into multiple smaller transistors with shared source and drain diffusions, parasitic resistance and capacitance are significantly reduced relative to a single large MOSFET, and the speed of the devices is thereby correspondingly improved.

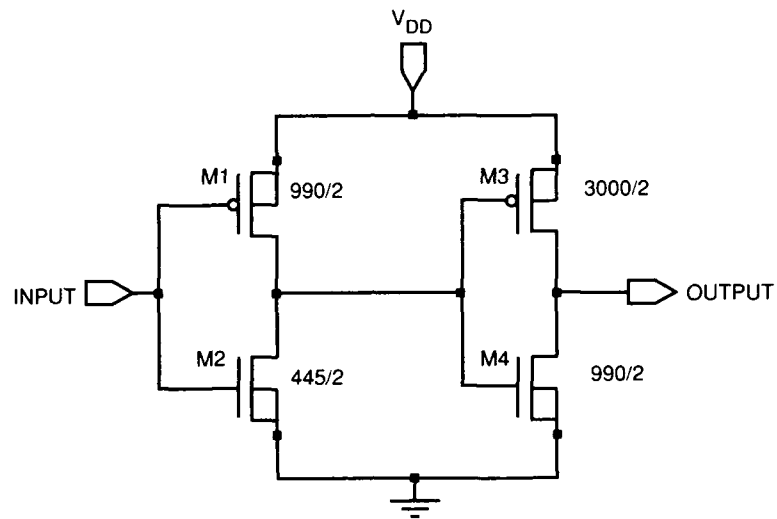
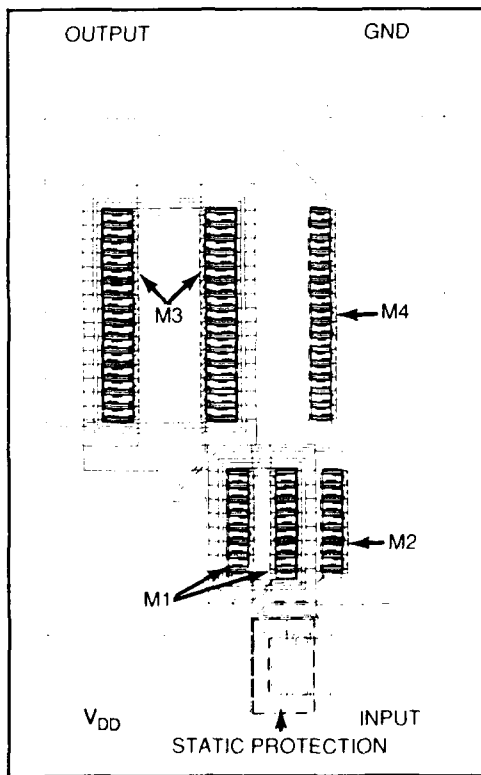
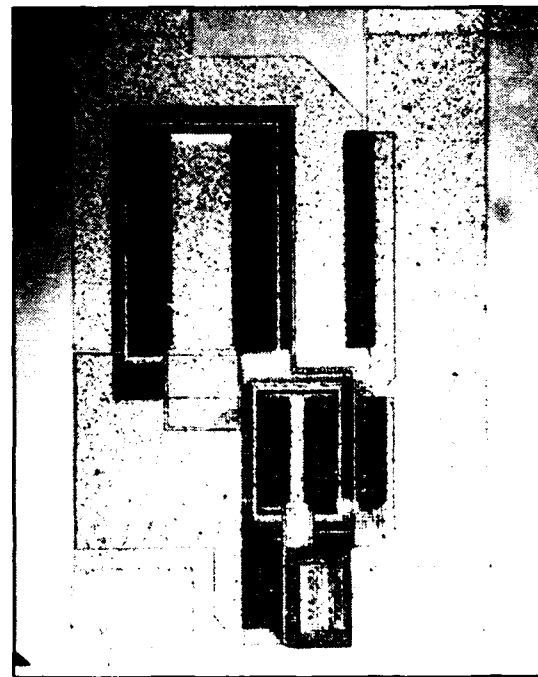


Figure 7-1. Schematic of a single unit of the quad CMOS buffer. Ratios depicted for MOSFETs M1 through M4 are the ratios of gate length to gate width for each device.



(a)



(b)

Figure 7-2. Optimized layout for a single unit of the quad CMOS buffer shown (a) graphically and (b) in a photomicrograph of an actual circuit.

Guard rings were incorporated around the p -type MOSFETs as a deterrent to latchup, which can result from the parasitic silicon-controlled-rectifier structures inherent in CMOS technology. A compact layout of the circuit was desirable for minimum parasitics but was hampered by the fact that MOSFETs could not be placed too close to one another without significantly increasing the risk of latchup. Care had to be exercised in this regard. Wide traces were utilized for power and ground to minimize inductive parasitics. To further improve performance, a decoupling capacitor was incorporated on the power line of each isolated buffer. Finally, since CMOS is susceptible to damage from static discharge, particularly at MOSFET gate connections, a static-protection circuit was placed at the input to each buffer.

The resultant quad CMOS buffer performed at a level commensurate with expectations. Rise and fall times into a 25-pF capacitive load for a single buffer were measured to be about 1.2 ns with a full rail-to-rail voltage swing. Since the device is CMOS, the standby (static) current is essentially zero. Of no small importance is the fact that this device functioned initially as one means of characterizing the CMOS/CCD process and as a preliminary means of verifying the accuracy of simulation results. The buffer currently represents a necessary component in the realization of support circuitry required in the test of CCD device prototypes.

D. B. Whitley
M. M. Seaver
D. R. Arsenault

7.2 MODES ON TWO- AND THREE-CONDUCTOR COPLANAR TRANSMISSION LINES

Locally confined modes on coplanar parallel strip transmission lines (called coplines) and their duals (obtained by interchanging conductor and gaps along the plane) propagate at natural characteristic impedance levels, which can be modified only slightly by reasonable choices for transverse dimensions. Calculations based on the quasi-TEM model and very thin conductors indicate that for a given average separation there is greater isolation between adjoining structures for properly designed systems of three conductors than for systems of two conductors. Figure 7-3 shows cross sections of coplines with conductors at the planar interface between two dielectric half spaces. The cross sections are complementary in the sense that metal and gaps are interchanged; the outside conductors in Figure 7-3(b) extend to infinity.

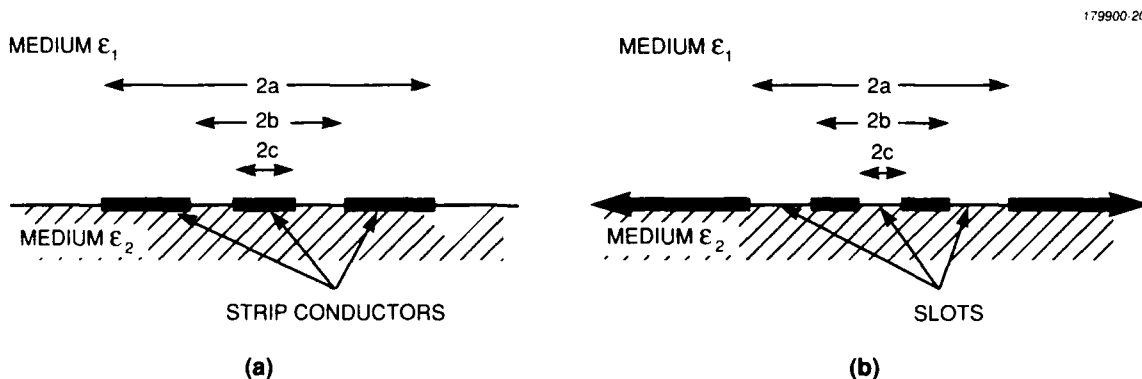


Figure 7-3. Cross sections of complementary coplanar lines showing (a) three conductors and (b) three slots.

The modes that can propagate on such structures are distinguished among other properties by the behavior of the E and H fields at low frequency and at a distance L that is large compared with the transverse dimensions of the conductors. Some of these modes have been named and studied extensively in the literature and others have not. In the interest of brevity, the structures (whether strips or slots) are here called coplines, and the useful modes are given letter designations.

When the lateral dimensions of the assemblage are small compared with a propagating wavelength it is common to make the quasi-TEM approximation, in which the wave speed v and nominal characteristic impedance Z_e are both Γ times that of free space:

$$v = c_0 \Gamma \quad (7.1)$$

$$Z_e \approx 120\pi \Gamma \text{ ohms} , \quad (7.2)$$

where c_0 is the speed of light in free space, Γ is given by

$$\Gamma = \left[2\epsilon_0 / (\epsilon_1 + \epsilon_2) \right]^{1/2} , \quad (7.3)$$

and ϵ_0 and $(\epsilon_1 + \epsilon_2)$ are, respectively, the dielectric constants of free space and the two dielectric media.

Propagation is said to be common mode when all conductors, such as those shown in Figure 7-3(a), are driven in parallel against a remote return path. For the common mode, it is necessary to know the return path (another conductor for strips, another slot for the dual) in order to define a characteristic impedance for the propagating wave.

Other modes are said to be compact because electric and magnetic fields drop off asymptotically as the inverse square or cube of distance from the conductor clusters. For some of these compact modes, the characteristic impedance is given in handbooks. When conductors are very thin compared with their lateral dimensions, all of the expressions for the characteristic impedance take the form [1]

$$Z_0 = Z_n \mu(k) , \quad (7.4)$$

where k is a combination of ratios of dimensions and $\mu(k)$ is a ratio of elliptic integrals, $K'(k)/K(k)$. For reasonable dimensional ratios, $\mu(k)$ cannot be far from unity; Z_n is thus a natural impedance level for the mode. In all cases investigated here, Z_n is either Z_e or $Z_e/4$.

Babinet's principle [2] states that if along the planar interface shown in Figure 7-3, metal is replaced by gap, and vice versa, the new structure will have a characteristic impedance Z_b given by

$$Z_0 Z_b = (Z_e/2)^2 . \quad (7.5)$$

This equation serves to define the impedances of these complementary structures. Table 7-1 arbitrarily names the various compact modes and gives the voltage excitation and natural impedance level. Note that a three-conductor configuration is called a triline and that the outside conductors are called flankers.

Observe a similarity between the P-mode triline with very wide flankers (row 3) and the infinite flanker FC mode (row 1). They are not really the same; all entries in the right-hand column have infinitely wide flankers. To avoid exciting the common mode, triline drive must be generally unbalanced so that drive $+V$ to a center conductor is accompanied by drive $-\zeta V$ to the others, as in Table 7-1, where ζ is a complicated function of a , b , and c . In terms of dimensions $2a$ and $2b$ (see Figure 7-3), calculations show that the parameter ζ drops to zero as $a \rightarrow \infty$ only as $2b/\pi a$.

For well-separated transmission lines, cross talk can be calculated from asymptotic formulas for the fields from one such line. The results are summarized in Table 7-2. They give only the amplitude of the electric coupling and do not take account of possibly differing values of Z_0 in different modes on the lines being coupled. (The quasi-TEM assumption implies that the magnetic coupling is the same as the electric.)

TABLE 7-1
Dual Compact Modes

Isolated Conductors	Slots Incised in Infinite Plane
$\begin{array}{c} \underline{-V} \quad \underline{+V} \\ \text{B mode} \\ \text{Balanced pair} \\ Z_n = Z_\epsilon \end{array}$	$\begin{array}{c} \leftarrow \underline{0} \quad \underline{+V} \quad \underline{0} \rightarrow \\ \text{FC mode} \\ \text{Single conductor with flanking} \\ \text{ground planes} \\ Z_n = Z_\epsilon/4 \end{array}$
$\begin{array}{c} \underline{-V} \quad \underline{0} \quad \underline{+V} \\ \text{S mode} \\ \text{Triline} \\ \text{Outer pair with balanced drive} \\ \text{Center conductor grounded} \\ Z_n = Z_\epsilon \end{array}$	$\begin{array}{c} \leftarrow \underline{0} \quad \underline{+V} \quad \underline{+V} \quad \underline{0} \rightarrow \\ \text{FP mode} \\ \text{Two conductors driven in parallel} \\ \text{against flanking ground planes} \\ Z_n = Z_\epsilon/4 \end{array}$
$\begin{array}{c} \underline{-\zeta V} \quad \underline{+V} \quad \underline{-\zeta V} \\ \text{P mode} \\ \text{Voltages are unbalanced unless} \\ a^2 = b^2 + c^2 \\ Z_n = Z_\epsilon/4 \end{array}$	$\begin{array}{c} \leftarrow \underline{0} \quad \underline{-V} \quad \underline{+V} \quad \underline{0} \rightarrow \\ \text{FS mode} \\ \text{Balanced pair with flanking ground} \\ \text{planes} \\ \text{Drive current of } \pm \zeta V/Z_0 \text{ to flankers} \\ Z_n = Z_\epsilon \end{array}$

TABLE 7-2

Intermodal Cross Talk Between Distant Coplines (or Between Their Duals)

From Source Line with Dimensions (a,b,c) or (b,c)	To Pickup Line with Dimensions (α,β,γ) or (α,β) at Distance L			
	Common Mode	B Mode (Dual: FC)	S Mode (Dual: FP)	P Mode $\alpha^2 = \beta^2 + \gamma^2$ (Dual: FS)
B Mode (Dual: FC)	$(b/\pi L)f(q)$	$(bA/\pi L^2)f(q)$	$(bA/\pi L^2)f(q)$	$(bA^2/2\pi L^3)f(q)$
S Mode (Dual: FP)	$(a/\pi L)f(q)$	$(aA/\pi L^2)f(q)$	$(aA/\pi L^2)f(q)$	$(aA^2/2\pi L^3)f(q)$
P Mode $a^2 = b^2 + c^2$ (Dual: FS)	$(ab/\pi L^2)f(q)$	$(2abA/\pi L^3)f(q)$	$(2abA/\pi L^3)f(q)$	$(3abA^2/2\pi L^4)f(q)$
$A = \alpha + \beta$ $f(q) = 1 + 2\sum_{m=1}^{\infty} q^{m^2}$, where $q = \exp(-\pi Z_0/Z_n)$ for the source line.				

In Table 7-2, (a,b,c) or (b,c) are the dimensions of the source transmission line, while (α,β,γ) or (α,β) are the dimensions of the pickup transmission line at remote distance L . For each column of Table 7-2, the lowest coupling occurs for P-mode triline and their duals, with remotely induced voltage varying as $1/L^4$.

R. M. Lerner

7.3 SOLID STATE ELECTROCALORIC REFRIGERATION

At temperatures down to the liquid nitrogen range, the thermal volume expansion of a material is the means by which thermal and electrical properties can be coupled by electrostriction. The modest thermal expansion and piezoelectric coupling of solids limit electrocaloric heat pumps to no-load temperature differentials of only a degree or two per stage and to discouraging coefficients of performance (COP).

To understand why an electric or magnetic field can cause heating or cooling, it is helpful to think of ordinary thermal expansion as due to thermally induced changes in the internal pressure exerted by a dense phonon gas. Conversely, if the volume of the material changes, the resulting change in gas volume alters its temperature. It immediately follows that if applied fields can cause a volume change, they can cause heating or cooling. For an applied electric field E , the effect is called electrocaloric.

The phonon gas behaves classically for temperatures down to about 1/6 of the Debye temperature

Θ_D . For most materials $\Theta_D/6$ is well below 75 K. The following discussion considers the possible use of the electrocaloric effect for refrigeration at such "ordinary" temperatures. In principle it is possible for a substance to be electrocaloric without dimensional changes, but such phenomena are negligible [3]. The situation is entirely different if $T \ll \Theta_D/6$, but that case [4] is beyond the scope of this report.

At ordinary temperatures, the fractional temperature change of the (ideal) phonon gas cannot exceed the fractional volume change. The latter is in turn limited by the strength of materials to at most a few percent. In fact, the actual change is less, partly because of the possibility of fatigue failure due to repeated cycling and partly because of breakdown limits on the applied electric field strength.

Given such limits, there are two electrostrictive effects that can be used for refrigeration. The first utilizes lattice volume changes occurring over a range of a few degrees around the ferroelectric Curie temperature. (Crystals of class $3\bar{m}$ behave as antiferroelectric but can exhibit the electrocaloric effect. Otherwise, all electrocaloric materials are also ferroelectric.) The sign of this effect does not depend on the direction of the dipole. The second involves volume changes resulting from body forces exerted when a field is applied to a permanent dipole. Here, the sign of the volume change does depend on the directions of field and dipole.

Attempts to build electrocaloric (or magnetocaloric) coolers have achieved no more than 1% in temperature per stage. It has been suggested that larger temperature changes can be obtained by stacking individual elements each having a ΔT of a degree or two. Here, the practical question is the COP, which is the ratio of heat moved to mechanical or electrical input. For small temperature differentials ΔT around absolute temperature T , the theoretical COP is $T/\Delta T$.

The COP of the stack is limited by the COP of the individual stage. Let the polar axis of a ceramic or plastic be the c axis, let d_3 be the volume piezoelectric coefficient, and let β be the volumetric temperature coefficient of expansion. Then, small signal changes in volume V , entropy per unit volume S , and electric displacement D are connected to changes in temperature T , pressure P , and electric field E by the thermodynamic relations

$$dS = \left(C_p / T \right) dT + q dE - \beta dP \quad , \quad (7.6a)$$

$$dD = q dT + \epsilon dE - d_3 dP \quad , \quad (7.6b)$$

$$dV / V = \beta dT + d_3 dE - \kappa dP \quad , \quad (7.6c)$$

where C_p is heat capacity at constant pressure per unit volume of material, ϵ is the dielectric constant, and κ is the isothermal compressibility, all at constant pressure; here, q is the so-called secondary pyroelectric coefficient. After various algebraic manipulations one finds that

$$C_p - C_v \equiv \delta C = \beta^2 T / \kappa \quad (7.7)$$

and

$$q = d_3 \beta / \kappa \quad . \quad (7.8)$$

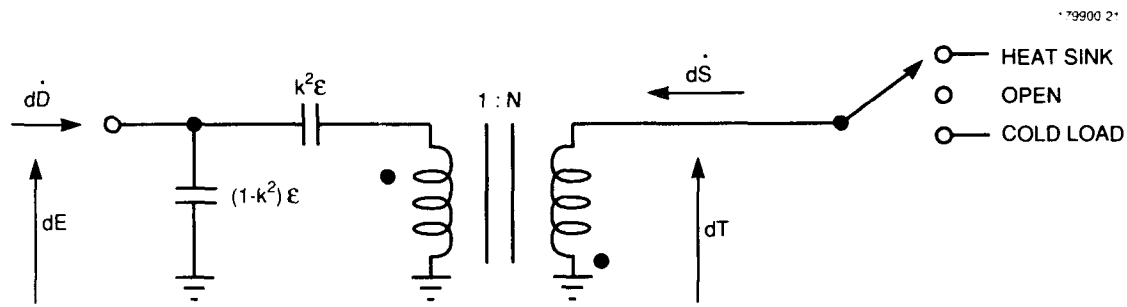


Figure 7-4. Electrocaloric equivalent circuit. The ideal transformer turns ratio N is determined by electric and thermal units. The dots over D and S denote the time derivatives.

At constant pressure, Equations (7.6a), (7.6b), and (7.6c) have equivalent circuits that have been thoroughly investigated in the domain of ultrasonic transducers. One such circuit is shown in Figure 7-4. The nondimensional coupling coefficient k^2 and turns ratio N are given by

$$k^2 = q^2 T / \epsilon C_p \quad (7.9)$$

and

$$N = k (T \epsilon / C_p)^{1/2} \quad (7.10)$$

The refrigeration cycle being implemented determines the protocol for connecting the switch to heat sink, nothing, and cold load as the input voltage is cycled (not necessarily sinusoidally). This switching does not affect the equivalent circuit.

Thermodynamic calculations show that the effective COP of these circuits can be no greater than the maximum theoretical COP multiplied by the energy efficiency η of the circuit as a transducer. The most effective utilization of such circuits occurs when both input and output are made resonant. Although no one seems to have done so, resonance can be implemented at the electrical input, even for very slow cycles, in the form of so-called resonant charging of the input capacitor.

However, such (fast) charging may be practical only for the adiabatic parts of a refrigeration cycle; further heat-flow-limited changes during the isothermal parts may be too slow. Moreover, there is no thermal inductance with which to resonate the output heat capacity. The conservative option is to assume nonresonant arrangements like those in the literature. For these, the maximum η is simply the coupling coefficient k^2 . Use of Equations (7.7) through (7.10) and some algebra then results in

$$\eta \leq k^2 = \beta^2 (d_3)^2 T / \kappa^2 C_p \epsilon = [(d_3)^2 / \kappa \epsilon] \delta C / C_p \quad (7.11)$$

On the far right-hand side, η is reduced to the product of two factors, η_1 and η_2 . The first can be recognized as the piezoelectric coupling coefficient for the material. The second is the relative difference in specific heats. Both are less than unity. The maximum value for η_1 is $< 1/3$. For solids, the maximum value of $\delta C / C_p$ is only a few percent.

Thus, the COP of an individual stage is likely to be $< 1\%$ of the maximum theoretical COP. This is confirmed by reports that values of ΔT of the order of 2 K have been achieved [5] with 85 to 90% energy efficiency. What should have been reported was the entropy efficiency (or fraction of theoretical COP) η . For $T = 300$ K and $\Delta T = 2$ K, the latter is a factor of 150 lower than the former. Such performance must compete with practical room-temperature refrigerators whose COP is roughly 30% of theoretical, and with mechanical cryocoolers that operate with COPs that are 10 to 20% of theoretical.

No concatenation of such stages will improve the result. One concludes that for temperatures above $\Theta_D/6$, the electrocaloric cooler is not an attractive or competitive means of refrigeration.

R. M. Lerner

REFERENCES

1. D. E. Gray (ed.), *American Institute of Physics Handbook*, 3rd ed. (McGraw-Hill, New York, 1972), Sec. 5, p. 16.
2. H. G. Booker, *J. Inst. Elect. Eng.* **93** (Pt. IIA), 620 (1946).
3. J. F. Nye, *Physical Properties of Crystals* (Clarendon, Oxford, 1957), Secs. 4.3 and 4.4. For historical reasons, the negligible effect is called primary and the major effect secondary.
4. S. B. Lang, *Ferroelectrics* **11**, 519 (1976).
5. Y. V. Sinyavsky, N. D. Pashov, Y. M. Gorovoy, G. E. Lugansky, and L. Shebanov, *Ferroelectrics* **90**, 213 (1989).

REPORT DOCUMENTATION PAGE

Form Approved
OMB No. 0704-0188

Public reporting burden for this collection of information is estimated to average 1 hour per response, including the time for reviewing instructions, searching existing data sources, gathering and maintaining the data needed, and completing and reviewing the collection of information. Send comments regarding this burden estimate or any other aspect of this collection of information, including suggestions for reducing this burden, to Washington Headquarters Services, Directorate for Information Operations and Reports, 1215 Jefferson Davis Highway, Suite 1204, Arlington, VA 22202-4302, and to the Office of Management and Budget, Paperwork Reduction Project (0704-0188), Washington, DC 20503.

1. AGENCY USE ONLY (Leave blank)		2. REPORT DATE 15 May 1991		3. REPORT TYPE AND DATES COVERED Quarterly Technical Report, 1 February - 30 April 1991	
4. TITLE AND SUBTITLE Solid State Research				5. FUNDING NUMBERS C — F19628-90-C-0002 PE — 63250F PR — 221	
6. AUTHOR(S) Alan L. McWhorter					
7. PERFORMING ORGANIZATION NAME(S) AND ADDRESS(ES) Lincoln Laboratory, MIT P.O. Box 73 Lexington, MA 02173-9108				8. PERFORMING ORGANIZATION REPORT NUMBER 1991:2	
9. SPONSORING/MONITORING AGENCY NAME(S) AND ADDRESS(ES) Air Force Systems Command, USAF Andrews AFB Washington, DC 20334-5000				10. SPONSORING/MONITORING AGENCY REPORT NUMBER ESD-TR-91-106	
11. SUPPLEMENTARY NOTES None					
12a. DISTRIBUTION/AVAILABILITY STATEMENT Approved for public release; distribution is unlimited.				12b. DISTRIBUTION CODE	
13. ABSTRACT (Maximum 200 words) <p>This report covers in detail the research work of the Solid State Division at Lincoln Laboratory for the period 1 February through 30 April 1991. The topics covered are Electrooptical Devices, Quantum Electronics, Materials Research, Submicrometer Technology, High Speed Electronics, Microelectronics, and Analog Device Technology. Funding is provided primarily by the Air Force, with additional support provided by the Army, DARPA, Navy, SDIO, NASA, and DOE.</p>					
14. SUBJECT TERMS electrooptical devices high-speed electronics optical modulators charge-coupled devices quantum electronics microelectronics ultraviolet lithography epitaxial layers materials research analog device technology proton bombardment electrocaloric refrigeration submicrometer technology lasers vacuum microelectronics coplanar transmission lines				15. NUMBER OF PAGES 92	
				16. PRICE CODE	
17. SECURITY CLASSIFICATION OF REPORT Unclassified	18. SECURITY CLASSIFICATION OF THIS PAGE Unclassified	19. SECURITY CLASSIFICATION OF ABSTRACT SAR	20. LIMITATION OF ABSTRACT		